Rare earth doped optical fibers and amplifiers for space applications

Ayoub Ladaci

N° d'ordre NNT : **2017LYSES027**

PhD thesis
University of Lyon (France)
In co-tutelle with
Politecnico di Bari (Italy)

Doctoral School N° 488

Doctoral School Specialty: **Optic, Photonic and Microwaves**

Public Defense on 19/09/2017, by :
Ayoub LADACI

Rare Earth Doped Optical Fibers and Amplifiers for Space Applications

jury composed by:

Rissons Angélique,	Professor/ ISAE-SUPAERO	Rapporteur
Jurdyc Anne-Marie,	Professor/Institut Lumière Matière	Présidente
Prudenzano, Francesco,	Professor/Politecnico di Bari	Examiner
Mélin Gilles,	PhD/ iXBlue	Examiner
Boutillier Mathieu,	PhD/CNES	Examiner
Boukenter Aziz,	Professor /University of Lyon	These supervisor
Mescia Luciano,	Professor /University of Lyon	These supervisor
Ouerdane Youcef,	Professor /University of Lyon	These co-supervisor
Girard Sylvain,	Professor /University of Lyon	Invited

Table des matières

INTRODUCTION

This PhD thesis work has been accomplished in co-tutelle between the University of Saint-Etienne in France and Politecnico di Bari in Italy and in the framework of a collaboration with iXBlue Photonics funding the CIFRE research grant. Furthermore, the work was done in close collaboration with other research labs, particularly the French Space Agency CNES and the CEA DAM DIF. Its main objectives are to advance the state-of-the-art regarding the development of Rare-Earth Doped Fiber Amplifiers (REDFA) tolerant to the space harsh environment by improving our understanding of the basic mechanisms causing a degradation of these amplifier performances when exposed to various types of irradiation.

In Chapter I of this manuscript, the context and state-of-the-art of the research topic of the PhD thesis are briefly described. REDFAs and lasers sources (REDFSs) are widely used in several on-Earth applications such as telecommunications. In addition to intrinsic advantages offered by the optical fibers such as their small-sizes, light weight, immunity to electromagnetic interferences…, the REDFA renders possible the direct amplification of signals in the 1550 nm Telecom window with high output powers, quite low noises figures, no dispersion and low power consumption. All these advantages made this mature technology very interesting for space applications such as inter-satellite and satellite-ground free space telecommunication systems or as super luminescent sources integrated in the satellite navigation systems. However, the conventional EDFAs and EDFS suffer from a high sensitivity to radiations. Indeed when they are exposed to radiations, a strong decrease of their performances is observed that limits their integration in space. It was demonstrated that the Rare Earth (RE) doped optical fiber (REDFs) is the most sensitive component of those systems. In Chapter II are detailed the basic mechanisms and physical mechanisms related to the amplification phenomenon in such RE-doped glasses, mandatory to understand the physics of radiation effects on REDFA. As an example, REDFs are often co-doped in their cores with Al and/or P to prevent the RE ions clustering that degrades the amplification. However, those interesting co-dopants also enhance the glass radiation sensitivity leading to higher radiation induced attenuation levels and explaining the bad response of REDFs compared to Telecom-grade passive fibers. To enhance the REDFs radiation tolerance many studies were carried out and several solutions were proposed such as the hydrogen loading, the Cerium co-doping or alternative manufacturing processes. All these techniques, some of them provided by the consortium involved in this PhD thesis, provide good

solutions that made possible the manufacturing of radiation hardened REDFs allowing their integration in actual space missions, those solutions are classified as a *hardening by component strategy*. However, due to the fast increase of the space research programs, more challenging space missions are aimed with higher radiations doses which require more efficient radiation hardened REDF based devices. To this aim, an optimization of the REDFA at the system level using a coupled Simulation/Experiment is proposed in this thesis, to add the opportunity to use *hardening by system* strategy to the usual approaches. To achieve that, we update a state-of -the-art REDFAs simulation code, described in Chapter III, to consider not only its optical performances but also their evolutions due to radiation constraints during the space mission lifetime. The developed simulation tools required a limited number of experimental data as input parameters such as the radiation-induced losses. These data were obtained using several techniques such as setups to monitor these excess losses and other spectroscopic techniques that are all described in the Chapter IV and used to characterize the REDFs used to build the amplifier. After building the simulation tools, a validation phase was conducted through a comparison between REDFA simulation with experimental results acquired on the same various REDFA architectures before and after exposure to X-rays. This comparison, presented in Chapter V, validates the modeling tools reliability and accuracy and allows to exploit the validated code to optimize the REDFA architecture to mitigate the radiation effects.

Finally, the feasibility to incorporate several add-ons to these simulation tools has been evaluated through the coupled simulation and experiment approach. The obtained preliminary results are given in Chapter VI. In details, the photobleaching effects on the Erbium-DFA have been characterized and their impact on the REDFA performance evaluated through simulation. The metastable energy levels lifetime evolution as a function of the equivalent dose for various radiation types (X-rays, γ-rays, protons and electrons) has been experimentally investigated. At the simulation levels; new phenomena such as the thermal effects and WDM (Wave Division Multiplexing) configurations have been implemented in the code and are presented.

Chapter I.
Context, State-of-the-Art and Objectives

I.1 INTRODUCTION

Since their apparition in 1985 [1], the technology of Rare Earth Doped Fiber Amplifiers (REDFAs) has been widely used for data amplification in telecommunications systems. This class of optical amplifiers exploits the spectroscopic properties of Rare Earth (RE) ions such as Erbium or Ytterbium and sometimes combination of several of them. Doping the fiber core with these ions allows an enormous increase of the distance for data transmission [2]. Nowadays, the REDFAs are broadly used for their effective and reliable characteristics such as high gain, polarization independent gain, high saturation output power, low noise figure, and low insertion loss [3-6].

All those characteristics made this technology as the one of the REDFS (Rare-Earth Doped Fiber Sources) very interesting for space applications too. In particular, these devices can serve as active components of inter-satellite/satellite-ground telecommunication systems and are part of fiber optic gyroscopes devices. In this chapter, we describe the context of the PhD work described in this manuscript. This chapter is concluded with the state-of-the-art regarding the vulnerability and radiation hardening studies of REDFAs for space.

I.2 APPLICATIONS OF REDFA IN SPACE ENVIRONMENT

Since the 90s the REDFAs and REDFSs were proposed for integration in space applications. In particular, those technologies can be selected to replace conventional crystal and semi-conductor amplifiers, enhancing the performances. Furthermore, they can be potentially used in a large set of other systems such as [7]:

- Telecom/Transponders
- Navigation systems
- Altimetry; for the spacecraft altitude measurement.

- Atmospheric Light Imaging, Detection, And Ranging (LIDAR or DIAL); that used a laser probe to study atmospheric properties. The LIDAR can be used for the detection of wind, CO2, water vapor, volcanic activities too.
- Bathymetry; underwater depth and ocean floors study
- Automated planetary rovers; and also high power sources for laser processing applications

iXBlue company, that founded this work, has a high interest concerning the first two applications (Navigation systems and telecommunications devices) that are described below in more details.

I.2.1 The spacecraft navigation system

One of the key applications for EDFs in space environment is as super-luminescence optical sources for inertial navigation devices. The system is based on a combination of Fiber Optic Gyroscopes (FOGs) and accelerometer measurements allowing to precisely determine the instantaneous position and trajectory of the spacecraft. The EDFS are generally selected thanks to their high power delivery which significantly improves the signal-to-noise ratio (SNR) [8].

The fiber optic gyroscope technology is based on the Sagnac effect (also called Sagnac interference). Two beams (generated by the same optical source) are injected into a fiber coil (of few km in length) in opposite directions. According to Sagnac effect, the beam traveling against the rotation direction will experience a slightly shorter path delay compared to the other beam. Using interferometry, the differential phase shift between the two waves can be measured and the information about the angular velocity deduced. A basic schematic setup of a FOG is represented in figure I. 1.

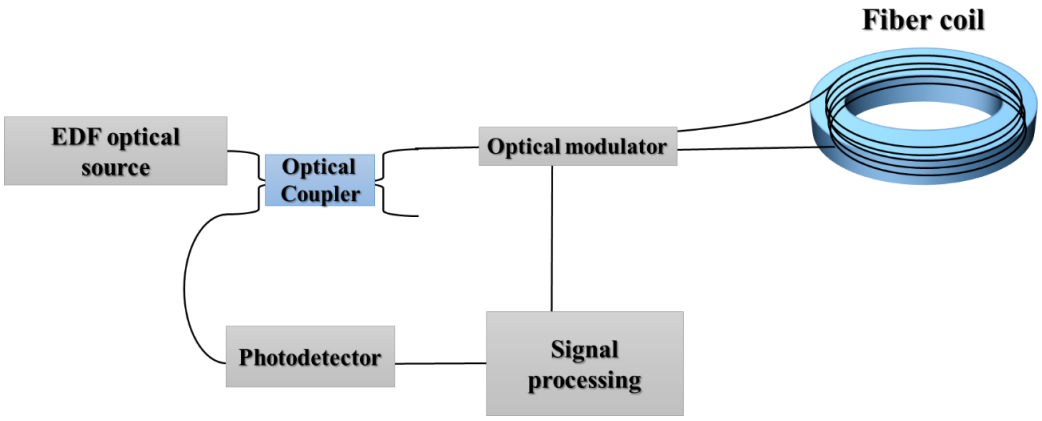

Figure I. 1. Basic schematic of an optical FOG

The FOG represents a breakthrough for space applications considering their performances, their high reliability (being a solid-state technology, no moving parts are needed) and a high versatility. Indeed, from a ground telecom mission to an earth observation mission, the design remains the same [9]. However, to qualify the FOG technology for a space mission, all the system component responses need to be investigated including the REDFS.

I.2.2 Inter-satellite and satellite-earth telecommunication systems

As a second space application, The EDFAs can be used as a signal amplifier in a wireless telecommunication system at both receiver and transmitter levels. The communication needs in earth (or planetary) observations are strongly increasing. In particular, the actual planets exploratory probes are equipped with several instrumentations inducing large data that need to be transmitted to the ground. Using optical communication systems, the data transfer speed reaches the 100s Gb/s instead of a few Gb/s. In addition, the FSO (Free Space Optical) telecommunication systems present several other advantages such as their simple deployment, low power consumption, electromagnetic interference immunity and high security.

I.3 RADIATION ENVIRONMENT

I.3.1 General aspects

The device response to radiation is not restricted only to the material composition itself but also depends on the radiation environment characteristics. In fact, the radiation environments are

generally characterized by their dose, dose rates and type of radiations. The knowledge of those characteristics is crucial for the conception of radiation hardened devices. The figure I. 2. represents several radiation environments of applicative and research interest as a function of their dose and dose rate ranges.

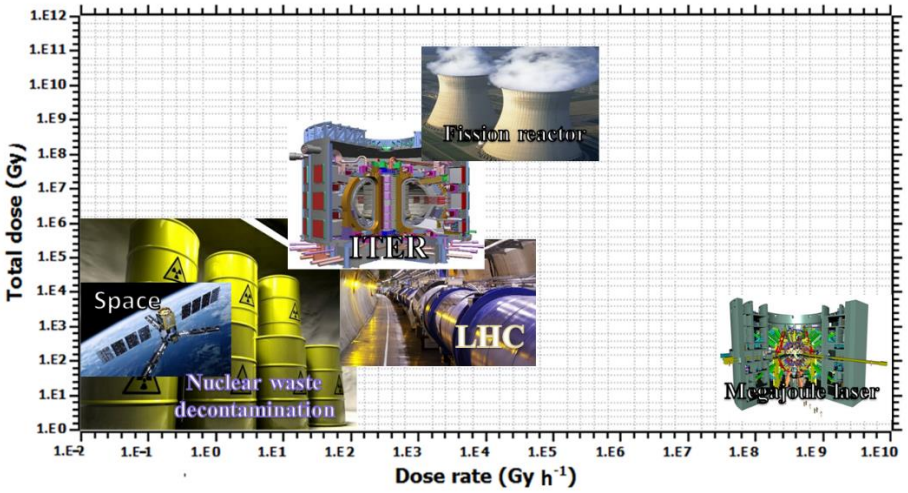

Figure I. 2. Several radiation environments characterized by their dose and dose rate ranges

The doses and dose rates depend on the aimed radiation environment and vary from Gy to TGy and from mGy/h to GGy/h, respectively. This wide range requires different optimizations and radiation hardening techniques for fibers and fiber-based systems.

Another characteristic of the radiation environment is the nature of radiations. In fact, depending on the radiation type, its effect on the device can strongly differ even for the same equivalent doses and doses rates [10]. Figure I. 3 represents the schematic synthesis of different phenomena that occur during the irradiation and the resulting cascade mechanisms leading to defect generation in silica-based materials [11].

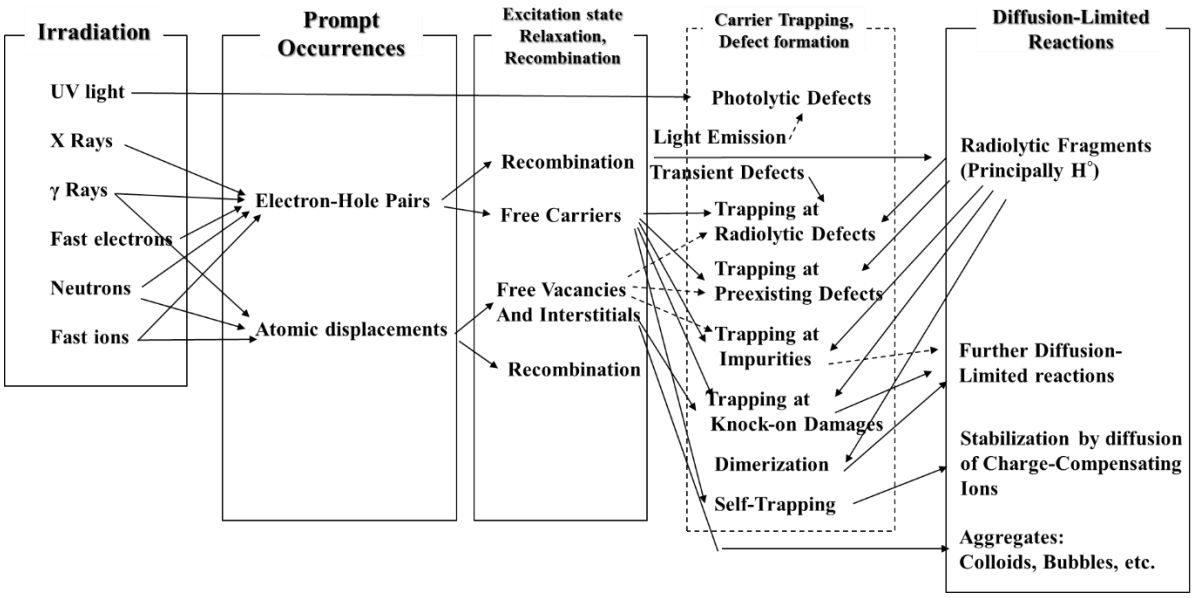

Figure I. 3. Radiation induced mechanisms occurring in the silica-based material during its exposure to the different radiation types (Modified from [11])

Two main mechanisms are activated depending on the irradiation nature and energy; the first is the atom displacements from their normal positions. Displaced atoms leave lattice vacancies and are incorporated into interstitial locations or cause interchange of dissimilar atoms in the lattice structure. This mechanism is also called the 'knock-on damage'. The second one is the ionization mechanism (radiolysis) that occurs when electrons are removed from atoms in the material inducing the formation of ion pairs in the path of the charged particles [12].

In this work, we focus on the vulnerability and hardening studies of REDFAs and REDFSs for space environment. This environment is characterized by low doses and doses rates, long mission duration (several years) and an associated harsh environment comprising several types of radiations.

I.3.2 Space environment

The natural space and atmospheric environments are characterized by strong thermal changes and the presence of different kinds of radiations. Its complexity renders the development of technological systems tolerant to these constraints very challenging. Indeed, those systems need to present the lowest degradation during the space mission without degradation of the performance requirements (high optical performances, low power consumption…). Figure I. 4. shows the

different constraints that a spacecraft undergoes during a mission and their influences on its different components materials.

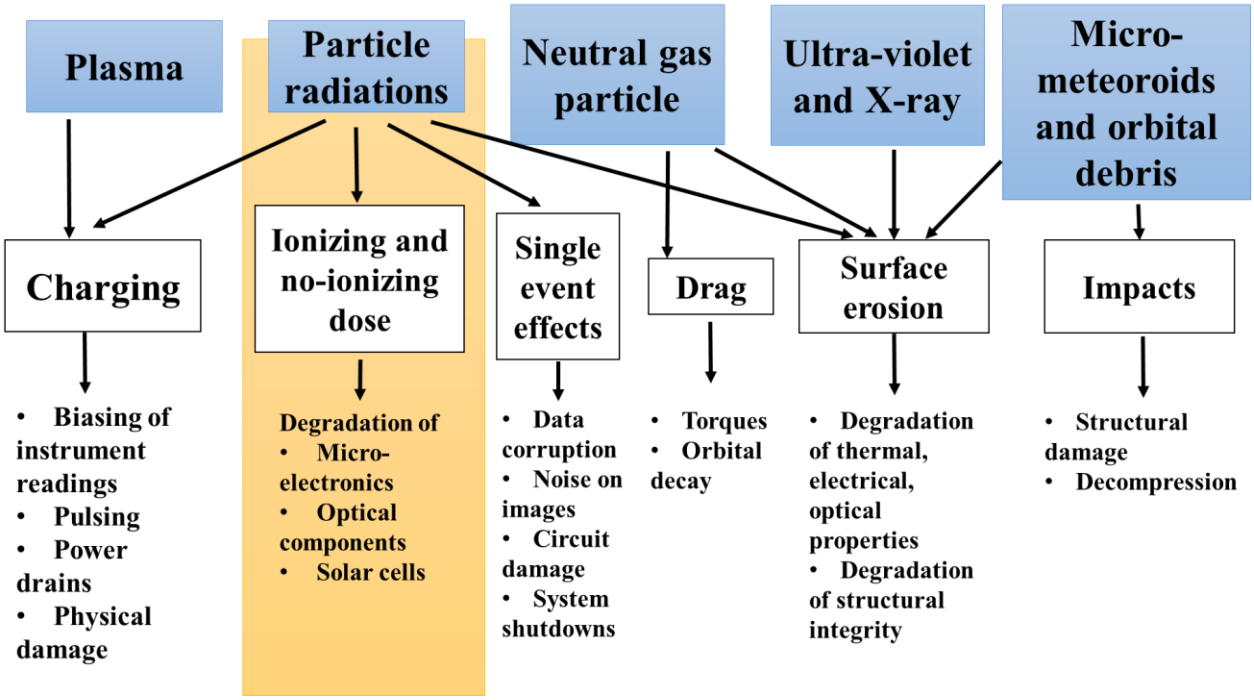

Figure I. 4. Types of constraints associated with space environment and their impact on spacecraft components [13, 14]

A critical step in the optimization of such systems is the knowledge of the expected space environment (doses, dose rates, radiation types), those parameters strongly depend on the orbit and mission profile of the spacecraft [15].

The space radiations can be classified as a function of their respective sources. The main ones are: solar particles (*energetic protons, alpha particles, heavy ions, and electrons*), trapped radiation in the 'Van Allen Belts' (*protons, electrons, and heavy ions*) and the cosmic rays (*energetic protons, electrons, alpha particles, and heavy ions*) [16]. Those particle energies are summarized in *Table I.1*.

Table 1. Maximum energy of particles in space

Particle Type	*Maximum energy*
Trapped Electrons	*Few MeV*
Solar Protons	*GeV*
Solar heavy Ions	*GeV*
Cosmic rays	*TeV*

I.3.2.A Solar particles

The sun chemical composition is mainly explained by Hydrogen and Helium at 98 %. The Sun radiation can be classified into 3 types: electromagnetic waves, solar wind and solar flares. Most of the electromagnetic radiations are non-ionizing and do not induce any radiation damages to the spacecraft devices but strongly affect the temperature constraint that in this turn can change the system radiation response. However, energetic photons as the UV light and X-rays induce defects on the material surface. In this case the exposed part of the space devices (as the solar cells) are the most vulnerable. The solar wind is a continuous steam of ions produced by the sun magnetic anomalies. The flux of those ions is typically ~ 10^9 particles cm^{-2} s^{-1} measured outside the earth's magnetosphere [17].

I.3.2.B. Trapped Particles

The Earth's trapped radiation belts were discovered by Van Allen in 1958. Outer space charged particles are trapped by the Earth's geomagnetic field, they helically move around the geomagnetic field lines in two motion trajectories between points near the north and the south poles; sliding motion along the magnetic field and bouncing motion along a line. In addition, a longitudinal drift around the earth of electrons and protons occurs (electrons to the East and protons to West), see Figure I. 5.

The South Atlantic anomaly is the region where the radiation belt reaches its lowest altitude. At low altitude the magnetic field intensity increases inducing an intense proton flux which strongly affects the low orbit space systems. The electrons of the Van Allen belts are also divided in two regions as represented in Figure I. 5.

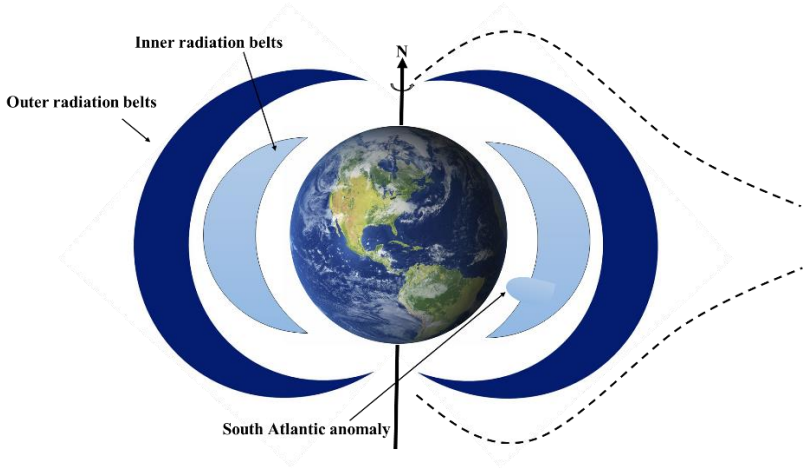

Figure I. 5. Trapped radiation belts around the Earth illustration (modified from [9])

I.3.2.C. Galactic Cosmic Rays

The GCR (Galactic cosmic rays) are particles mostly generated outside of our solar system. A high amount of those particles are generally protons (~ 85 %), the rest being alpha particles (14 %) and less than 1 % of gamma rays and electrons. The GCR can easily penetrate the spacecraft with their high energy. Additionally, their interaction with the atmosphere can generate other radiations of lower energy including X-rays, protons, muons, alpha particles, pions, electrons, and neutrons [10], this is called 'air shower secondary radiation' and is illustrated in Figure I. 6.

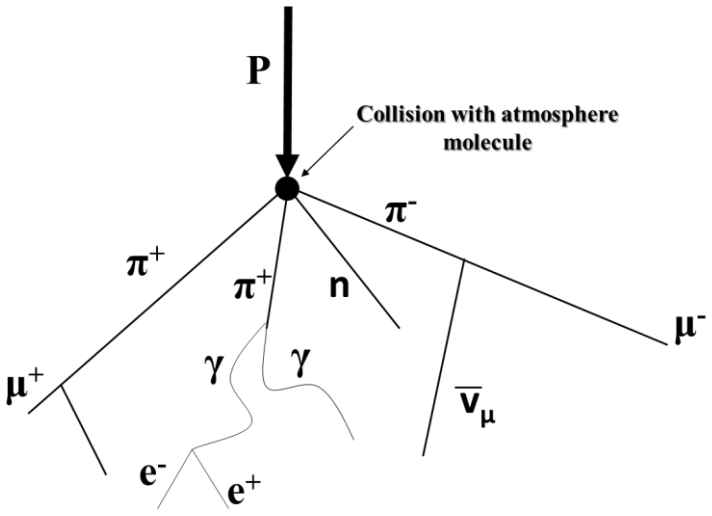

Figure I. 6. Air shower secondary radiation generated by a proton collision with the atmosphere (modified from [18])

It is important to notice that shielding against the GCR is very difficult due to their high energy making them a serious problem for the spacecraft engineers.

I.4. REDFAS ADVANTAGES FOR INTEGRATION IN SPACE

The very high cost of the satellite launching (~ 10^4 $/kg) renders the space needs for integrated devices very severe. In fact, to be qualified for space, a proposed device needs to succeed to pass several tests in conditions similar or more severe than the mission requirements (generally those conditions are chosen considering the worse expected cases during the mission) [19].
The REDFAs present a high interest for the space applications due to their performances compared to alternative technologies. In addition to the interesting optical fiber characteristics such as the electromagnetic immunity, high bandwidth, light weight,… REDFAs shows high performances as:

- High amplification: REDFA can induce amplification gains exceeding ~ 40 dB at 1550 nm.
- Wide bandwidth: The Erbium amplification spectrum is flat region over 40 nm (5000 GHz) allowing WDM (Wavelengths Division Multiplexing) multiplexed configurations.
- High input powers: can support high signal input power hundreds of mW in case of EYDFAs.
- Low noise figure: the induced noise of REDFAs is quite low compared to other technologies.
- Availability of high power pumping diodes at ~ 980 nm, already qualified for space applications with multimode output powers of about ~ 50 W.

I.5. REDFAs DRAWBACKS FOR INTEGRATION IN SPACE

The conventional REDFAs and lasers present some drawbacks, limiting their use in harsh environments. The most notable of them are their high temperature sensitivity and their radiation vulnerability. It was demonstrated that the active optical fiber was the most vulnerable component of these systems [20].

I.5.1. Radiation vulnerability

As described above, space is characterized by the presence of several types of radiations. As the active fiber is generally codoped with Aluminum and/or phosphorus to prevent RE ions quenching (more detail in *Section II.3.4*), these fibers present a high vulnerability to radiation compared to passive fibers doped with Fluorine or Germanium [21]. The fiber degradation affects the REDFA performances during the mission. In particular, the gain of the amplifier decreases and its noise figure increases, the amplitudes and kinetics of these changes being dependent of the selected fiber and amplifier architecture.

I.5.2. Temperature dependence

The temperature dependence of the REDFAs is a big issue in particular in the space environment, where high temperature gradients are observed between the day and night (depending on the sun exposure and distance). High temperature affects the amplifier gain by different mechanisms such as the temperature induced refractive index changes and evolution of the ions emission and absorption cross sections… (see VI. 5.). To limit this issue, the REDF based devices are usually thermally regulated to avoid these external temperature fluctuations and associated amplifier performances degradation [22].

I.6. RADIATION EFFECTS ON OPTICAL FIBERS

During the last decades, the optical fiber application field has exceeded the telecommunication market, and the strong research activities in OF based devices open new perspectives for their use in several domains for temperature and/or strain sensors (using Rayleigh, Brillouin, Raman, fiber Bragg grating [23]), or spectroscopy analysis, diagnostics, …. When fibers are integrated in radiation environment, the optical fiber transmission properties are affected. Main effect is the attenuation increasing with the accumulated dose.

I.6.1 RIA in passive optical fibers

When silica-based devices are used under irradiation, color centers are created due to the radiation-released electron and holes trapped on defects pre-existing in the amorphous silica glass based network before the irradiation or being created during the exposure. The created point defects, also called color centers, are responsible for an excess of optical losses that increases with the dose. Their optical properties (absorption, luminescence) and their generation rates depend on many parameters including the irradiation conditions, the fiber composition and its manufacturing process. [24]

Until now, a complete model allowing to predict the OFs degradation under irradiation is still missing. However, an empirical model allowing to estimate the fiber radiation induced attenuation (RIA) dependence to steady-state radiations dose was proposed in [25]. According to this work, the RIA growth dependence can be reproduced using a power law function (equation I.1).

$$A(D) = C_0.D^{\beta} \qquad \text{(I.1)}$$

Where $A(D)$ is the RIA, D is the total accumulated dose. β $(1 > \beta > 0)$ and C_0 are constants that depend on the fiber properties and the operation wavelength.

The process of defect creation in fibers is dominated by two competitive phenomena: the point defect generation mechanisms (their efficiencies depend on dose rate, dose, fiber composition…) and the point defect bleaching mechanisms through photobleaching or thermal bleaching (their efficiencies depend on the light power density, operation wavelengths, fiber composition…) [26].

Another important RIA feature concerns its dose rate dependence. Dose rate directly impacts the competition between the mechanisms of point defects creation and bleaching at a given dose. In other words, when the dose rates increase the defects have less time during the irradiation run to recover whereas at lower dose rate, the bleaching mechanisms will have a stronger influence.

The defects in the amorphous silica glass can be classified in two types as a function of their behaviors during and after the exposure at room temperature (RT): the RT stable defects or ‘permanent’ defects and the RT metastable defects or ‘transient’ defects that are partially bleached during the run and quickly recovered as soon as the irradiation stop. Due to these transient defects,

the RIA decrease as a function of the time after irradiation usually follows a stretched exponential function converging to a constant value (A_p) that represents the contribution of the permanent defect to the RIA (equation I. 2) [27].

$$A(t) = \underbrace{A_0 \exp\left[\left(\frac{-t}{\tau}\right)^{\alpha}\right]}_{A_T(t)} + A_P \qquad \text{(I. 2)}$$

Where A_0 is the contribution of transient defects to the RIA at the end of the irradiation, τ is the decay time and α $(1 > \alpha > 0)$ is the stretching coefficient.

I.6.2 Radiation effects on RE doped optical fibers

Previous studies demonstrate that REDFs are dramatically affected by radiations compared to other classes of optical fibers [21, 28]. In fact, this kind of fibers undergoes RIA of hundreds of dB/m after only a limited dose (below 100 krad, 1 kGy) [29]. This high radiation vulnerability is mostly explained by the composition of the fiber host matrix usually codoped with Aluminum and/or Phosphorus. In fact, it was reported in [30] that the RE ion (Er or Yb) concentration weakly impacts the fiber RIA response compared to the Al and P-related defects.

It is important to notice that the RIA generated in the RE optical fibers, considering the dose and dose rate ranges of space, has been shown as independent of the nature of particles (γ-rays, protons) meaning that similar color centers at the same concentrations seem generated by these particles [30]. In this PhD thesis work, these preliminary results made possible to compare the exposure effects of several types of irradiation by focusing on X-ray testings that can be performed at the LabHC.

The RIA kinetics appear to be more complex in the case of RE doped fibers compare to the pure-silica-based ones. In this case two different models (for different dose rates) are used to reproduce the RIA evolutions during irradiation.

In the case of low dose rate the RIA (A) kinetic in an Er doped fiber can be fitted using equation I. 3 that depends on the irradiation dose (D) and dose rate ($\dot{D}$).

$$A(D,\dot{D}) = C_0.\dot{D}^{\frac{1-\beta}{n}}.D^{\beta} \qquad \text{(I. 3)}$$

Where n is the kinetic order of the transient RIA recovery.

In the case of a high dose rate, the use of a saturating exponential (equation I. 4) has been shown as more efficient to reproduce the fiber response.

$$A(D) = \sum_i a_i \left[1 - \exp\left(\frac{-D}{\tau_i}\right)\right] \qquad \text{(I. 4)}$$

Where the contribution of each color center 'i' is defined through a term related to its absorption [31].

In space, the dose rates are quite low, then the first formula (equation I. 3) can be used to fit the RIA response of REDFs.

Depending on the incorporated dopants and associated defects, the radiation induced optical losses evolve after the exposure. In the presence of Phosphorus in the fiber core or cladding, the recovery processes are very limited at room temperature, as the P-related defects absorbing in this region (P1 defects) are stable after the irradiation for a long time [32]. This differs for the case of Al-codoping where the Al-related defects are known to be more sensitive to Photo/Thermal-bleachings. This explains that for EDFAs (generally Er^{3+} ions are embedded within an aluminosilicate matrix), the RIA kinetics during the irradiation are more sensitive to the signal and pump input powers whereas for Erbium\Ytterbium co-doped fibers (generally incorporated into a phosphosilicate glass), this is less the case even if higher pump power densities are usually involved.

I.7. RADIATION HARDENING STRATEGY FOR REDFAs

Since the first proposal to implement REDFAs in space environment, their response to radiations was widely studied in the literature. As the active fiber was identified as the most sensitive part of the amplifier architecture, several studies were carried out in order to identify effective solutions

to mitigate the observed radiation effects. The most relevant of them are described in the next paragraph.

I.7.1. Hydrogen pre-loading of the REDFs

It is well known that hydrogen presence in silica glass can significantly improve its response to radiations [33]. In particular, the interstitial hydrogen loaded before the irradiation reduces the amount of precursor centers to be converted in optically-active radiation induced defects during the exposure. Furthermore, those radiation induced point defects can also be passivated by hydrogen. Namely, hydrogen converts the radiation induced defects into hydrogen-related defects associated with absorption bands ranging outside the usual application spectral domains [34].

The same behavior was observed in phosphosilicate or aluminosilicate doped fibers. In particular, the hydrogen loading directly impacts these fiber RIA radiation responses. In [35], a comparison between the γ-ray responses of Erbium-Ytterbium doped fibers treated or not with hydrogen before exposure is discussed. The results demonstrate that the non-treated sample undergoes respectively, about 1.5 and 0.15 dB/m at 915 and 1550 nm wavelengths after a 90 krad dose, instead of less than 0.05 dB/m for both wavelengths in the pre-treated sample. The deuterium loading is efficient too as demonstrated in [36] where an EDF response to 30 krad of 63 MeV Proton irradiation was investigated, after the irradiation the D_2 loaded sample undergoes 5× less RIA than the non-loaded sample.

The H_2 or D_2 loading of REDF is an effective way to improve their response to radiation and then the one of the REDFAs. However, it is difficult to ensure that the gas, very mobile at room temperature, will be maintained in the fiber core during the whole duration of the space mission (typically dozens of years). To overcome this issue, a solution [37] consists in adding a carbon layer around the fiber (thickness of hundreds of nm) to prevent the H_2 or D_2 outgasing in the temperature range of interest. In this way, the gas can be kept in fiber for years, however, that solution makes more difficult the fiber gas loading. The selected solution is then to perform a series of holes (of ~ 3 μm of diameter) along the fiber longitudinal axis. These holes have no impact on the fiber guiding properties but can be used to inject the gas from one of the fiber extremities. After loading, splicing hermetically closes the fiber. This fiber architecture is called HACC (Hole Assisted Carbon Coated) fiber and is now under qualification by the French Space Agency (CNES).

Such a solution is more difficult to implement on Yb or Er/Yb-doped optical fibers with double clad geometries. This is due to the second clad nature (generally acrylate or polyimide) which does not support the carbon coating deposition. In fact, in the high power YDFAs and EYDFAs, the multimode pump power is guided using the first pure silica and the second acrylate or polyimide cladding. In order to reach high numerical aperture (of about 0.65), a low refractive index material needs to be used in the fiber second clad manufacturing (typically n ~1.3), which cannot be achieved using the doped silica glass.

I.7.2. Cerium Co-doping

Ce incorporates in the silica network as either Ce^{+3} or Ce^{4+} species [38] and the ratio between the concentrations of these two typologies depend on the production processes: an oxygen rich atmosphere promotes the creation of Ce^{4+} whereas the Ce^{3+} concentration is larger in a deficient oxygen atmosphere [39].

Under irradiation the Ce^{3+} typology can be converted to $(Ce^{3+})^{+}$ species [39] with different optical properties compared to the Ce^{4+} ions, those differences being explained by the difference in the environment surrounding the two ions.

$$Ce^{3+} \rightarrow (Ce^{3+})^{+} + e^{-} \qquad (5)$$

During the exposure, the electrons released by ionization can interact with some of the generated point defects such as the Oxygen Hole Centers, allowing to passivate them.

It was reported in [35, 41] that the Cerium co-doping of the silica glasses significantly reduces the impact of several defects-related absorption bands, in particular in Al or P-codoped fibers. It was demonstrated in [41] that the Cerium presence in an Erbium doped P-doped fiber affects the P_1 defect creation and their associated IR absorption as well as the P=O bond rupture leading to POHC centers. Those two types of radiation induced defects are also linked through a conversion mechanism. The following scheme represents both mechanisms.

P=O radiolysis → POHC center (during the irradiation)

POHC center → P_1 center (during and after the irradiation)

Both mechanisms are affected by the presence of Cerium that allows to strongly reduce the amount of generated POHC and P_1 centers [42].

I.7.3. RE Nano-particle doping

Based on the fact that the RIA generated in REDFs is mostly due to the P and/or Al co-doping of the silica host matrix, several studies were carried out in order to propose alternative manufacturing techniques allowing to reach high RE concentrations avoiding quenching effects while keeping low the P or Al amounts. In [43] a fabrication process based on the RE nanoparticles doping procedure is described, the quenching in the fiber is reduced even for low aluminum concentrations allowing to design Er doped fibers more resistant to radiations with interesting optical properties. This study opens new perspectives for future RE doped pure silica core fibers.

I.8. STATE OF THE ART OF REDFAS HARDENING

I.8.1 EDFAs hardening

The actual radiation hardened EDFAs by these techniques have a good resistance to radiations pushing their integration in today space missions. It was reported in reference [36] that the HACC EDFs can undergo much lower degradation compared to other conventional and radiation tolerant fibers from earlier work reported in [44]. The performances of the various fibers are reported in Figure I.7 where NP-Si+ sample corresponds to the one developed by the Nano-particle DRAKA approach [43], AL-LB is a conventional EDF and RTAC is Radiation Tolerant Acrylate Coating Fiber (hole-free) from iXBlue.

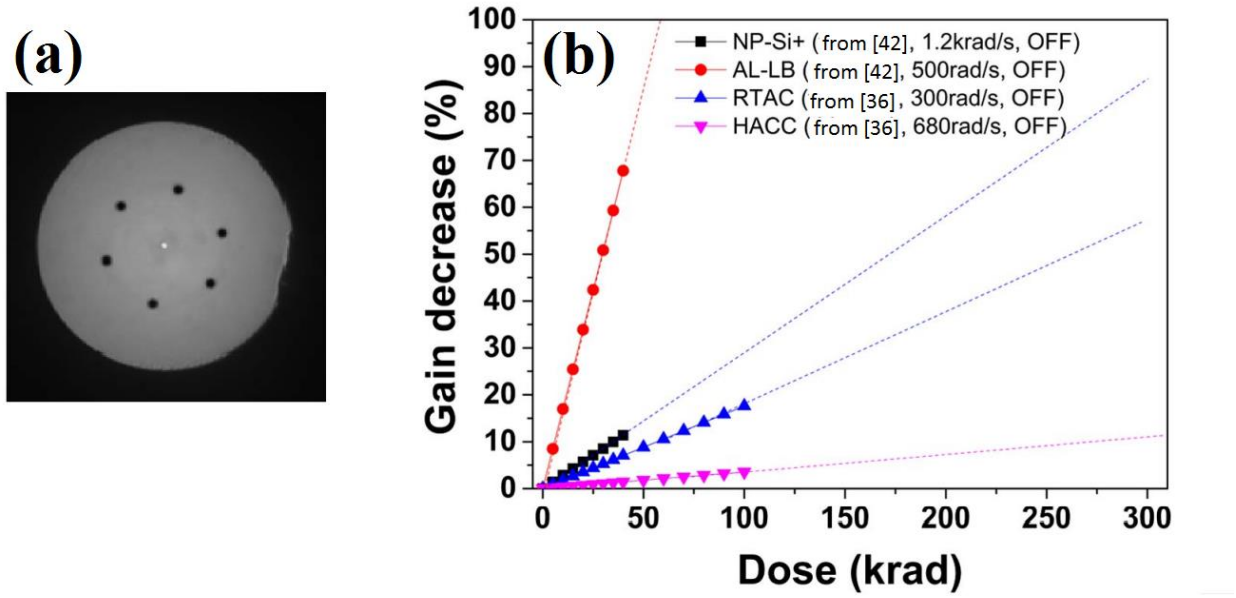

Figure I. 7. HACC optical fiber (a) its microscope image, (b) its gain decrease during the irradiation compared to other conventional and radiation hardened fibers from reference [36]

The HACC sample undergoes less than a 10 % gain degradation at the maximum irradiation doses (300 krad) instead of 60 and 70 % in the case of RTAC and NP-Si+, respectively. In these conditions, we can assume that the HACC based EDFAs can be used for space applications with good performances during the whole mission lifetime.

I.8.2 EYDFAs hardening

In some application, higher output powers are required (such as for satellite-ground telecommunication systems). In this case EYDFAs are used instead of the EDFAs. Several solutions for the manufacturing of radiation hardened EYDFAs are proposed such as the hydrogen loading or/and the Cerium co-doping. The good radiation responses of those systems are demonstrated in [35] by comparison with reference amplifier responses. Figure I.8 represents the degradation level of these different amplifiers using different classes of active fiber. All the systems are tested under the same conditions.

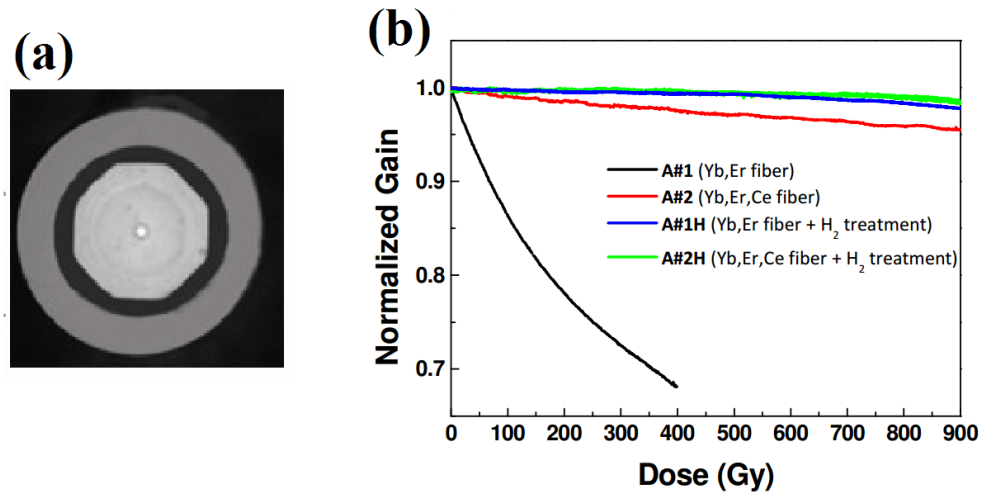

Figure I. 8. (a) DC EYDF microscope image, (b) the normalized gain decrease during the irradiation for different fiber compositions from [34]

The Ce doped/hydrogenated sample exhibits the best performances during the irradiation with a slight improvement compared to the sample that was only hydrogen pre-treated. In the other hand, the Cerium-doped sample also shows a good resistance during the exposure compared to the conventional amplifier (A#1). However, as explained in *section I.7.A.*, as the hydrogen cannot be kept easily into the EYDF, we assume that today the Cerium doped sample (A#2) remains the reference one that should be considered for space missions.

I.9. OBJECTIVES OF THIS PHD WORK

Today, the vulnerability studies of REDFAs are mainly conducted through an experimental approach based on accelerated tests at Earth irradiation facilities. During these tests; the samples undergo a dose corresponding to dozens of years of exposure in space in a few hours or days. As a consequence, the dose rates of the tests are about 10^4 higher than the ones characterizing the natural space environment. The dose rate influence on the REDFAs remains a key issue as several studies demonstrate a direct relation between the RIA, the dose rate, and the operating conditions [44, 45] (see section VI.2). In other words, using this approach we usually overestimate the REDFA degradation in terms of gain during the mission. However, those studies can permit to build a model that can be used to improve the prediction of the amplifier degradation during the space mission as well as the potential efficiencies of various radiation hardening techniques.

In addition, the hardening techniques described in this chapter are mainly based on a Hardening-By-Component (HBC) approach, exploiting alternative fiber compositions and manufacturing processes to improve the tolerance of REDFAs. In this work, we investigate the potential of coupling these HBC approaches to an additional Hardening-By-Design (HBD) procedure. In fact, different REDFA parameters such as pumping configurations, fiber lengths, signal and pump wavelengths, input signal power, … can also affect the amplifier response to radiation and their optimization is based on ground performances, not space ones. As a consequence, it is possible to imagine to design a REDFA with limited gain degradation during the mission thanks to a design especially conceived to reduce the radiation effects. To achieve this, several challenges have to be overcomed. If successful, the validated simulation tools coupled with a limited number of experimental data can be exploited to conceive radiation hardened (by HBC and HBD) REDFAs.

This PhD thesis work can be divided in the following main steps:

- The acquisition of a REDFAs simulation code and its adaptation to our samples and applications. This was not existing in the laboratory even if such codes are state-of-the-art for telecommunication applications.
- The validation of this code for the not-irradiated REDFAs manufactured during this work and a fine study of the influence of the different spectroscopic parameters on the simulation accuracy.
- The validation of the code developed during this PhD thesis for the radiation effects module through a comparison with experimental data in different irradiations conditions. In particular, one open question regards the possible impact of other radiation effects (changes in ion spectroscopic properties,…) than the RIA.
- The code accuracy improvements by considering different phenomena such as the photobleaching effect on RIA with respect to the profile of use of the REDFA and the thermal effects on the EYDFA radiation response. In addition, the implementation of complementary modules allowing the WDM simulations is targeted to ensure the versatility of our codes for the needs of future missions.
- Finally, exploitation of our coupled Simulation/Experiment approach to optimize amplifier REDFA performances during the irradiation and to mitigate the radiation effects over the whole space mission duration.

In this chapter, we present the context, the state-of-the-art and the objectives of this PhD thesis work devoted on the radiation hardening of fiber-based optical amplifiers (REDFAs) for space applications.
In *sections I.2-I.5* we introduce the space environment and its challenging constraints, the possible applications for REDFAs in space detailing the advantages and drawbacks of this technology for today's and future space missions. In *section I.6,* we briefly describe how radiations affect optical fibers in general and REDFs more particularly. Thereafter, the different radiation hardening techniques and the state-of-the-art regarding these hardening solutions are explained in *sections I.7* and *I.8.* Finally, the objectives of this PhD thesis work are given in *section I.9*

EN

Dans ce chapitre, le contexte, l'état-de-l'art et les objectifs de ce travail de doctorat sur l'amélioration de la tenue aux contraintes de l'environnement spatial des amplificateurs optiques (REDFAs) sont introduits. Dans les *sections I.2-I.5* cet environnement et ses contraintes sont présentés ainsi que les applications possibles des REDFAs dans l'espace, en détaillant les avantages et inconvénients de cette technologie pour les missions spatiales actuelles et futures. Dans la *section I.6,* les effets des radiations sur les fibres optiques en général et sur les fibres dopées aux terres rares plus particulièrement sont brièvement décrits. Par la suite, les différentes techniques de durcissement aux radiations des REDFs et REDFA sont présentées ainsi que leur état de l'art dans les *sections I.7* et *I.8.* Finalement, les objectifs de ce travail de thèse sont listés dans la *section I.9.*

FR

In questo capitolo sono introdotti il contesto, lo stato dell'arte e gli obiettivi di questa tesi di dottorato, dedicata al miglioramento della resistenza alle radiazioni degli amplificatori ottici a fibre (REDFA) per le applicazioni spaziali. Nelle sezioni I.2-I.5 questo ambiente radiativo e i suoi vincoli sono presentati, insieme alle possibili applicazioni degli REDFA nello spazio, dettagliando i vantaggi e le limitazioni di questa tecnologia per le missioni spaziali di oggi e future. Nella sezione I.6, gli effetti delle radiazioni sulle fibre ottiche in generale e in particolare sulle fibre dopate alle terre rare sono bevemente descritti. Successivamente, le diverse tecniche per migliorare la resistenza alle radiazioni dei REDF (t as pas defini le REDF) e REDFA e il loro stato dell'arte sono riportati nelle sezioni I.7 e I.8. Infine, gli obiettivi di questa tesi di dottorato sono riportati nella sezione I.9.

IT

Chapter II
Rare-Earth Doped Fiber Amplifiers: basic mechanisms and architectures

II.1 INTRODUCTION

In order to build a Multiphysics/Multiscale model for the simulation of REDFA performances, a good understanding of the physical aspects related to the spectroscopy of the Rare Earth ions and the light amplification process is needed. In this chapter we introduce those general aspects for ions focusing our attention on Erbium and Ytterbium ones. The main ions properties are described as well as the ion-ion interactions and the influence of the host matrix. Indeed, the RE ions spectroscopic parameters are sensitive to their surrounding electrical field, and noticeably vary depending on their host matrix. In the framework of this manuscript, we introduce the pure and doped amorphous silica (a-SiO_2) glass networks and their influence on the RE ions properties.
In the last part of this chapter, the major parameters defining a REDFA performances are introduced, focusing on its amplification gain and its noise figure. Those parameters are the most crucial ones to characterize the REDFA performances before, during and after irradiation.

II.2 OPTICAL PROPERTIES AND SPECTROSCOPY OF IONS

II.2.1 Electron-phonon coupling in solids

The nature of the optical transitions in laser-active ions embedded in bulk materials can be explained by the Franck-Condon principle. According to this principle, the photon absorption is an instantaneous process. The nuclei are extremely heavy compared to the electrons, then, the electronic transition occurs in a short time scale with respect to the nuclear motion time. As a consequence, the transition probability is calculated for a fixed nuclear position. During the photon absorption the electrons can move whereas the nuclei have no time to readjust themselves during the process. In fact, this readjustment occurs after the photon absorption and results in vibrations. This occurrence can be illustrated by the potential energy diagram [46].

Figure II.1 represents the expanded Franck-Condon energy-level diagram modified from [47].

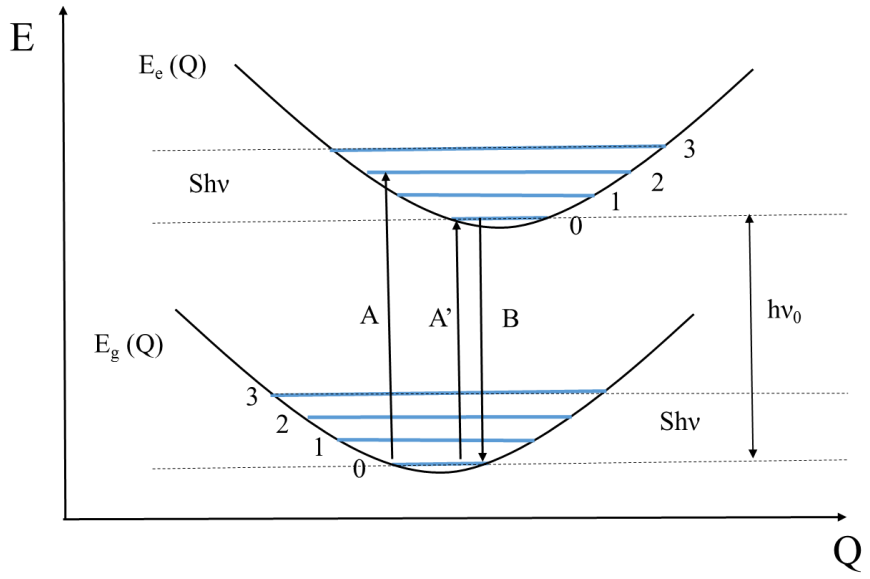

Figure II.1. Franck-Condon diagram of the ground and excited states of an optically-active center in solids modified from [2].

$E_e(Q)$ and $E_g(Q)$ are respectively the excited and ground state energies, (S) is the dimensionless Huang-Rhys factor (a well-defined function of the equilibrium position offset) and $h\nu$ is the effective phonon energy of the host material [48]. The vertical and horizontal axes represent the energy and the nuclear coordinates, respectively. (A) represents the absorption of a photon, (B) denotes the emission transition and (Q) is the distance between the nuclei (configurational coordinate).

The two potential curves represent the potential energies for the ground and excited states of the optically-active center as a function of the configurational coordinate. The excitation is represented by a vertical arrow which crosses the upper curve (notated as A in Figure II.1). The absorption of the photon puts the optically-active center in a non-equilibrium state. Consequently, this center relaxes into the lower vibrational states with phonons creation which are characteristic of the lattice vibration modes. As a particular case (represented by A' in Figure II.1), the process can result from transitions between the lowest vibrational states of the ground and the excited states (from the 0 of E_g to the 0 of E_e), in this case the absorption and emission lines are called Zero Phonon Lines (ZPLs). The time scale of relaxation ranges usually from sub-nanoseconds to milliseconds. The vibrational energy in the optically-active center is lost through phonons inducing heating of the host matrix. Thereafter, the center relaxes further through the electron transition from the excited

state to the ground state. The absorption and emission phenomena can be affected by two different energy conversions due to the interaction with the network phonons. The first creates a Stokes shift. In this case, the photon luminescence energy is lower than the excitation one, it is also called 'red shift'. On the other hand, an Anti-Stokes shift can be created which is also called 'blue shift'.

II.2.2 Spontaneous and stimulated emissions

In order to describe the spontaneous emission of an optically-active center, we can consider a simple atomic structure with two energy levels labelled as "1" and "2" associated with energies: E_1 and E_2, respectively. We assume that E_1 energy level is lower than E_2, and that E_1 corresponds to the ground state. If the considered atom energy is in the level 2, it will tend to decay to a lower level (level 1 in our case) and an energy equal to the difference between to the two involved levels $(E_2 - E_1)$ will be released by the system. If this energy is delivered in the form of an electromagnetic wave, this phenomenon is called 'the spontaneous emission' (Figure II.2.a). The emitted photon has an energy equal to $h\nu = E_2 - E_1$ where h is the Planck's constant and ν is the wave frequency. There is also the case where the decay happens without a radiative emission and the energy is then delivered in another form such as an energy transfer to the host matrix or to another atom.

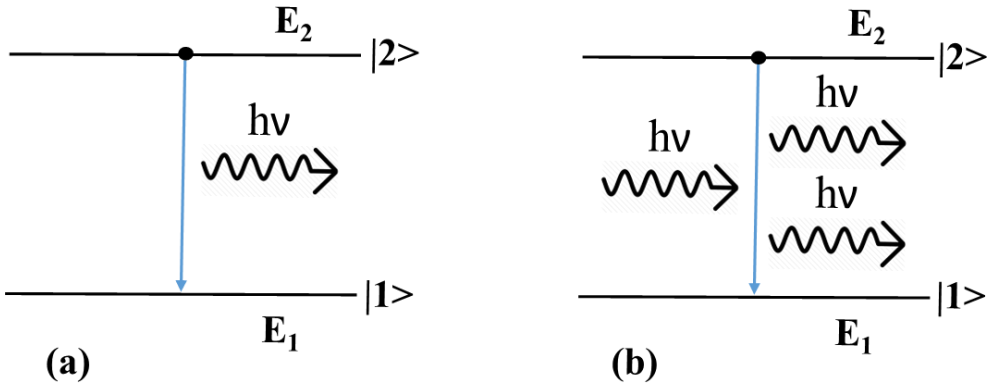

Figure II.2. Illustration of emission process in a simple 2 levels system
(a) Spontaneous Emission, (b) Stimulated Emission

In the case where a photon of an energy equal to $h\nu$ is incident on an atom which is already in its excited state (level 2), and since this photon energy is equal to the difference between the two energy levels, it has a finite probability to force the atom to relax through the emission of an electromagnetic radiation identical to the incident photon, duplicating it (Figure II.2.b). This process is called the stimulated emission [49].

In the case of the spontaneous emission, the phase and emission direction of the emitted electromagnetic radiation differ from one atom to another. In the stimulated emission case, since the process is forced by an incident photon, the electromagnetic radiations are emitted in the same direction and with a phase similar than the one of the incident photon.

II.2.3 The A and B Einstein Coefficients

Earlier in the 1900, Einstein assumes in his analysis of the radiation - matter interactions that the probability of a transition induced by an electromagnetic field is proportional to the energy density of the radiation field at the transition frequency. By following Einstein analysis, we can calculate the transition probability from the atomic energy level 1 to the excited level 2 using the Equation II.1.

$$W_{12} = B_{12}\, u(w) \qquad \text{(II.1)}$$

Where B_{12} is the Einstein coefficient for the transition from $|1\rangle \rightarrow |2\rangle$ and $u(w)$ is the radiation field energy density. In the same way we can calculate the stimulated emission transition (W_{21}) using B_{21} and Equation II.1.

If we labeled the equilibrium populations as N_1 and N_2 for the energy levels 1 and 2, respectively, we can write the ratio $\frac{N_1}{N_2}$ as a function of the degeneracy factors (statistical weights) of the levels 1 and 2 labeled g_1 and g_2, respectively (Equation II.2).

$$\frac{N_1}{N_2} = \frac{g_1}{g_2} exp\left(\frac{E_2 - E_1}{kT}\right) \qquad (II.2)$$

Where k is the Boltzmann coefficient and T is the absolute temperature [50].

In general, the equilibrium population in the excited state is lower than the one in the ground state. Einstein proposes the spontaneous emission process in order to obtain the correct population ratios.

A_{21} is the Einstein coefficient for the spontaneous transition process $|2\rangle \rightarrow |1\rangle$, and the variation in the ground level population is then given by Equation II.3.

$$\frac{dN_1}{dt} = -N_1 B_{12}\, u(w) + N_2 B_{21}\, u(w) + N_2 A_{21} \qquad (II.3)$$

If the whole system is at a thermal equilibrium at a given temperature T, $\frac{dN_2}{dt} = -\frac{dN_1}{dt}$ and the energy density is given by the blackbody formula (Equation II.4).

$$u(w) = \frac{8\pi\nu^2}{c^3} \frac{h\nu}{e^{h\nu/kT} - 1} \qquad (II.4)$$

When the system is in the thermal equilibrium $\frac{dN_1}{dt} = 0$ and from equations (II.3) and (II.4) we then obtain equations (II.5) and (II.6).

$$A_{21} = \frac{8\pi h\nu^3}{c^3} B_{21} \qquad (II.5)$$

$$B_{12} = \frac{g_2}{g_1} B_{21} \qquad (II.6)$$

The Einstein B_{21} coefficient can be also expressed as a function of the oscillator strength (f) of the transition as defined in Equation II.7.

$$B_{21} = \frac{g_1}{g_2} \frac{e^2}{4m\varepsilon_0 h\nu} f \qquad (II.7)$$

Where ε_0 is the dielectric constant of the vacuum, m and e are the masse and charge of the electron, respectively [51]. For a given optically-active center, the oscillator strength f can be estimated using the Equation II.8.

$$f \sim \frac{1}{(h\nu)^2 \tau} \frac{m\nu^2 c^3}{2e^2} \qquad (II.8)$$

Where $(h\nu)$ represents the zero phonon line energy position and τ is the radiative decay time [52].

II.2.4 Homogeneous and Inhomogeneous broadenings

The spectral lines broadening type (homogeneous or inhomogeneous) is linked to the nature of the glass matrix in which optically-active centers are generated. For Rare Earth ions embedded into a glass matrix, two phenomena are mainly responsible for the broadening of their optical line transitions: the homogenous and the inhomogeneous broadenings. The transition line shape is homogenous when all the emitting centers are affected in the same way otherwise, the transition is inhomogeneous. At room temperature (~ 300 K), for Rare Earth ions the homogenous spectral line broadening smooths the overall line shape that can be resolved only at low temperatures: Stark levels become more evident at lower temperatures which help to determinate the characteristic profile of the line shape.

II.2.4.A Homogeneous line broadening

The corresponding spectral lines of a purely radiative decay has a quasi-Dirac's delta function shape (e.g. the radiative transition with ZPLs). A homogenous broadening process such as the interaction of the centers with lattice phonons shortcuts the excited state lifetime. This homogenous broadening optical transition leads to a Lorentzian shape (Figure II.3, Equation II.9).

$$G_L(\nu) = \frac{\frac{\Delta\nu_h}{2\pi}}{(\nu - \nu_0)^2 + \left(\frac{\Delta\nu_h}{2}\right)^2} \qquad (II.9)$$

Where ν_0 and $\Delta\nu_h$ are the optical transition central frequency and the spectral line FWHM (Full Width at Half Maximum), respectively.

II.2.4.B Inhomogeneous line broadening

The nature of the inhomogeneous broadening of the optically-active center line shape comes from a local site-to-site variation in the surrounding environments of these centers. The optical transition spectral properties are then affected by the surrounding field in the lattice environment.

The inhomogeneous broadening shape is explained by a superposition of individual spectral shifting transition lines generated by the various surrounding types of optically-active centers. The

overall shape of the inhomogeneous broadening is usually defined by a Gaussian function (Figure II.3, Equation II.10).

$$G_G(\nu) = \frac{1}{\Delta\nu_{h'}}\sqrt{\frac{4\ln 2}{\pi}}\left[-4ln2\left(\frac{(\nu - \nu_0)}{\Delta\nu_{h'}}\right)^2\right] \qquad (II.10)$$

Where $\Delta\nu_{h'}$ is the spectral line FWHM [49].

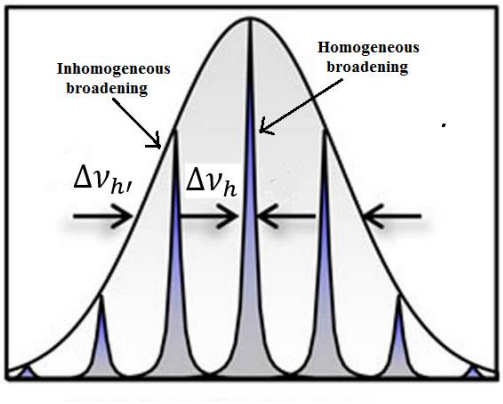

Figure II. 3: illustration of an Inhomogeneously broadened emission (Gaussian shape) and homogeneous emission lines (Lorentzian shape)

II.2.5 Energy level lifetime

The lifetime of an excited energy level is inversely proportional to its probability to relax (by transition to another energy level) per unit of time. The energy level total population decays as an exponential function depending on the time following the excitation event. When the relaxation is ensured by several de-excitation channels, the total probability is equal to the sum of the individual transitions probabilities. In general, the lifetimes of the Rare Earths ions in a glass matrix depend on two phenomena: the radiative and non-radiative transitions as described in equation II.11.

$$\frac{1}{\tau} = \frac{1}{\tau_R} + \frac{1}{\tau_{NR}} \qquad (II.11)$$

Where τ is the total lifetime of the energy level, τ_R and τ_{NR} are respectively, the radiative and non-radiative lifetimes.

The non-radiative lifetime strongly depends on the host matrix of the ions and of the nature of the coupling between the lattice vibrations and the energy levels of the excited ions. The relaxation process is ensured by the energy transfer from the excited state to the matrix phonons.

In the case of rare-earth ions, the non-radiative transition probability can be estimated by considering the level located directly below the excited one, and by measuring the energy difference between these two levels using as unit the highest phonon energy in the host matrix. The probability of the non-radiative transition will then be inversely proportional to the number of phonons needed to bridge the gap. This probability decreases as a function of the number of phonons required to relax the ion on the closer lower level following equation II.12 [53].

$$\left(\frac{1}{\tau_{NR}}\right)_{n,T} = \left(\frac{1}{\tau_{NR}}\right)_{n,0} \left[1 - exp\ \left(\frac{-h\nu}{KT}\right)\right]^{-n} \qquad (II.12)$$

Where $h\nu$ is the phonon energy, $n = \Delta E/h\nu_m$ is the number of phonons needed to bridge the gap ΔE between the two considered energy levels and $h\nu_m$ is the maximum phonon energy that can be coupled to the ions. $\left(\frac{1}{\tau_{NR}}\right)_{n,0}$ is the non-radiative transition rate at *T=0 K*.

II.2.6 Ion-ion interactions

For the previous discussed phenomena, the ions were supposed to be isolated from each other. In the case of a higher density of ions, the distance between the ions becomes very small and the ion-ion interactions increase. The ions can be close enough that a direct energy transfer from one ion to another occurs (spatial transfer). Such phenomena can strongly reduce the laser performances of highly-doped materials. However, in some cases the ion-ion interaction can enhance the amplification efficiency. This is the case for the Erbium-Ytterbium co-doped fiber amplifiers in which the pump energy is absorbed by Ytterbium ions that present the largest absorption cross section and then transferred this energy to the Erbium ion in charge of the amplification process [54].

The most important ion-ion energy transfer mechanisms in RE solid state lasers are illustrated in Figure II.4 (A-E). In these diagrams, S refers to the sensitizer ion that is the ion providing the

energy and A is the activator ion i-e. the one receiving this energy; this latter is also called the acceptor ion.

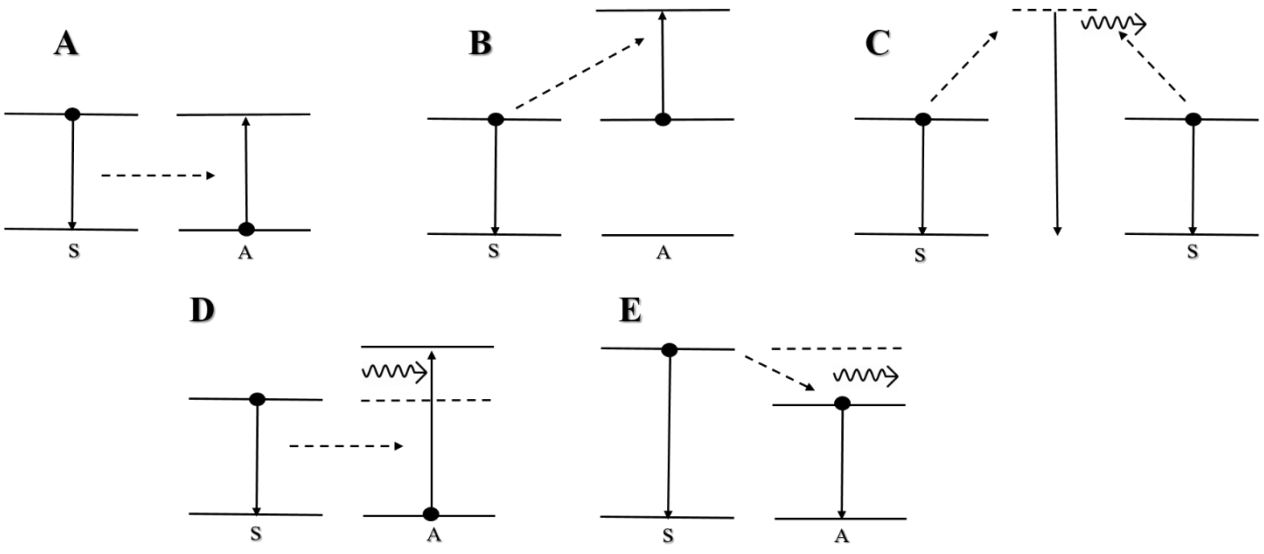

Figure II.4. Different ion-ion interactions in RE solid state lasers

A) Is the ***resonant energy transfer***, often observed when the excitation is not sufficient to excite all the ions of the system (low population inversion). The sensitizer ion which is in the excited state relaxes by giving its energy to another neighbor ion (the activator) in its ground state.

B) Is the ***stepwise up conversion mechanism***, it happens when the sensitizer gives its energy to an acceptor which is already in an excited state inducing its promotion to a higher energy level. This phenomenon induces energy losses at the excitation wavelengths due to an energy conversion to higher energy photons.

C) Is the ***cooperative emission***, that occurs when two excited ions (very close to each other) emit a photon at a higher energy. The emitted photon energy will be the sum of the two excitation energies (eg. the green emission observed in the Ytterbium-doped fiber lasers).

D, E) Are the ***cooperative energy transfer***s assisted either by the absorption (D) or the Emission (E) of phonons (E is the major cause of the energy transfer from Ytterbium to Erbium ions in a phosphosilicate glass).

II.2.7 Excited state absorption

When the upper state lifetime is longer enough (metastable state), their interaction with photons at the appropriate wavelength can promote excited state electrons to higher levels resonant with the incident photon energy. The ions excited at higher electronic levels may return to the metastable state by multi-phonon relaxation or radiative decay. In both cases the energy is lost through heating for the first case or by the emission of a photon at a different wavelength than the one of interest in the second case. Therefore, the reabsorption in the case of optical amplification can be a real problem, in particular for high power REDFA. Indeed, in this class of amplifier very high pump powers are injected in the very small volume of the fiber cross section inducing high energy density in the first portion of the active fiber, which strongly enhances this phenomenon and reduces the REDFA performances.

II.3 RARE EARTH ELEMENTS IN SILICA BASED HOST MATRIX

II.3.1 Rare earth elements

The REEs (Rare Earth Elements) includes the 15 lanthanide (Z= [57-71]) in the periodic table, in addition to Yttrium (Z=39). Their appellation comes from the fact that most of them were originally isolated as oxides from rare minerals earlier in the 19th century. Due to the similarities in their reactivity and their chemical properties, they were observed to be difficult to refine to pure metals. Otherwise, in the 20th century Sir William Crookes develops an effective separation processes [55]. *Table II.1* represents the lanthanide elements, their symbols, atomic numbers:

Table II.1. REEs, atomic numbers, and abundances [56, 57].

Element	Symbol	Atomic number	Element	Symbol	Atomic number
Scandium	Sc	21	Europium	Eu	63
Yttrium	Y	39	Terbium	Tb	65
Lanthanum	La	57	Dysprosium	Dy	66
Cerium	Ce	58	Holmium	Ho	67
Praseodymium	Pr	59	Erbium	Er	68
Neodymium	Nd	60	Thulium	Tm	69
Promethium	Pm	61	Ytterbium	Yb	70
Samarium	Sm	62	Lutetium	Lu	71
Gadolinium	Gd	64			

From the table we can observe that REEs are not so rare. As example the Cerium is present at a level of 64 ppm in the upper Earth's crust.

II.3.2 Atomic structures of the rare earths

The lanthanides character is given by the *4f* subshell electrons and the 17 RE metals possess an analogous electronic configuration. The electronic configuration of their neutral form is [Xe] $4f^N 6s^2$ (or [Xe] $4f^N 5d^1 6s^2$), where [Xe] is the Xenon complete configuration. N is the electron number in the *4f* subshell (going from 0 (La) to 14 (Lu)). Generally, the lanthanides exist in an ionic form with a 3+ valence. This ionization is achieved by the removal of two electrons from the *6s* subshell and of one electron from the $5f^N$. It can be done also by removing two electrons from the *6s* and the unique electron occupying the *5d* subshell. Some structural and electronic properties of REEs are reported in *Table II.2*.

Table II.2. Structural and electronic properties of REEs [58]

Element	Z/A	Electronic configuration	Radius /pm		Crystal structure
			Ionic	Metallic	
Sc	21/45	$(3d4s)^3$	78.5	164.1	*hcp*
Y	39/89	$(4d5s)^3$	88.0	180.1	*hcp*
La	57/139	$4f^0 (5d6s)^3$	106.1	187.9	*dhcp*
Ce	58/140	$4f^1 (5d6s)^3$	103.4	182.5	*fcc*
Pr	59/141	$4f^2 (5d6s)^3$	101.3	182.8	*dhcp*
Nd	60/144	$4f^3 (5d6s)^3$	99.5	182.1	*dhcp*
Pm	61/145	$4f^4 (5d6s)^3$	97.9	181.1	*dhcp*
Sm	62/150	$4f^5 (5d6s)^3$	96.4	180.4	*rhom*
Eu	63/152	$4f^6 (5d6s)^3$	95.0	204.2	*bcc*
Gd	64/157	$4f^7 (5d6s)^3$	93.8	180.1	*hcp*
Tb	65/159	$4f^8 (5d6s)^3$	92.3	178.3	*hcp*
Dy	66/163	$4f^9 (5d6s)^3$	80.8	177.4	*hcp*
Ho	67/165	$4f^{10} (5d6s)^3$	89.4	176.6	*hcp*
Er	68/167	$4f^{11} (5d6s)^3$	88.1	175.7	*hcp*
Tm	69/169	$4f^{12} (5d6s)^3$	86.9	174.6	*hcp*
Yb	70/173	$4f^{13} (5d6s)^3$	85.8	193.9	*fcc*
Lu	71/175	$4f^{14} (5d6s)^3$	84.8	173.5	*hcp*

hcc: Hexagonal Close Packed, *dhcp*: double hexagonal close packed, *fcc*: face centered cubic, *rhom*: rhombohedral, *bcc*: body centered cubic

II.3.3 Oxide Glasses

The oxide glasses as phosphate (P_2O_5) and silicate (SiO_2) systems get a high interest due to their wide range of uses in the photonics fields; particularly, in the manufacturing of fiber-based sensors, components and sources. The glass properties of these materials can be adjusted by doping them with impurities, called dopants. As an example the silica refractive-index can be increased by incorporation of Germanium, Phosphorus and Aluminum whereas adding Fluorine or Boron lowers it.

II.3.3.A Vitreous silica structure

Various structural models for vitreous amorphous silica (*a*-SiO_2) were developed even if none of them describes all its properties. Many experimental approaches were used as the X-ray and infrared spectroscopy, NMR (Nuclear Magnetic Resonance) to investigate this glass structure. Each of these techniques was used to investigate a specific physical characteristic of the optical material and none technique allows to obtain a global characterization of the whole *a*-SiO_2 system.

The morphological study of the amorphous materials is based on model structures. A model is applied for each physical propriety and the calculated results are compared with the experimental ones. The description of the glass networks has been greatly enhanced with the expansion of the modern computational devices. Many models already exist but none of them gives a complete definitive structure [59].

The two most used model structures in the case of the silica glass are based on:

- A network of randomly oriented crystallites
- A continuous random network of fully bonded molecules

II.3.3.B Doped silica glass

Silica is generally doped with other materials in order to meet the needs of modern optical systems. This leads to a high interest on the understanding of the structural environment of the sites occupied by the dopants and of their behaviors in a given glass matrix. In fact, the structure and optical properties of those glasses are strongly sensitive to the local environment surrounding the dopant elements.

As the dopants atoms offer novel properties to the material, the study of those atoms occupied sites is crucial. The ion available electronic states are mostly affected by the short-range order of the dopant sites. However, as the dopant concentration increases the influence of the dopant inclusion usually extends to larger ranges.

The modified random network model was suggested in [60] for the doped *a*-SiO_2 glass. In this model the glass structure consists of network formers of pure silica and modified atoms inter-network regions (Figure II.5). This model is based on EXAFS (Extended X-ray Absorption Fine

Structure) spectroscopy results which allow the extraction of short range structural information about a selected atom type into a given matrix.

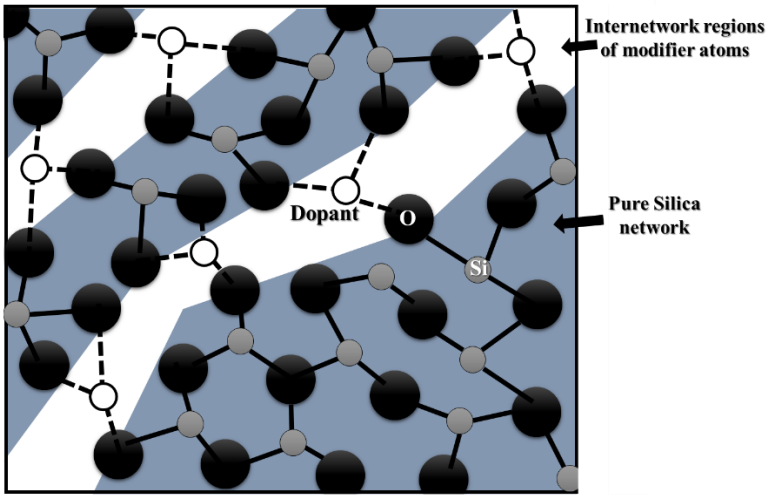

Figure II.5. Bi-Dimensional example of a modified Random Network, showing the covalently bonded network forming regions and the ionically bonded modifier atoms residing in percolation channels running through the network (modified from [60]).

The dopant atoms take positions in the glass network modifying their surrounding environments to satisfy the bonding requirements.

II.3.3.C Rare Earth doped glasses

Usually the RE ions are ionized to give di/trivalent ions (as the Er^{3+}, Yb^{3+}…). This ionization typically occurs by the loss of two $6s$ electrons and one of the $4f$ electrons (as described above). When RE ions are used as a glass dopant, a change of their energy diagram is induced and therefore of their optical properties. Two phenomena can be observed:

- The first one is due to Stark splitting, where the spectral substructure will become evident (the degeneracies in the energy level structure will be removed due to the inter-atomic electric field influence; crystal field).
- The second effect is the spectral broadening of the energy level. Its two main contributing factors are the phonons and the crystal field distribution. In the case of an amorphous host matrix the field is characterized by a non-uniform distribution and spatial variations occur all along the sample leading to an inhomogeneous broadening.

The RE doped glasses can be separated in two categories according to their properties and use. The optical properties of the first category are exploited in telecommunications and lasers whereas the second category is used for their interesting magnetic properties. For each of these categories a different host matrix is used, usually, silicate glass and semiconductor materials for optical applications and phosphate glass for the magnetic ones. In fact, the magnetic applications generally require higher RE dopant concentrations, which cannot be achieved without phase separation effects using the silicate glass.

Silicate glass is easy to produce using usual techniques such as the chemical vapor deposition generally devoted to the production of high quality optical glasses. It was demonstrated in [61] that the upper limit of RE dopant concentration in pure silica is about 1 wt.%. Beyond this value, clustering and phase separation phenomena occur between the RE dopants and the bulk silica network. However, if the silicate glass host matrix is co-doped with Aluminum or/and Phosphorus those effects can be reduced allowing to reach higher RE concentrations.

II.3.4 RE quenching issue in silicate glass

The choice of the RE dopant concentration to be used in the active devices conception is a critical issue that determinates the performances of the system. Among the most comment problems encountered in the manufacturing of REDFAs are the concentration quenching and phase separation effects. These effects are enhanced when the RE concentration increases in the silica. The concentration quenching decreases the amplifier efficiency, its negative impact increases with the ion concentration. In detail, the RE clustering significantly increases the ion-ion interactions and results in excitation losses via the cooperative emission. The quenching can be observed as a lifetime reduction of the RE excited state. In [62] an empirical formula allowing to express the measured lifetime τ as a function of the ions concentration ρ was proposed (Equation II.13).

$$\tau = \frac{\tau_0}{1+\left(\frac{\rho}{Q}\right)^p} \qquad \text{(II.13)}$$

Where τ_0 is the lifetime for very low ion concentrations, Q is the quenching concentration expressed in ions/m^3 and p is a constant depending on the involved energy level.

The silica-glass doping with Aluminum or/and Phosphorus increases the RE solubility and prevents the RE clusters formation. Aluminum ensures a complete cluster dissolution for RE concentration levels ranging from 10^{19} to 10^{20} cm^{-3} (about 0.1-1 wt.% for an Al/RE concentration ratio of about 10 or higher). This can be also achieved by the Phosphorus co-doping but at higher ratios (P/RE ratio of about 15) [62].

II.4 REDFAS MEASUREMENT AND CHARACTERIZATION

II.4.1 REDFAs operation principles

REDFA is used for the direct amplification of an optical signal without using an electro-optic conversion. The optical amplifiers can be classified as a function of the basic mechanism exploited to ensure the amplification: in semiconductor-based optical amplifier for example, the electron-hole recombination is used. In Raman amplifiers: the coherent photons are generated by the Raman scattering of the incoming light with phonons of the gain medium. In the case of REDFAs and bulk amplifiers, the stimulated emission process is exploited.

REDFAs are based on an active fiber doped with rare earth ions in its core. A pump (usually generated using a fibered laser diode) and a signal (the laser light that needs to be amplified) are coupled into the active single-mode fiber core using an optical combiner. The pump ensures the ion population inversion along the whole length of the active fiber. Thanks to this inversion, the signal is amplified through the stimulated emission during all its propagation along the fiber. Figure II.6 represents the basic schematic setup of an REDFA designed with a forward pumping configuration.

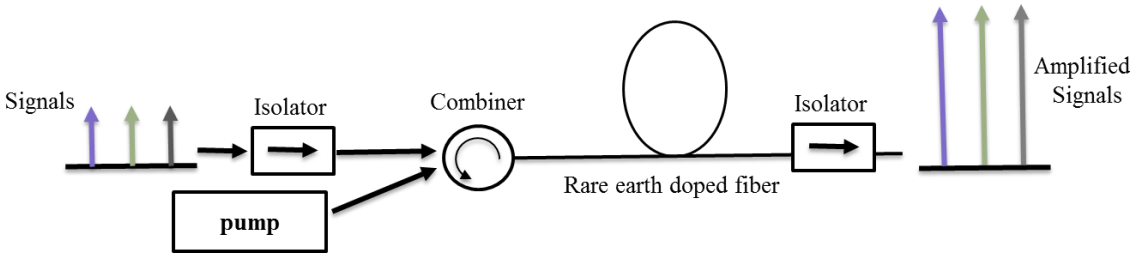

Figure II.6. Basic schematic of a rare earth doped fiber amplifier (REDFA) setup designed with a forward pumping configuration

The amplifier performances (its gain and noise figure) strongly depend on the homogeneity of the population inversion along its active fiber. In the forward configuration, the signal and the pump are injected from the same side of the fiber: the amplifier input. This architecture induces a high consumption of the pump power along the first portions of the fiber. If the pump power is not strong enough, a low population inversion on the other side of the fiber (output side of the amplifier) can occur, reducing the amplification efficiency. This inhomogeneity in the distribution of the pump power is detrimental for both the amplifier gain and its noise figure.

Other pumping configurations can be used to avoid or limit such issues. The backward pumping (A/) consists in injecting the pump from the opposite fiber side of the signal (Figure II.7.A). The pump power is then distributed in agreement with the signal power distribution: the population inversion is better at the output side of the fiber where the signal power is higher. This scheme allows a better amplification performance in terms of gain and noise figure even if the pump power is still not homogenously distributed along the fiber length. The double-pumping configuration (also called bidirectional pumping, B/) consists in dividing the pump power and injecting it from both sides of the REDFA (Figure II.7.B). This configuration gives the best pump distribution along the active fiber resulting in the best population inversion homogeneity and then usually ensures the best amplification.

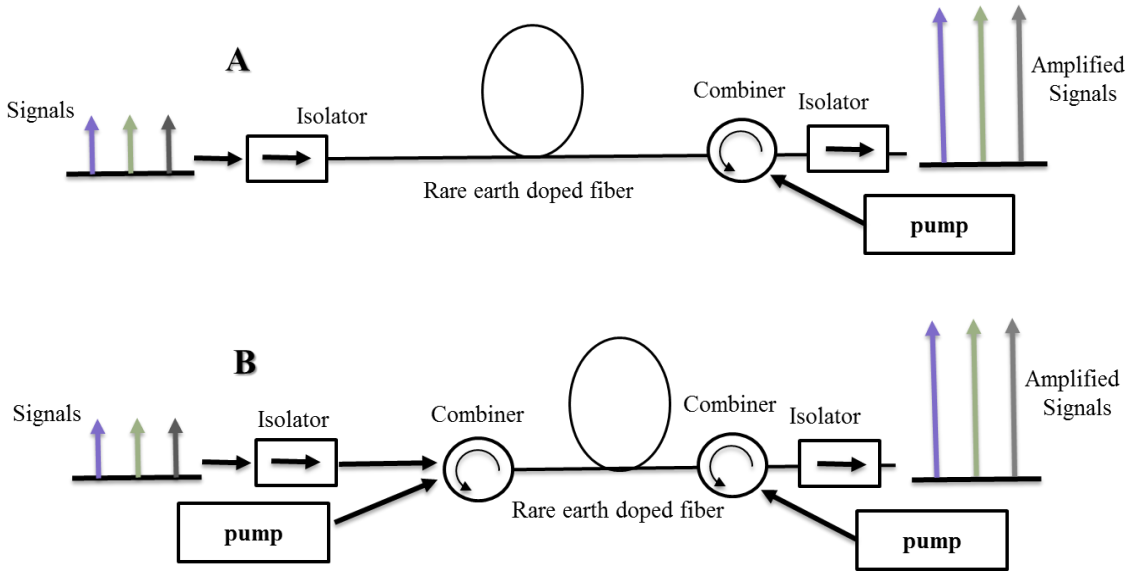

Figure II.7. Different pumping configuration architectures for rare earth doped fiber amplifier REDFAs, A. backward pumping scheme, B. Bidirectional pumping configuration

II.4.2 Gain spectrum and Gain saturation

The optical pumping of the EDFAs and EYDFAs provides the population inversion between the ${}^4I_{13/2}$ excited state and the ${}^4I_{15/2}$ ground state energy levels of the Erbium ions, which induces the optical gain described by Equation II.14.

$$g = \sigma(N_2 - N_1) \qquad \text{(II.14)}$$

Where σ is the transition cross section. N_1 and N_2 are the ions concentrations in the ground and excited state, respectively.

Contrary to the ideal homogenously broadened gain medium cross section, the gain spectrum of a REDFAs is strongly broadened by the amorphous nature of silica and by the presence of the codopants (such as P or Al) in the fiber core. This could be exploited to ensure the amplification of signals distributed over a larger range of wavelengths, eg WDM and DWDM amplifications for Telecom applications.

The gain of the amplifier decreases as the signal power increases, this phenomenon is usually known as 'the gain saturation in laser and amplifier systems'. In fact, the increase of the number of signal photons results in a faster depopulation of the excited state than the population inversion. In this case the gain can be written in the form of Equation II.15.

$$g = \frac{g_0}{1 + \frac{p}{p_s}} \qquad \text{(II.15)}$$

Where g_0 is the wavelength dependent signal gain coefficient for a small signal power, p is the signal power and p_s is the saturated signal power (the power required for the gain to drop by 3 dB). In other words, the signal power evolution over the fiber length can be expressed as Equation II.16.

$$\frac{dp}{dz} = g(z)P(z) = \frac{g_0(z)p(z)}{1 + \frac{p(z)}{p_s}} \qquad \text{(II.16)}$$

The Equation II.16 can be integrated over the fiber length giving Equation II.17.

$$p_{out} = p(L) = Gp_{in} \qquad \text{(II.17)}$$

By consequence the amplifier gain G can be calculated using the Equation II.18 [63].

$$G = G_0 \exp\left(-\frac{G-1}{G}\frac{p_{out}}{p_{in}}\right) \qquad \text{(II.18)}$$

Where G_0 is the unsaturated amplifier gain given by

$$G_0 = \exp\left(\int_0^L g_0(z)dz\right) \qquad \text{(II.19)}$$

II.4.3 Amplifier Noise

II.4.3.A The amplifier noise quantum limit

A linear amplifier adds noise to any signal it processes. In fact, the added noise must be at least the equivalent to the double of the zero-point noise associated with the input signal. This leads to a SNR (Signal-to-Noise Ratio) of at least 3 dB in a linear phase-insensitive amplifier (which does not consider the phase of the input light) [64].

In a configuration where the signal is coupled to an inverted atomic population, and using a quantum mechanics approach, the electrical field E_0 and the photon number η_0 of the input signal evolution induced by a linear amplifier can be calculated. It was demonstrated in [65] that a relation between the output and the input SNR can be derived for both the electric field and the photon number as demonstrated in Equations II.20 and II.21, respectively.

$$\left(\frac{S}{N}\right)_{out} = \frac{G}{2n_{sp}(G-1)+1}\left(\frac{S}{N}\right)_{in} \qquad \text{(II.20)}$$

$$\left(\frac{S}{N}\right)_{out} = \frac{G^2\langle n_0\rangle}{n_{sp}^2(G-1)^2 + n_{sp}(G-1) + 2n_{sp}(G-1)G\langle n_0\rangle + G\langle n_0\rangle}\left(\frac{S}{N}\right)_{in} \qquad \text{(II.21)}$$

Where G is the amplifier gain, n_{sp} is the population inversion factor and $<n_0>$ is input-photons number.

Equations II.20 and II.21 show that the SNR directly depends on the gain and the population inversion factor of the amplifier. The minimum noise is obtained when a full population inversion is reached $(n_{sp} \approx 1)$. In such condition, and for a high amplifier gain $(G \gg 1)$ and a large photon number input $(\langle n_0 \rangle \gg 1)$, Equation II.21 can be reduced to Equation II.22.

$$\left(\frac{S}{N}\right)_{out} = \frac{1}{2}\left(\frac{S}{N}\right)_{in} \qquad \text{(II.22)}$$

The Equation (II.22) is the SNR quantum limit.

II.4.3.B Amplified Spontaneous Emission Noise

The Amplified Spontaneous Emission (ASE) physical picture is an effective way to explain the intrinsic noise present in all atomic population inversion based amplifiers. Basically, the amount of noise photons which are generated by the random spontaneous decay of the excited ions are negligible compared to the ones of the stimulated emission. However, the ASE noise is amplified during its propagation along the pumped active fiber, as well as the stimulated emission. In other words, the higher the gain, the greater the ASE noise. The signal mode associated noise power can be calculated using Equation II.23.

$$p_{ASE} = h\nu n_{sp}(G(\nu)-1)\Delta\nu \qquad \text{(II.23)}$$

Where $\Delta\upsilon$ is the frequency bandwidth.

This power strongly depends on n_{sp}. In order to reduce the ASE noise, the population inversion factor needs to be close to 1 $(n_{sp} \approx 1)$. This can easily be achieved using a four level system as in the case of ErYb codoped amplifiers. On the other hand, in three levels systems as in the case of EDFA, this condition can be achieved only using a very strong pump power [66].

II.4.3.C Amplifier Noise Figure

The noise performance of an optical amplifier cannot be described only by the noise power calculated using Equation II.21. As the SNR is the ultimate limitation of a detection system, the NF (Noise Figure) is commonly used to characterize the amplifier. It is defined using Equation II.24.

$$NF = \frac{SNR_{in}}{SNR_{out}} \qquad \text{(II.24)}.$$

In this second chapter, we introduce the basic mechanisms involved in the amplification process for ions in general and REs (Er and Yb) more particularly. The described phenomena were used to build the rate equations of our simulation tool used to calculate the energy levels populations of the active ions embedded in the REDF. We also present the different host matrix used to incorporate these ions in the fiber core, highlighting the necessity to add P and/or Al elements to enhance the REDFAs amplification performances. Finally, we described the different amplifiers architectures that are considered in literature and detailed how are characterized the REDFAs main performance criteria: its optical gain and its noise figure.

EN

Dans ce chapitre, les mécanismes de base impliqués dans le processus d'amplification sont introduits pour les ions en général et pour les ions Terres Rares (Er et Yb) plus particulièrement. Ces différents phénomènes sont pris en compte pour élaborer l'outil de simulation incluant les équations de populations des différents niveaux d'énergies des ions actifs incorporés dans les REDFs. Les différentes matrices vitreuses permettant une incorporation efficace de ces ions Terres Rares sont décrites explicitant la nécessité d'ajouter du P et/ou de l'Al afin d'optimiser les performances des ???. Finalement, les différentes architectures possibles pour les REDFAs sont présentées ainsi que les critères permettant de caractériser les performances d'un amplificateur optique, à savoir son gain optique et sa figure de bruit.

FR

In questo secondo capitolo, i meccanismi di base coinvolti nel processo di amplificazione sono introdotti per gli ioni in generale e in particolare per le quelli delle Terre Rare (Er e Yb). Questi diversi fenomeni sono stati considerati per sviluppare le equazioni di popolazione dei differenti livelli energetici degli ioni attivi incorporati nel REDF, equazioni necessarie per la realizzazione della simulazione. Le diverse matrici amorfe che permettono l'incorporazione efficace degli ioni di Terre Rare sono descritti, mettendo in evidenza la necessità di aggiungere elementi come P e/o Al per migliorare le prestazioni di amplificazione degli REDFA. Infine, le diverse architetture degli amplificatori sono presentate, insieme ai criteri che permettono di caratterizzare le prestazioni degli amplificatori ottici, come il guadagno ottico e la figura di rumore.

IT

Chapter III
Simulation Procedure

III.1 INTRODUCTION

The physics involved in the REDFAs amplification process is quite complex. In order to simulate the REDFAs behaviors, two issues need to be overcomed. The first regards the rate equations system modeling the ion population of the energy levels. The second, pertains the modelling of the optical powers propagation along the fiber length at different wavelengths [67].

The numerical code requires two different classes of input data; one related to the fiber spectroscopic parameters (emission and absorption cross sections, energy levels lifetimes, transition rates, etc …) and another one related to the amplifier parameters: signal and pump wavelengths and powers, pumping configuration, fiber lengths and losses, etc.

Figure III.1 represents the diagram of the developed simulation procedure showing the main core of the code based on the Particle Swarm Optimization (PSO), the two subroutines where the rate equations and the power propagations equations are solved using a globally convergent Newton's method for solving nonlinear system of equations and a relaxation algorithm for solving two point boundary value problem. The input and output data of the simulation are represented in grey and green, respectively.

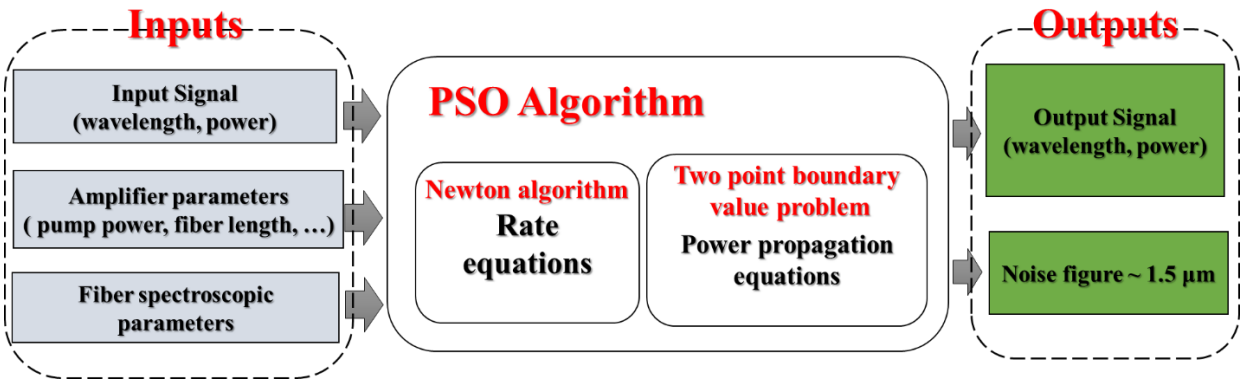

Figure III.1 Diagram of the simulation procedure used in our numerical model.

III.2 CODE INPUT

The REDFAs modeling and design require some experimental data as inputs. The accuracy of the simulation strongly depends on such input values. In this section, the overlap factor parameters and the procedure allowing the evaluation of both absorption and emission cross sections will be described. Other inputs such as spectroscopic parameters, geometrical and physical parameters of the optical fiber are reported in *Section VI.2*.

III.2.1 Overlapping factors

The overlap factor represents the parameter quantifying the overlap between the electromagnetic field distribution and the doped region of the optical fiber (generally the fiber core). The calculation of such parameter is performed by considering the refractive index profile. Thereafter, the overlap factors at the pump and signal wavelengths $\Gamma(\lambda_p)$ and $\Gamma(\lambda_s)$ are described by the Equation III.1.

$$\Gamma(\lambda_{p,s}) = \int_0^{2\pi}\int_0^{R} \left|E(r,\theta,\lambda_{p,s})\right|^2 r dr d\vartheta \qquad \text{(III.1)}$$

Where *R* is the radius of the doped core and E is the normalized transverse electric field envelope so that:

$$\int_0^{2\pi}\int_0^{\infty} \left|E(r,\theta,\lambda_{p,s})\right|^2 r dr d\vartheta = 1 \qquad \text{(III.2)}$$

However, the electric field distribution is calculated by solving the eigenvalue Helmholtz equation for electric field using a full-vectorial solver based on finite element method (COMSOL Multiphysics in our case) [68].

Figure III.2 illustrates an example of the normalized electric field at both pump and signal wavelengths as well as the measured refractive index profile of an Erbium-Aluminosilicate-codoped single mode fiber: the mode profile spreading at larger wavelengths is clearly observed.

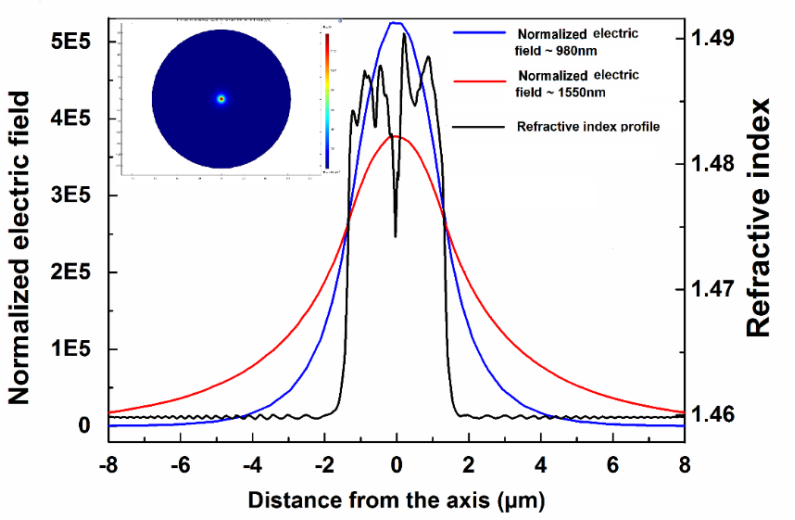

Figure III.2. Measured refractive index profile of an Erbium-Aluminosilicate-codoped single mode fiber and calculated radial distributions of the normalized electric field at the pump and signal wavelengths. The inset illustrates the 2D electric field distribution of the guided mode at 1550 nm.

III.2.2 Ions emission and absorption cross sections

The optical transition cross sections are used to quantify the probability of optically induced transition events. The cross section (expressed in m^2) starting from a certain electronic level is defined so that the rate of the optical transitions (per active ion) is the transition cross section σ times the photon flux [69]. In some cases, (as for the RE ions doped glasses), this concept often cannot be directly applied to optical transitions, since the Stark level manifolds contain multiple electronic sublevels with slightly different energies. As result, the concept of effective cross sections is more used. In particular, the effective cross section can be calculated directly from the absorption and emission spectra knowing some parameters such as the ion concentration and the optical energy distribution.

In the case of Er^{3+} doped fibers, the absorption cross section for the $^4I_{15/2} \rightarrow {}^4I_{13/2}$ transition is determined from the measured absorption spectrum using the following Equation:

$$\sigma_{Er}^{a}(\lambda_k) = \frac{A(\lambda_k)}{4.343\Gamma(\lambda_k)N_{Er}} \qquad \text{(III.3)}$$

where $A(\lambda_k)$ is the measured attenuation expressed in dB/m, evaluated using the cutback method and N_{Er} is the Erbium concentration.

In the case of high power Yb^{3+} and Er^{3+}/Yb^{3+} co-doped fiber amplifiers, high signal and pump powers are involved in the amplification and a double clad fiber geometry is required (see Section IV.2.3). In this configuration, the fiber is multimode at the pump wavelengths and the evaluation of the overlap factor becomes more complex using the method described in section III.2.1. In order to overcome this drawback, the approximation $\Gamma(\lambda_k) = \frac{S_{core}}{S_{clad}}$ can be used, with S_{core} and S_{clad} the core and the first cladding surfaces, respectively.

Considering this approximation, the $^2F_{7/2} \rightarrow {}^2F_{5/2}$ cross section transition of Yb^{3+} ions can be evaluated using the equation

$$\sigma_{Yb}^{a}(\lambda_k) = \frac{A(\lambda_k) S_{clad}}{4.343 N_{Yb} S_{core}} \qquad \text{(III.4)}$$

The emission spectrum is difficult to be measure experimentally; as it strongly depends on the excitation power and wavelength. On the other hand, the absorption cross section characterization is easier to characterize since, as highlighted by equation III.3, it can be inferred using the absorption spectrum that is an absolute measurement. The emission cross section can then be calculated starting from its absorption cross section using the McCumber theory [70]; relating the emission cross section to the absorption one for an ion in a solid-state laser and expressed by:

$$\sigma_{Er,Yb}^{e}(\lambda_k) = K \sigma_{Er,Yb}^{a}(\lambda_k) \exp\left(\frac{\varepsilon - h\nu_k}{k_B T}\right) \qquad \text{(III.5)}$$

where k_B and h are the Boltzmann and Planck constants, respectively, $\nu_k = c/\lambda_k$ is the light frequency, ε is the energy gap between the upper and lower manifolds, T is the absolute temperature and K is a constant value calculated using the equation:

$$K = \frac{\sum_{j=1}^{N} \exp\left(-E_{1,j}/k_B T\right)}{\sum_{j=1}^{M} \exp\left(-E_{2,j}/k_B T\right)} \qquad \text{(III.6)}$$

E_{1j} and E_{2j} being the sublevels energies of the fundamental and excited manifolds, respectively [71]. Moreover, ε can be obtained from the highest absorption peak.

An example of the calculated emission and measured absorption cross sections of Er^{3+} ions in an aluminosilicate host matrix and for Yb^{3+} ion in a phosphosilicate network are reported in Figures III.3.A and III.3.B.

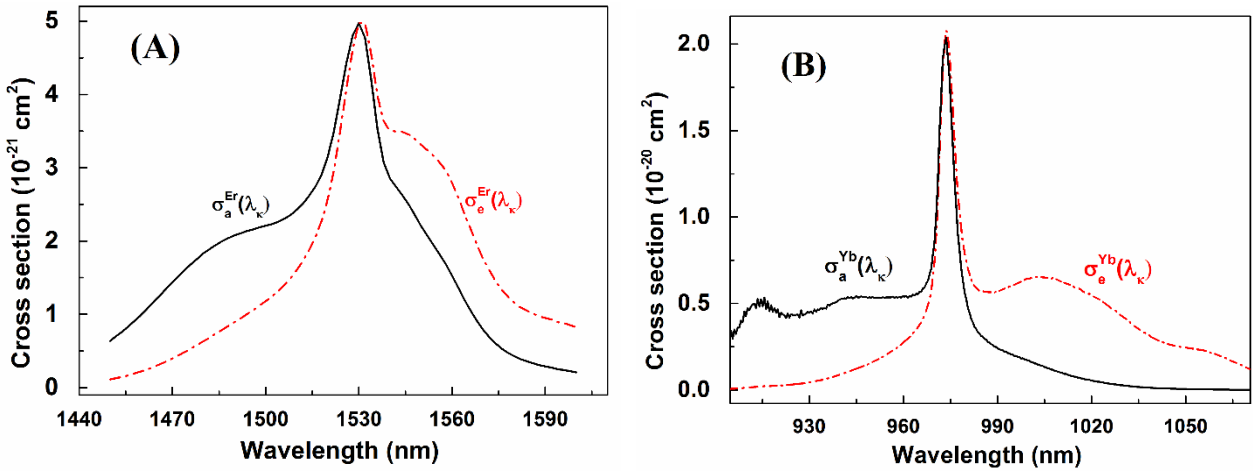

Figure III.3. Calculated emission and measured absorption cross sections of: A) Er^{3+} ions in an aluminosilicate host matrix and B) Yb^{3+} ions in a phosphosilicate network.

III.3 RATE EQUATIONS

To model the amplification process in REDFAs, a set of multilevel rate equations (describing the population in the different energy levels) have to be resolved. The energy level diagram of the RE doped system including i) absorption and stimulated emission at both pump and signal wavelengths, ii) spontaneous radiative decays and fast nonradiative multiphonon relaxation, iii) cross relaxation and cooperative upconversion, vi) ion-ion energy transfer processes have to be considered.

The rate equation depends on the different ions involved in the amplification phenomenon as well as on their interaction with the excitation light and the ions-ions interactions. In our case, the amplification process in Erbium and Erbium/Ytterbium doped amplifiers has been considered.

III.3.1 Rate equations model

The Erbium/Ytterbium amplification system is generally used to obtain high output powers amplifiers. The Ytterbium-codoping is used since it exhibits high absorption cross section at the pumping wavelength. In the case of a phosphosilicate glass matrix, the energy transfer from the Yb^{3+} $^2F_{5/2}$ energy level to the Er^{3+} $^4I_{11/2}$ energy level is strongly enhanced. In some cases, (with an appropriate Yb/Er and P/Yb ratio) about 90-95 % of the excitation energy absorbed by the Yb^{3+} ions is transferred to the Er^{3+} ones. The Figure III.4 illustrates the Er/Yb energy levels system considered in our model.

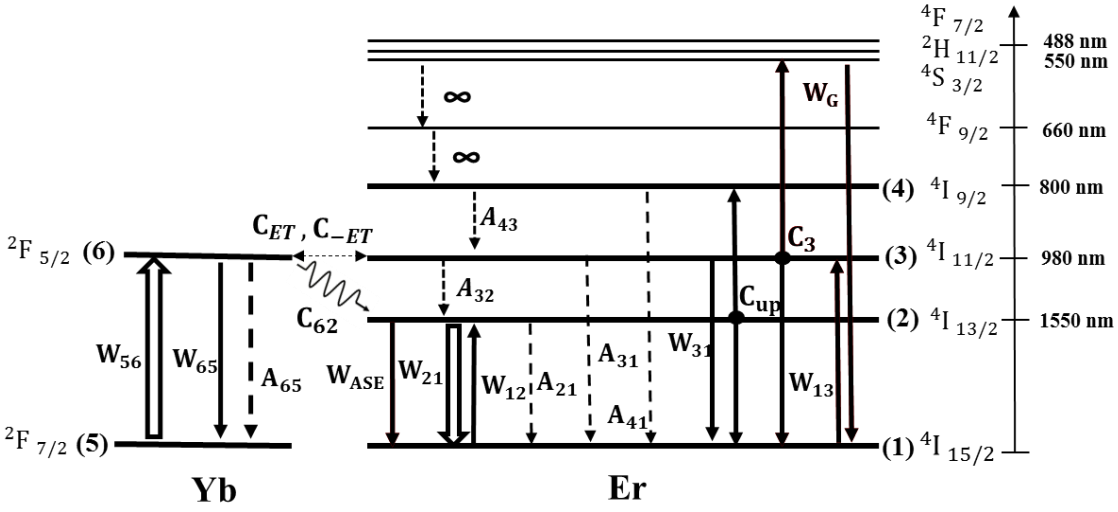

Figure III.4. Energy levels diagram of an Er^{3+}/Yb^{3+} system.

The excitation, at pumping wavelength of about 915 nm, is resonant with the $^2F_{7/2} \rightarrow {}^2F_{5/2}$ and at pumping wavelength of about 980 nm with the $^4I_{15/2} \rightarrow {}^4I_{11/2}$ transitions, and the signal beam (at about 1550 nm) with the $^4I_{13/2} \rightarrow {}^4I_{15/2}$ transition. The ions lying at energy level $^4I_{11/2}$ predominantly relax to level $^4I_{13/2}$ by means of a mostly non-radiative decay. Particularly, in an aluminosilicate or a phosphosilicate host matrix, this transition is enhanced and promote to the radiative transition to the $^4I_{15/2}$ level. As the signal beam propagates along the fiber, it is amplified by stimulated emission due to the $^4I_{13/2} \rightarrow {}^4I_{15/2}$ transition.

The co-doping with Yb^{3+} improves the pump absorption efficiency, too. In fact, the large spectral overlap between the $^2F_{5/2} \rightarrow {}^2F_{7/2}$ transition of Yb^{3+} ions and $^4I_{15/2} \rightarrow {}^4I_{11/2}$ transition of Er^{3+} results in an efficient resonant-energy transfer from $^2F_{5/2}$ level to $^4I_{11/2}$ one. However, the loss channels

limiting the gain performance such as cooperative up-conversion processes of both $^4I_{13/2}$ (C_{up}) and $^4I_{11/2}$ (C_3)Er^{3+} energy levels as well as the ASE noise are also considered in the simulation.

The populations of Er^{3+} and Yb^{3+} energy levels are expressed by the following steady-state rate equations

$$W_{12}N_1 - (W_{ASE} + A_{21} + W_{21})N_2 + A_{32}N_3 - 2C_{up}N_2^2 + C_{62}N_2N_6 = 0 \quad \text{(III.7)}$$

$$W_{13}N_1 - (W_{31} + A_{32} + A_{31})N_3 - C_3N_3^2 + A_{43}N_4 - 2C_3N_3^2 + C_{ET}N_1N_6 - C_{-ET}N_3N_5 = 0 \quad \text{(III.8)}$$

$$C_{up}N_2^2 - A_{43}N_{46} = 0 \quad \text{(III.9)}$$

$$(W_{65} + A_{65})N_6 - W_{56}N_5 - C_{ET}N_1N_6 + C_{-ET}N_3N_5 - C_{62}N_2N_6 = 0 \quad \text{(III.10)}$$

$$N_1 + N_2 + N_3 + N_4 - N_{Er} = 0 \quad \text{(III.11)}$$

$$N_5 + N_6 - N_{Yb} = 0 \quad \text{(III.12)}$$

where N_{Er} and N_{Yb} are respectively the Er^{3+} and Yb^{3+} dopants concentrations in the fiber core, N_i (i=1, 2…, 6) are the ions concentration of the different energy levels, $A_{ij} = 1/\tau_{ij}$ $A_{ij} = \frac{1}{\tau_{ij}}$ (with τ_{ij} is the lifetime of the *i* level to *j* level and $\frac{1}{\tau_i} = \sum \frac{1}{\tau_{ij}}$) is the spontaneous radiative transition rate from the *i-th* to the *j-th* energy levels, W_{12} and W_{21} are respectively the absorption and stimulated emission transition rates between the $^4I_{15/2}$ and $^4I_{13/2}$ energy levels of Er^{3+} ions at the signal wavelength (λ_s) calculated using the equation Equation III.13.

$$W_{ij}(z,\lambda_s) = \frac{\Gamma(\lambda_s)\sigma_{ij}(\lambda_s)\left[P_s^+(z) + P_s^-(z)\right]\lambda_s}{hcS_{core}} \quad \text{(III.13)}$$

Where P_s^+ and P_s^- are the forward and backward signal powers respectively, W_{13} and W_{31} are the absorption and stimulated emission transition rates between the $^4I_{15/2}$ and $^4I_{11/2}$ energy levels of Er^{3+} ions at pump wavelength (λ_p), W_{56} and W_{65} are the absorption and stimulated emission transition rates between the $^2F_{7/2}$ and $^2F_{5/2}$ levels of Yb^{3+} ions at pump wavelength, respectively. The amplified spontaneous emission rate due to the ASE noise is given by:

$$W_{ASE}(z)=\frac{1}{hcS_{core}}\sum_{k=1}^{M}\Gamma_{ASE}(\lambda_k)\sigma_{lm}(\lambda_k)\left[P_{ASE}^{+}(z)+P_{ASE}^{-}(z)\right]\lambda_k \quad (l,m=2,1) \qquad \text{(III.14)}$$

where M is the number of the wavelength slots sampling the noise frequency band. C_{up} and C_3 are respectively the $^4I_{13/2}$ and $^4I_{11/2}$ homogeneous cooperative up-conversion coefficients, C_{ET} and C_{-ET} are the energy transfer rates from $^2F_{5/2}$ to $^4I_{15/2}$ levels and from $^4I_{11/2}$ to $^2F_{7/2}$ levels, respectively. C_{62} is the secondary energy transfer rate from $^2F_{5/2}$ to $^4I_{13/2}$ levels, $\Gamma(\lambda_p)$ and $\Gamma(\lambda_s)$ are the overlap factors at the pump and the signal wavelengths, respectively. P_s , $P_p^{\pm}$ and $P_{ASE}^{\pm}$ are, the signal, the forward and backward propagating pump, and forward and backward ASE powers, respectively.

III.3.2 Rate equations for Erbium doped system

The case of an Erbium system is simpler compared to the one of Er/Yb. It can be obtained starting from the previous model by setting all the Yb-related coefficients and population values to zero. However, some changes on the population inversion and amplification parameters need to be done. Figure III.5 represents the diagram of an Erbium system and the different processes involved in the amplification.

To simplify the model, we assume that the $^4F_{7/2}$, $^2H_{11/2}$, $^4S_{3/2}$ and $^4F_{9/2}$ energy levels are empty since they immediately relax to the $^4I_{9/2}$ as their lifetimes are very small compared to the other levels inducing very high transition rates.

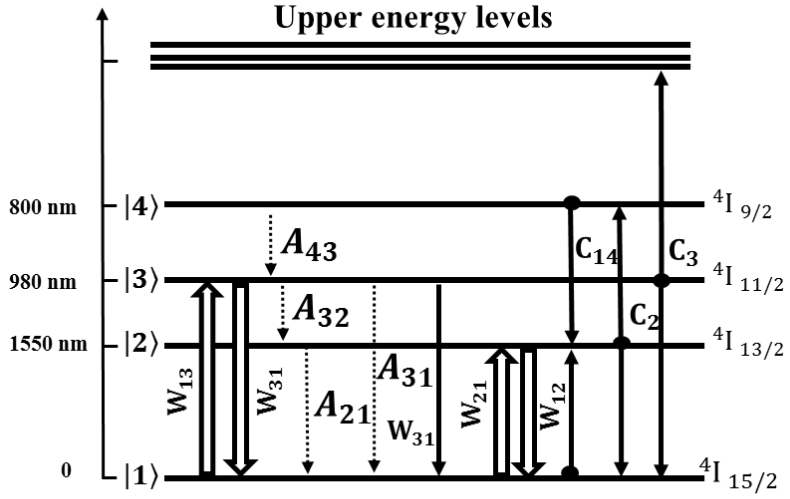

Figure III.5. Energy level diagram of transitions in the Er^{3+}-doped system considered in our model under 980 nm pump excitation.

At steady state, the rate equations of the Er^{3+}-doped system are the following:

$$-\frac{N_4}{\tau_{43}} + C_2 N_2^2 + C_3 N_3^2 - C_{14} N_1 N_4 = 0 \quad \text{(III.15)}$$

$$W_{13} N_1 - W_{31} N_3 - \frac{N_3}{\tau_{32}} + \frac{N_4}{\tau_{43}} - 2C_3 N_3^2 = 0 \quad \text{(III.16)}$$

$$W_{12} N_1 - W_{21} N_2 + \frac{N_3}{\tau_{32}} - \frac{N_2}{\tau_{21}} - 2C_2 N_2^2 + 2C_{14} N_1 N_4 = 0 \quad \text{(III.17)}$$

$$N_1 + N_2 + N_3 + N_4 = N_{Er} \quad \text{(III.18)}$$

where N_i, $i = 1,2,3,4$ are the population densities of the energy levels, $1/\tau_{ij}, i = 2,3,4$ and $j = 1,2,3$ are the spontaneous transition rates from level N_i to level N_j, C_2 and C_3 are the coefficients of the cooperative and up-conversion processes $2\,^4I_{13/2} \rightarrow {}^4I_{15/2} + {}^4I_{9/2}$, $2\,^4I_{11/2} \rightarrow {}^4I_{15/2} + {}^4S_{3/2}$, respectively. C_{14} is the coefficient of cross relaxation process $^4I_{15/2} + {}^4I_{9/2} \rightarrow 2\,^4I_{13/2}$, W_{13} and W_{31} are the absorption and stimulated emission transition rates for the ground state $^4I_{15/2}$ and $^4I_{11/2}$ level, W_{12} and W_{21} are the absorption and stimulated emission transition rates for the ground state and the metastable one $^4I_{13/2}$ and N_{Er} is the Erbium concentration.

III.3.3 Rate Equation solver

The false position and the bisection methods are usually used to find the roots of a nonlinear equation $f(x) = 0$ requiring bracketing of the root by two guesses. Thereof, those methods are called 'bracketing methods'. These methods are always convergent since they are based on reducing the interval between the two guesses so as to zero in on the root of the equation.

On the contrary, in the Newton-Raphson one, the root is not bracketed. In this case, only one initial guess of the root is needed to get the iterative process to start for solving $f(x) = 0$ equation. Thereby, the Newton-Raphson method belongs to open methods category. Convergence in open

methods is not guaranteed. However, if the method does converge, it does so much faster than the bracketing methods [72]. Such property renders this method very interesting to solve complex equation systems as the rate equations in our case with a lower computational burden.

III.3.3.A 1D Newton's Method Algorithm

Considering the Taylor-series expansion of the function $f(x)$ around a value $x = x_0$:

$$f(x) = f(x_0) + f'(x_0)(x - x_0) + (f"(x_0)/2!)(x - x_0) + \cdots. \quad \text{(III.19)}$$

A first approximation to the root of the equation $f(x) = 0$ can be obtained using only the first two terms of the expansion obtaining

$$f(x1indice) \approx f(x_0) + f'(x_0)(x_1 - x_0) = 0 \qquad \text{(III.20)}$$

Such approximation can be given by:

$$x_1 = x_0 - \left[\frac{f(x_0)}{f'(x_0)}\right] \qquad \text{(III.21)}$$

The Newton-Raphson method algorithm consists in improving the values of the approximated root through the recursive application of equation III.20. This iterative procedure can be generalized by the Equation III.22.

$$x_{(i+1)} = x_i - \left[\frac{f(x_i)}{f'(x_i)}\right] \qquad \text{(III.22)}$$

where i is the iteration counter. The convergence condition is checked after each iteration and the algorithm stops when a user defined error is reached. Generally, the stop condition is defined by the equation

$$|f(x_{(i+1)})| < \varepsilon \qquad \text{(III.23)}$$

where ε is the user defined error value.

Figure III.6 illustrates the way in which the Newton-Raphson method converges to find the solution of the equation $f(x) = 0$ (for a one-dimensional problem).

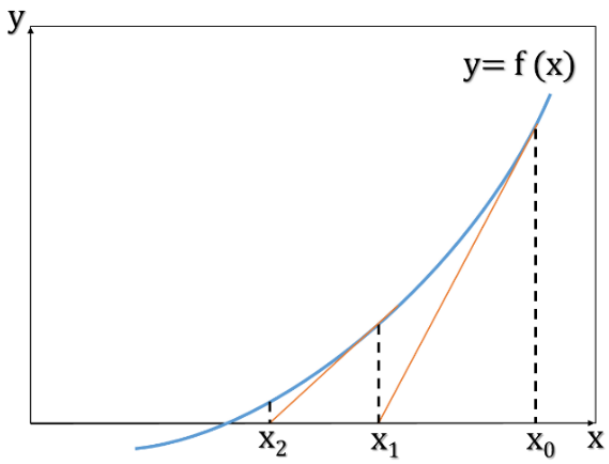

Figure III.6 Graphic illustration of the Newton-Raphson method convergence steps in founding the root of $f(x) = 0$.

It's important to notice that the equation $f(x_0) + f'(x_0)(x_1 - x_0)$=0 represents a straight-line tangent to the curve $y = f(x)$ at $x = x_0$. The intersection of this line with the x-axis gives the new x position ($x_1 = x_0 - [f(x_0)/ f'(x_0)]$). At that point another straight-line tangent can be defined and so on. Proceeding with this iteration the intersection of consecutive tangent lines with the x-axis approaches the actual root relatively fast [73].

III.3.3.B Newton-Raphson Method for Multidimensional Equations Systems

There is no good general method to solve a multidimensional equations system. Considering the case of two dimensions, the following equations have to be solved

$$f(x, y) = 0 \qquad \text{(III.24)}$$

$$g(x, y) = 0 \qquad \text{(III.25)}$$

f and g are two arbitrary functions, each one has zero contour lines that divide the (x,y)-plane into positive or negative function regions. The solutions are those points that are common to the zero contours of f and g as it is represented in Figure III.7.

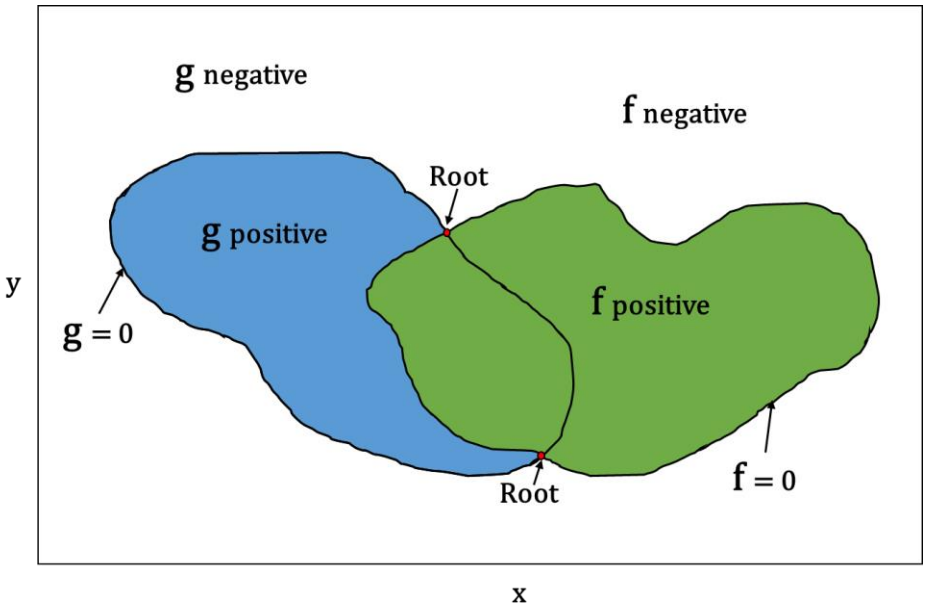

Figure *III.7*. Graphic illustration of solutions of two nonlinear equations with two unknowns

In general, the functions f and g have no relation to each other. In other words, there is nothing special about a common point from either *f* 's point of view, or from *g*'s. A map out of the full zero contours of both functions need to be done in order to find all common points (which are the solutions of the nonlinear equations). In general, in a multidimensional problem, the zero contours will consist of an unknown number of disjoint closed surfaces virtually impossible to found without insight.

The Newton-Raphson method is one of the simplest multidimensional root-finding methods. With a sufficiently good initial guess, this method gives a very efficient means of converging to a root. Otherwise, it can also easily fail to converge, indicating that the aimed root does not exist nearby.

The global Newton-Raphson method is set as following:

If we take a typical problem gives N functional relations to be zeroed, involving variables x_i, where $i = 0, 1, \ \dots, \ N-1$.

$$\begin{cases} f_0(x_0, x_1, \dots, x_{N-1}) & = 0 \\ f_1(x_0, x_1, \dots, x_{N-1}) & = 0 \\ \vdots & \\ f_{N-1}(x_0, x_1, \dots, x_{N-1}) & = 0 \end{cases} \qquad \text{(III.26)}$$

We set **x** as the vector of entire values of x_i and **F** the vector of entire values of the functions f_i. In the neighborhood of x, each of the functions f_i can be expanded in Taylor series (Equation III.27).

$$F_i(\boldsymbol{x} + \delta\boldsymbol{x}) = F_i(\boldsymbol{x}) + \sum_{j=0}^{N-1} \frac{\partial F_i}{\partial x_j} \delta x_j + O(\delta \boldsymbol{x}^2) \qquad \text{(III.27)}$$

The partial derivatives matrix appearing in Equation III.27 is the Jacobian Matrix **J** where

$$J_{ij} = \frac{\partial F_i}{\partial x_j} \qquad \text{(III.28)}$$

In this way, the Equation III.27 can be rewritten as

$$\mathbf{F}(\mathbf{x} + \delta\mathbf{x}) = \mathbf{F}(\mathbf{x}) + \mathbf{J} \cdot \delta\mathbf{x} + O\left(\delta\mathbf{x}^2\right) \qquad \text{(III.29)}$$

By neglecting the terms of second order ($\delta \boldsymbol{x}^2$) and higher, and by setting $F_i(\boldsymbol{x} + \delta\boldsymbol{x}) = 0$, the corrections $\delta\boldsymbol{x}$ is obtained by a set of linear equations that move each function closer to zero simultaneously.

$$\mathbf{J}\, \delta\boldsymbol{x} = -\mathbf{F} \qquad \text{(III.30)}$$

The equation matrix III.30 can be solved by LU decomposition as described in Equation III.31. The corrections are then added to the solution vector.

$$\mathbf{x}_{i+1} = \mathbf{x}_i + \delta\mathbf{x} \qquad \text{(III.31)}$$

III.3.3.C Globally Convergent Methods for Nonlinear Systems of Equations

As previously explained, the use of the Newton's method for solving multidimensional, nonlinear, equations has an unfortunate tendency to diverge if the initial guess is not well chosen (not sufficiently close to the root). In order to overcome this drawback, a global minimization method should be used. To this aim, in the developed numerical code the quasi-Newton method has been implemented to solve the nonlinear? system of equations in multidimensional space.

The algorithm combines the Newton's method (rapid local convergence) with a higher-level strategy that guarantees at least some progress at each step. Usually, this method can identify if

there is a root in the chosen region or not (the method recognizes the problem and signals failure). On the other hand, the Newton's method can run forever in the interval without convergence. This implemented method is structured as following

From Equation III.30, we can obtain:

$$\delta \mathbf{x} = -\mathbf{J}^{-1}\mathbf{F} \qquad \text{(III.32)}$$

where δx needs? to be cheeked after each iteration to reduce the divergence occurrence. A reasonable strategy is to require that the step decrease if we were trying to minimize.

$$f = \frac{1}{2}\mathbf{F}\mathbf{F} \qquad \text{(III.33)}$$

Every solution $F = 0$ minimizes the Equation III.33, but there may be local minima that are not solutions to $F = 0$. In order to develop a better strategy, we should consider that the Newton step (Equation III.32) is a descent direction for f.

$$\nabla \mathbf{f}\, \delta \boldsymbol{x} = (\mathbf{F}\mathbf{J})(-\mathbf{J}^{-1}\mathbf{F}) = -\mathbf{F}\mathbf{F} < 0 \qquad \text{(III.34)}$$

The strategy developed in [74] is quite simple and can be resumed in the following steps.
Full Newton step is applied at first. Because once the solution is close enough, a quadratic convergence will be obtained. However, at each iteration, the proposed step is checked if it reduces f. If not, a 'backtrack' along the Newton direction is applied until an acceptable step is obtained. Since Newton step is a descent direction for f, it is quite sure to find an acceptable step by backtracking.

III.4 PROPAGATION EQUATIONS

III.4.1 Propagation equations model

In Er^{3+}/Yb^{3+}-codoped-fiber-amplifiers, the signal is amplified during its propagation along the pumped-fiber-doped-core (the pump power is converted to signal photons). The power evolutions along the fiber longitudinal z-axis are described with the propagation equations for the signal (P_s

), the forward and backward propagating pump ($P_p^{\pm}$), and the amplified spontaneous emission ($P_{ASE}^{\pm}$) powers.

$$\frac{dP_s(z)}{dz} = \Gamma_s(\lambda_s) g_s(\lambda_s) P_s(z) - \alpha(\lambda_s) P_s(z) \quad \text{(III.36)}$$

$$\frac{dP_p^{\pm}(z)}{dz} = \pm\Gamma_p a_p(\lambda_p) P_p^{\pm}(z) \mp \alpha(\lambda_p) P_p^{\pm}(z) \quad \text{(III.37)}$$

$$\frac{dP_{ASE}^{\pm}(z,\lambda_k)}{dz} = \pm\Gamma_{ASE}(\lambda_k) g_s(\lambda_k) P_{ASE}^{\pm}(z,\lambda_k) \mp \alpha(\lambda_k) P_{ASE}^{\pm}(z,\lambda_k) \pm P_{0k} \quad \text{(III.38)}$$

where

$$g_s(\lambda_s) = \sigma_{21}(\lambda_s) N_2 - \sigma_{12}(\lambda_s) N_1 \quad \text{(III.39)}$$

$$a_p(\lambda_p) = \sigma_{31}(\lambda_p) N_3 - \sigma_{13}(\lambda_p) N_1 + \sigma_{65}(\lambda_p) N_6 - \sigma_{56}(\lambda_p) N_5 \quad \text{(III.40)}$$

$$P_{0k} = \frac{2hc^2}{\lambda_k^3} \Delta\lambda_k \Gamma_{ASE}(\lambda_k) \sigma_{21}(\lambda_k) N_2 \quad \text{(III.41)}$$

+ and - signs denote the forward and backward propagating waves, respectively, λ_k is the k^{th} wavelength component and $\Delta\lambda_k$ is the ASE bandwidth at the k^{th} wavelength component. The term P_{0k} defined in Equation III.41 accounts for the spontaneous emission which is amplified along the fiber.

To solve a such set of differential Equations (III.36-III.38), the following boundary conditions have to be satisfied:

$$P_s(z=0) = P_{s,in} \quad \text{(III.42)}$$

$$P_p^{+}(z=0) = P_{p,in}^{+} \quad \text{(III.44)}$$

$$P_p^{-}(z=L) = P_{p,in}^{-} \quad \text{(III.45)}$$

$$P_{ASE}^{+}(z=0,\lambda_k) = 0 \quad \text{(III.46)}$$

$$P_{ASE}^{-}(z=L,\lambda_k) = 0 \quad \text{(III.49)}$$

In particular, considering that equations (III.42-III.49) generate a two-boundary values problem, an iterative forward and backward integration through the fiber has to be carried out until a

convergence criterion is fulfilled. Such criterion is to demand that the changes in gain from two successive iterations be within an error limit. In order to perform accurate calculations and minimize algorithm instabilities with the random occurrence of divergence, the following procedure has been implemented. In each step of integration are solely integrated signal, pump and ASE powers in the direction of propagation. In other words, forward-propagating powers are found by forward integration and backward-propagating powers are found by backward integration. The energy levels populations of Er^{3+} and Yb^{3+} ions at a given place of the fiber are calculated, with the use of equations III.7-III.15, with the integration from the calculated values of forward powers and stored values of backward powers found from a previously applied oppositely directed integration. The Figure III.8 illustrates the power propagation solving procedure for two successive iterations, where L represents the fiber length, ΔL the step-length and t the iteration number..

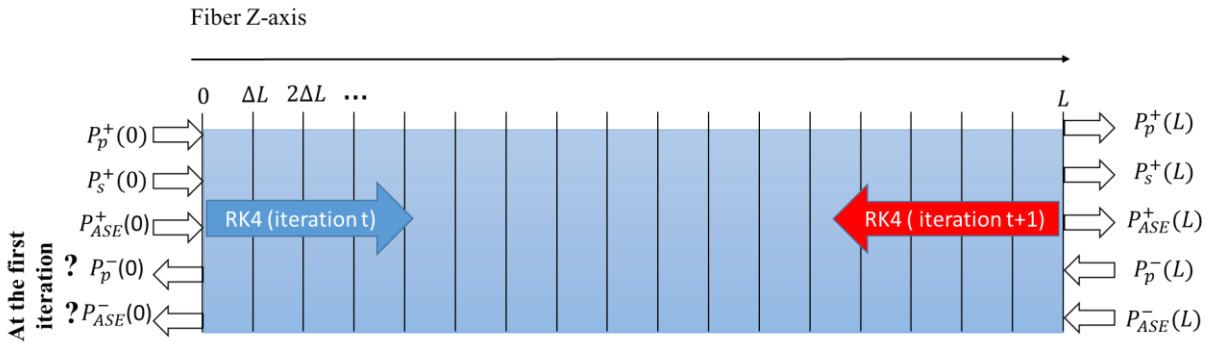

Figure III.8. Diagram of the power propagation solving procedure for two successive iterations

III.3.2 Propagation equations solver (Runge-Kutta Methods)

The Runge-Kutta methods in one of the most important class of one-step methods that are generically applicable to the ordinary differential equation systems (ODES). An ODES has one independent variable x, and N dependent variables $y_i\ (x)$ with $i = 1, 2, \dots, N$, usually, we are interested in a particular solution of a differential equation given a particular set of initial values of the variables.

The algorithm of the method can be set starting from the Euler formula

$$y_{n+1} = y_n + hf(x_n, y_n) \qquad \text{(III.50)}$$

The Equation III.50 advances a solution from x_n to $x_{n+1} \equiv x_n + h$. This formula is unsymmetrical. In other words, it advances the solution across an interval h. However, the derivative information is used only at the beginning of that interval, which means that the error step is one power of h smaller than the correction.

Euler's method is not recommended for practical use due to several reasons such as: the bad accuracy of the method compared to other methods, even if it runs at an equivalent step size, the low stability of the method.

However, the use of a step like in Equation III.50 is done by taking a "trial" step to the midpoint of the interval. The computation of the "real" step across the whole interval is done using the value of both x and y at that midpoint as described by following equations

$$k_1 = hf(x_n, y_n) \qquad \text{(III.51)}$$

$$k_2 = hf\left(x_n + \frac{1}{2}h, y_n + \frac{1}{2}k_1\right) \qquad \text{(III.52)}$$

$$y_{n+1} = y_n + k_2 + O(h^3) \qquad \text{(III.53)}$$

The first-order error term is wipe out using this summarization, which makes the method of the second order (A method is conventionally called n^{th} order if its error term is $n+1$ order $'O(h^{n+1})'$). Indeed, this method is called the second-order Runge-Kutta (also known as midpoint method). Based on that, many ways to evaluate the right-hand side $f(x, y)$ that all agree to the first order one can be cited, but with different higher-order error terms coefficients. The error terms can be eliminated order-by-order by adding up the right combination of these coefficients; the Runge-Kutta method is based on such criterion. Various specific formulas derived from this basic idea were given [75, 76]. The classical fourth-order Runge-Kutta formula is one of the most often used methods, and its formulation is described by the equations III.54 to III.58 [77].

$$k_1 = hf(x_n, y_n) \qquad \text{(III.54)}$$

$$k_2 = hf(x_n + \frac{h}{2}, y_n + \frac{k_1}{2}) \qquad \text{(III.55)}$$

$$k_3 = hf(x_n + \frac{h}{2}, y_n + \frac{k_2}{2}) \qquad \text{(III.56)}$$

$$k_4 = hf(x_n + h, y_n + k_3) \quad \text{(III.57)}$$

$$y_{n+1} = y_n + \frac{k_1}{6} + \frac{k_2}{3} + \frac{k_3}{3} + \frac{k_4}{6} + O(h^5) \quad \text{(III.58)}$$

The easy implementation and the good accuracy of the fourth-order Runge-Kutta made it a very appropriate method to be implemented into our code to solve the power evolution across the active fiber length.

III.5 OPTIMIZATION

The optimization is a key procedure for the treatment of complex systems. Mainly, the optimization using simulation, allowing the money and time saving by shortening the experimental study, also allow to study new configurations and methods that cannot be all tested through an experimental study. Thanks to the progresses in the calculation systems, the computational time is reduced and the efficiency is improved. The choice of the optimization procedure remains an important issue to ensure the best performance of the calculation code.

The computer-based optimization techniques can be classified into deterministic and stochastic methods. Stochastic search techniques are potentially able to find the global optima of the problem regardless the initial points, contrary to deterministic methods in which the final solution strongly depends on the initial values of the variables, Therefore, the so-called metaheuristics algorithms get a high interest because of their potential in solving large-scale problems efficiently, which was impossible by using deterministic ones.

Swarm intelligence offers insight into metaheuristics. In general, this technique concept is based on the interaction and information exchange between multiple agents. In particular, a swarm intelligence system consists of a population with members within their environment following simple rules and having characteristic behaviors and interacting locally with each other. Such simple systems can show more complex and a better self-organized behavior than the one of a stand-alone individual system. The resulting metaheuristic algorithms show a high capability to find global optima without being trapped in local extrema, and also made possible to solve nonlinear and discontinuous problems possibly characterized by great numbers of variables. Such

properties made them very interesting to the electromagnetic research community and among electromagnetic engineers as design tools and problem solvers [78, 79].

Metaheuristic algorithms are characterized by a good flexibility, efficiency, high adaptability and easy implementation. They also allow dealing with very complex fitness functions since the computation of derivatives is not needed during the optimization procedure. However, due to the strong stochastic behavior, these algorithms need a lot of iterations to get a meaningful result [80].

A variety of swarm intelligence-based optimization algorithms has been developed in order to solve different optimization problems. The efficiency of each algorithm as well as the solution accuracy depend on the problem descriptors and a number of unknowns. Those algorithms include particle swarm optimization, ant cuckoo search, firefly algorithm, artificial bee colony, bat algorithm, flower pollination algorithm, colony optimization, wolf search algorithm, artificial fish swarm algorithm, gray wolf optimization [80]. The choice of a proper algorithm is a key issue to increase the optimization efficiency (fast convergence, good accuracy, low computational resources, etc.). However, there is no general rules for this choice, yet. Typical features helping to a fair decision in this matter regard good convergence properties, ability to manage complex fitness function, ease of use and implementation, limited number of control parameters, computing time andgood exploitation of the parallelism offered by the modern computational architecture.

The PSO (Particle Swarm Optimization) has attracted the attention of many researchers which resulted in the development of many variants of the original algorithm relying on different parameter automation strategies. The parallel implementation of PSO allows the simultaneous evaluation of the fitness of all the agents involved in the procedure and substantially speeds up the optimization process. The PSO has been often used as an optimization algorithm because of its effectiveness in addressing hard problems. Moreover, compared to other evolutionary methods, the PSO scheme provides better results in a faster and cheaper way with fewer parameter adjustments.

III.5.1 General Definition of the PSO

The particle swarm optimization was proposed for the first time by J. Kennedy (social-psychologist) and R. Eberhart (engineer) in 1995 [81]. The method was inspired from the animal's

swarm behavior as birds, fish or bees (Figure III.9.A and III.9.B). This kind of swarm are characterized by a high efficiency to accomplish different tasks as searching for the best food location or avoiding a potential danger. Those performance are assured by the interaction and the fast communication between the different individual which called the 'Group intelligence'. In fact, each individual of the swarm is characterized by a position and a velocity (Figure III.9.C). Those parameters are related to the swarm general position and speed.

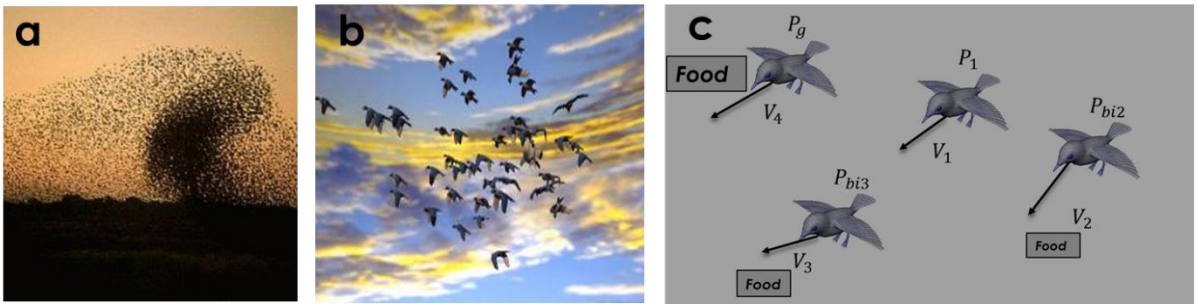

Figure III.9. a and b: illustration of a swarm of birds in nature, c: illustration of a bird's swarm as defined by the PSO

Form a mathematical point of view, the PSO consists to set a population (called the swarm) of potential candidate solution of the problem (called particles). Each particle is characterized by a position x_i in the solutions search-space. This position is updated using a velocity v_i which depend on the previous best position founded by the particle itself as well as the best position founded across all the swarm of particles. When the best position is reached, a new swarm is created around this new solution and the same process is repeated. The algorithm is stopped when all the particles converge on the same position. In other case the algorithm stops automatically when it reaches the maximum number of iterations (defined by the user).

III.5.2 The PSO Algorithm

The PSO algorithm is a population-based optimizer emphasizing the interaction between independent agents and the social or swarm intelligence. As in the other evolutionary computation, a number of particles are embedded in the swarm, each of them representing a potential candidate solution of the optimization problem. Each particle searches the global optimal point in the multi-dimensional solution space by adjusting its position according to its own experience (positions

founded by the particle in the previous iteration) as well as the experiences of other particles. In particular, each particle changes its position by simply varying its associated velocity taking into account the best position it has visited so far, called particle personal best, and the best position reached by all the particles during their paths, called global best.

If we consider a swarm of M particles in an N-dimensional search space, each swarm can be characterized by two matrices of the dimension $N \times M$, X will be the position matrix and V the velocity matrix:

$$X(t) = \begin{bmatrix} x_{11}(t) & x_{12}(t) & \cdots & x_{1M}(t) \\ x_{21}(t) & x_{22}(t) & \cdots & x_{2M}(t) \\ \vdots & \vdots & \vdots & \vdots \\ x_{N1}(t) & x_{N2}(t) & \cdots & x_{NM}(t) \end{bmatrix} \qquad \text{(III.59)}$$

$$V(t) = \begin{bmatrix} v_{11}(t) & v_{12}(t) & \cdots & v_{1M}(t) \\ v_{21}(t) & v_{22}(t) & \cdots & v_{2M}(t) \\ \vdots & \vdots & \vdots & \vdots \\ v_{N1}(t) & v_{N2}(t) & \cdots & v_{NM}(t) \end{bmatrix} \qquad \text{(III.60)}$$

where t is a pseudo-time unit increment (iteration number), $x_{nm}(t)$ is the n^{th} position element of the m^{th} particle at t^{th} iteration, $v_{nm}(t)$ is the n^{th} velocity element of the m^{th} particle at t^{th} iteration, every column $x_m(t)$ in matrix X is a possible solution for the problem. Moreover, the personal best position matrix X^b and the global best position vector G^b are introduced:

$$X^b(t) = \begin{bmatrix} {x^b}_{11}(t) & {x^b}_{12}(t) & \cdots & {x^b}_{1M}(t) \\ {x^b}_{21}(t) & {x^b}_{22}(t) & \cdots & {x^b}_{2M}(t) \\ \vdots & \vdots & \vdots & \vdots \\ {x^b}_{N1}(t) & {x^b}_{N2}(t) & \cdots & {x^b}_{NM}(t) \end{bmatrix} \qquad \text{(III.61)}$$

$$G = \begin{bmatrix} g_1(t) \\ g_2(t) \\ \vdots \\ g_N(t) \end{bmatrix} \qquad \text{(III.62)}$$

where $x^b{}_{nm}(t)$ is the n^{th} personal m^{th} particle best position element of t^{th} iteration, and $g_n(t)$ is the n^{th} global best position of the swarm at t^{th} iteration. For the first iteration (t=0), the swarm is randomly initialized and, subsequently, the position matrix is updated by the application of a suitable velocity matrix for each iteration as shown in the following equation:

$$X(t+1) = X(t) + V(t+1) \qquad \text{(III.63)}$$

The motion of the entire swarm towards the global optimum is defined by the update rule on the velocity field which represents the main PSO operator. The information on global and local best positions need to be properly processed in order to obtain the best update for the next iteration position. A right balance between cognitive and social perspectives is beneficial to improve the efficiency of the PSO algorithm. Those perspectives can be illustrated as follows:

III.5.2.A Cognitive perspectives

At t^{th} iteration, the m^{th} particle compares its fitness (figure of merit) ($\mathcal{F}[X_m(t)]$) with the one ($\mathcal{F}[X_m^b(t-1)]$) corresponding to the previous personal best position. If $\{\mathcal{F}[X_m(t)] < \mathcal{F}[X_m^b(t-1)]\}$ then the algorithm sets $X_m^b(t) = X_m(t)$. In this way, the velocity update kept a record of the best positions achieved by an individual particle.

III.5.2.B Social perspectives

At t^{th} iteration, the m^{th} particle compares its fitness ($\mathcal{F}[X_m(t)]$) with the one ($\mathcal{F}[G(t)]$) corresponding to t^{th} global best position. If $\mathcal{F}[X_m(t)] > \mathcal{F}[G(t)]$ then the algorithm sets $G(t) = X_m(t)$. Which allow the particle to share its information with the rest of the swarm by updating the global best position.

In the classical PSO algorithm, the velocity component is updated so that the contribution due to the cognitive and social perspectives are directly proportional to the difference between the current position of the particle $x_m(t)$ and the previously recorded personal $x_m^b(t)$ and global best $g_n(t)$,

respectively. In other words, the velocity vector of each particle can be decomposed to three vectors: the first one representing the current motion, the second one pointing towards the particle's best position (this being steered by the individual knowledge accumulated during the evolution of the swarm), and the last one pointing towards the global best position (modelling the contribution of the social knowledge). In this case, the m^{th} particle updates its velocity and position according to the equations

$$\mathcal{V}_{nm}(t+1) = \underbrace{w\mathcal{V}_{nm}(t)}_{current\ motion} + \underbrace{c_1 r_1\left[x^{\,b}_{nm}(t) - x_{\,nm}(t)\right]}_{individual\ knowledge} + \underbrace{c_2 r_2\left[g_{\,n}(t) - x_{\,nm}(t)\right]}_{social\ knowledge} \quad \text{(III.64)}$$

$$x_{nm}(t+1) = x_{nm}(t) + \mathcal{V}_{nm}(t+1) \quad \text{(III.65)}$$

where $w \in [0,1]$ is the inertia weight (it could be a constant as well as a variable value depending on the problem), c_1 and c_2 are the cognitive and social parameters, respectively, r_1 and r_2 are two random numbers uniformly distributed in the range [0,1]. The objective function evaluated at the new positions is compared with a user defined error criterion (a tolerance in the final solution accuracy that the user set in the algorithm). If this criterion is not satisfied, the algorithm generates new random numerical values of the numbers r_1 and r_2 in the next update. The process is iterated until the error criterion is reached. The personal best position of each particle is updated using the equation

$$x^{\,b}_{nm}(t+1) = \begin{cases} x^{\,b}_{nm}(t) & if \quad \mathcal{F}[x_{nm}(t+1)] \geq \mathcal{F}[x^{b}_{nm}(t)] \\ x_{\,nm}(t+1) & if \quad \mathcal{F}[x_{nm}(t+1)] \leq \mathcal{F}[x^{b}_{nm}(t)] \end{cases} \quad \text{(III.66)}$$

The choice of the w, c_1 and c_2 parameters value can be critical to determinate the success or failure of the search algorithm as well as the algorithm performance.

The main failure causes are:

- the particles velocity increases rapidly and they move out of the search space;
- the particles velocity rapidly decreases and they become immobile;

- particles cannot escape from locally optimal solutions.

The stochastic exploration of the search space can be modelled by the random variables $\emptyset_1 = c_1 r_1$ and $\emptyset_2 = c_2 r_2$. The weighting constants c_1 and c_2 regulate the relative importance of the cognitive perspective versus the social one. In particular, different weighting constants are used for a finer control of the search ability, by biasing the new particle position toward its historically best position or globally best position. High values of c_1 and c_2 result in new positions that are relatively far away from the previous ones in the search space, this leading to a finer?! global exploration but can also induce a divergence of the particle motion. Small values of c_1 and c_2 are useful to achieve a more refined local search around the best positions due to the limited movement of the particles but increases the time of computation. Two different conditions can be observed:

- The condition $c_1 > c_2$ endorses the search behaviour towards the particle best experience.
- The condition $c_1 < c_2$ endorses the search behaviour towards the global best experience.

The algorithm convergence is controlled by the inertial weight w. Large values of w improve exploration efficiency, while small values of w result in a confinement in an area surrounding the global maximum. The convergence speed is an important aspect to take into account since the numerical evaluation of the fitness function generally takes a considerable amount of time. Convergence speed strongly depends on the swarm size, the initial population and the boundary conditions. In particular, the parameters of the algorithm can be adapted to the specific type of problem in order to achieve a better search efficiency. However, the algorithm parameters need to be selected in order to control the convergence of the particles.

These key aspects were well studied in the literature [82-85]. When the global best position turns to be a local optimum, the PSO search performance could be degraded and a premature convergence to this local optimum can occur. Indeed, the particles located close to the local optimum solution became inactive and their velocities could become very low (close to zero). As result, the PSO algorithm would be trapped in an undesired state of slow evolution. Such limitation becomes more restrictive when PSO is applied to more complex optimization problems characterized by large search spaces and multiple local optima.

In order to avoid this phenomenon (called swarm explosion) and facilitate the convergence at the same time, specific solutions were implemented [86-88] with the aims to develop a PSO algorithm characterized by an optimal balance between global and local searching abilities. If the velocity field is not controlled, some particle can leave the physically meaningful solution space. Such process could lead to swarm divergence., This aspect increases with the problem complexity. To prevent such drawback, the definition of upper and lower limits on the velocity could be an efficiency solution

$$v_{nm}(t+1) = \begin{cases} v_{max} & if \quad v_{nm}(t+1) > v_{max} \\ -v_{max} & if \quad v_{nm}(t+1) < -v_{max} \end{cases} \qquad \text{(III.67)}$$

The value of the v_{max} parameter is selected empirically and it can significantly affect the algorithm behavior. A large value of v_{max} may cause the overlooking of a good solutions, whereas small values would reduce the motion of the particles inducing a poor exploration of some portions of the search domain. In other words, proper settings of the algorithm enhance the global exploration ability, while avoiding the trapping in local optima. Generally, the threshold velocity depends on the problem complexity [84]. Different modifications of the PSO learning have been proposed [89-91]. In particular, a variant of the learning equation has been introduced in [91]. In this scheme, the velocity is updated using the equation

$$\mathcal{V}_{nm}(t+1) = \chi\{\mathcal{V}_{nm}(t) + \vartheta_1 r_1[\mathcal{V}^b_{nm}(t) - \mathcal{V}_{nm}(t)] + \vartheta_2 r_2[g_n(t) - \mathcal{V}_{nm}(t)]\} \qquad \text{(III.68)}$$

where

$$\chi = \frac{2}{|2-\vartheta-\sqrt{\vartheta^2-4\vartheta}|} \quad \text{with} \quad \vartheta = \vartheta_1 + \vartheta_1 \text{ and } \vartheta > 4 \qquad \text{(III.69)}$$

χ is the constriction factor. The use of this update procedure enhances the convergence properties of the algorithm. A very simple identification of the optimal value of the algorithm parameters is achieved. In fact, the inertial weight and the cognitive constants are defined when only one value is set. This aspect makes the method very easy to implement while keeping its high efficiency, which perfectly corresponds with our applications in term of the REDFAs parameters optimization.

III.6 SIMULATION CHAIN

The previously described simulation model can be used in two different ways depending on the user needs; to solve the optimal design or characterization problem:

A) The Optimal design consists of the optimization of the amplifier parameters (that vary in a range defined by the user) in order to improve the amplifier performances (in particular, the gain and its noise figure). This procedure allows to found the best amplifier configuration by adapting its architecture parameters as the fiber length, the ions concentrations, the signal and pump powers, the pumping configuration…

B) The characterization problem consists in the optimization of the input parameters (such as the spectroscopic parameters of ions) in order to found their values that fit at best the experimental data (gain and noise figure). This procedure allows to recover the values of several parameters as the upconversion and energy transfer coefficients and upper energy levels lifetimes, which are generally difficult to evaluate experimentally.

Figures III.10 A and B report the flow charts summarizing the algorithm to solve both the optimal design and characterization problem, respectively.

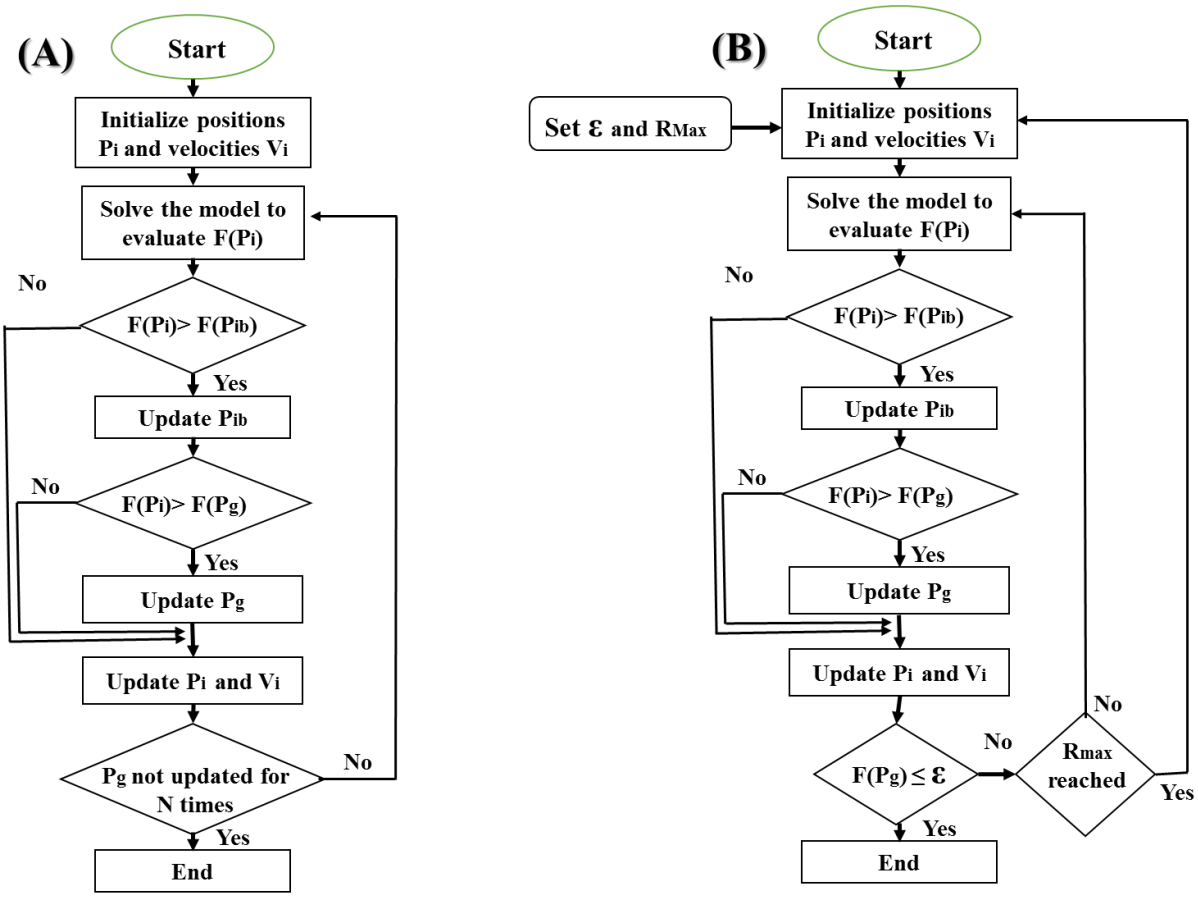

Figure III.10. Flow chart of the algorithm for solving: A) the optimal design problem and B) the characterization problem

In this third Chapter, we detailed the physical models included in our simulation tool. The overlap factors between the pump and the fiber core, the method to estimate the emission cross section of the RE ions are reported in *section III.2.* These results are used as input parameters in the modeling of REDFAs. In *sections III.3, III.4* and *III.5*, we present the different blocks of the code and their respective solvers:

-The rate equation of Er/Yb and Er doped amplifiers and the Newton-Raphson method.

-The propagation equations of signal and pump powers and the Range-Kutta method.

-The optimization procedure and the particle swarm optimization algorithm (PSO).

Finally, we describe the whole simulation chain that can be used in two ways: for design studies or characterization studies.

EN

Dans ce chapitre, nous détaillons les modèles physiques inclus dans notre outil de simulation. Les méthodes d'estimation des facteurs de recouvrement et des sections efficaces d'émission sont discutées dans la *section III.2*. Ces résultats sont utilisés comme données d'entrée pour la modélisation du REDFA. Dans les *sections III.3, III.4* et *III.5,* sont présentées les différentes parties du code et les techniques de résolution associées :

-Les équations de population des amplificateurs Er/Yb et Er et la méthode Newton-Raphson.

-Les équations de propagation des puissances du signal et de la pompe ainsi que la méthode Range-Kutta.

-La procédure d'optimisation et l'algorithme de l'approche par essaim de particules (PSO).

Finalement, l'architecture globale du code est explicitée ainsi que son utilisation soit pour des études de conception, soit pour des études de caractérisation.

FR

In questo terzo capitolo abbiamo dettagliato i modelli fisici inclusi nella nostra simulazione. I metodi utlizzati per stimare i fattori di sovrapposizione tra la pompa e il core della fibra e le sezioni efficaci di emissione degli ioni RE sono riportati nella sezione III.2. Questi risultati sono stati utilizzati come parametri d'ingresso nella modellizzazione degli REDFA. Nelle sezioni III.3, III.4 e III.5, i diversi blocchi del codice e le tecniche di risoluzione sono presentati:

-L'equazione di tasso degli amplificatori Er / Yb e Er e il metodo Newton-Raphson.

-Le equazioni di propagazione della potenza del segnale e della pompa e il metodo Range-Kutta.

-La procedura di ottimizzazione e l'algoritmo di ottimizzazione noto come PSO.

Infine, l'architettura globale del codice è spiegata, inisieme alla sua utilizzazione; infatti, esso può essere utilizzato per studi di progettazione o di caratterizzazione.

IT

Chapter IV.
Experimental Procedure

IV.1 INTRODUCTION

This chapter first describes the selected active fibers for our investigation in terms of composition, geometry and optical properties. For some of the reported tests, one of these fibers has been pre-loaded with hydrogen gas before irradiation exposure. The hydrogenation procedure is detailed, involving the hydrogen loading inside the active fiber and its outgassing monitoring after the end of the process. Second, we present our experimental procedures to irradiate the RE-doped fibers and REDFAs. Main goal was to characterize the REDFA gain evolution during and after an X-ray exposure as those experimental results are the ones that are used for comparison with the REDFA simulation results in order to validate the developed simulation tools. Third, as our simulation tools are not *ab initio,* they necessitate several input parameters that, for some of them, can be experimentally determined by our group. The various setups used to obtain them, such as RIA measurements on the active fibers and RE ion lifetimes measurements are presented. Other parameters, non-easily accessible with our facilities, have been recovered by the Particle Swarm Optimization (PSO) (see Section III.4)

IV.2 STUDIED SAMPLES

IV.2.1 Tested Optical Fibers

All the samples studied in this PhD thesis have been manufactured by iXBlue SAS [92]. The first sample Ech1 is a single mode optical fiber with an Er/Ce codoped Aluminosilicate core developed for space applications. It is a radiation tolerant optical fiber [35]. The second sample, Ech2 has the same composition than Ech1 except that no Cerium was incorporated in its core. As a consequence, this sample is more sensitive to radiations, even if it can be considered as more radiation tolerant than the active fibers from literature [37]. Ech3 sample is a double clad Er/Yb co-doped phosphosilicate fiber. Ech2 and Ech3 fibers are prototype versions of conventional active fibers and are used in this work to highlight the radiation effects on Er and Er/Yb doped fibers and to authorize a better comparison between experimental and theoretical responses of the REDFAs. Main information about these samples are reported in Table IV.1:

Table IV.1: Main characteristics of tested optical fibers

Sample	**Core dopant**	**[Yb] (wt. %)**	**[Er] (wt. %)**	**[Ce] (wt. %)**	**Geometry (μm)**	**Losses 1.55/0.98 μm**
Ech1	Al	none	0.05	yes	SC 2.7/125	8.59/11.7 dB/m
Ech2	Al	none	0.05	none	SC 2.7/125	10.3/16 dB/m
Ech3	P	1.4	0.07	none	DC 6/135	17.8/1.3(MM) dB/m

As explained in Chap. I, hydrogen presence in the fiber core improves the radiation hardness of the RE-doped optical fibers [24, 93, 94]. As a consequence, for some of the experiments, samples of Ech1 fiber have been loaded with hydrogen. After this treatment, they are labeled as Ech1H_2. It is important to notice that for this sample, designed for lab-tests, no further solution was implemented, such as the Hole Assisted Carbon Coating (HACC) structure [36] to ensure the hydrogen presence for years within the fiber. This is not an issue in the context of our work as radiation tests are done in a few hours, but for practical use of these H_2-loaded fibers in space, the use of such a solution will be mandatory.

IV.2.2 Hydrogen-loading procedure

In order to load the fiber with hydrogen, samples are kept in an H_2 atmosphere (~ 150 bar) at room temperature (RT) for about 10 days. Kinetics of hydrogen diffusion in silica are well-known, as this procedure is widely used to enhance the photosensitivity of germanosilicate fibers before ultraviolet inscription of Fiber Bragg Gratings [95,96]. The selected treatment is sufficient to ensure that the fiber core becomes saturated with hydrogen molecules before the end of the treatment [97].

As soon as the saturation level is reached, we removed the loaded fiber from the gas tank and we build an EDFA using 8 meters of the hydrogenated Ech1H_2 sample. The chosen architecture was the following: input backward pump power of 90 mW at 980 nm and input signal power of 15 μW at 1550 nm. As expected from [98], we observed a lower gain compared to the one of an EDFA made using the same length of the unloaded Ech1 sample: ~16 dB instead of ~26 dB. This gain

reduction is due to the hydrogen presence in the core and the associated increase of the fiber attenuation at the pump and signal wavelengths. We then follow the time evolution of the gain as the hydrogen outgasses at RT (about 20°C). Figure IV.1 illustrates the increase of the measured EDFA gain since the EDFA building (with the fiber saturated with H_2) and then during the hydrogen outgassing from the fiber core. It is worth noticing that the gain increases from 16 dB starting 20 hours after the end of the hydrogen loading, to ~ 23 dB after 120 hours of desorption at RT. The observed growth kinetic of the EDFA gain can be well fitted using a simple exponential law with the parameters listed in Table IV.2.

Table IV.2: Fitting function and its parameters

Fitting equation	$G = A\,e^{-t/t_0} + G_0$	
Parameter	**Value**	**standard error**
G_0	25.63	0.05
A	-12.72	0.03
t_0	65.83	0.76

As expected, this gain evolution agrees with the amount of H_2 in the fiber core. Hydrogen strongly attenuates the signal and the pump power [99]. Indeed, it was reported in [87] that the desorption kinetic $C(r,t)$ of hydrogen in an optical fiber having a radius of r_0 is described by the equation IV.1.

$$C(r,t) = C_0 \sum_{n=1}^{\infty} \frac{2J_0\left(\alpha_n \frac{r}{r_0}\right)}{\alpha_n J_1(\alpha_n)} Exp\left[-D\left(\frac{\alpha_n}{r_0}\right)^2 t\right] \qquad \text{IV.1}$$

Where D is the diffusion coefficient, J_1 the Bessel function of first order, α_n the n^{th} order of the Bessel function J_0 and C_0 the initial hydrogen concentration.

From a practical point of view, a compromise has to be found for the fiber hydrogen treatment between its negative impact on the gain and its positive enhancement of the fiber radiation resistance. For the experiments reported in Section V.4, we defined as an acceptable compromise the H_2 concentration reached ~120 h after the end of the loading. At this time, the EDFA gain is of ~23 dB using Ech1H_2 sample instead of ~26 dB for the EDFA based on the Ech1 sample. As it will

be demonstrated later, those conditions allow to design an EDFA with good optical performance and enhanced radiation hardness.

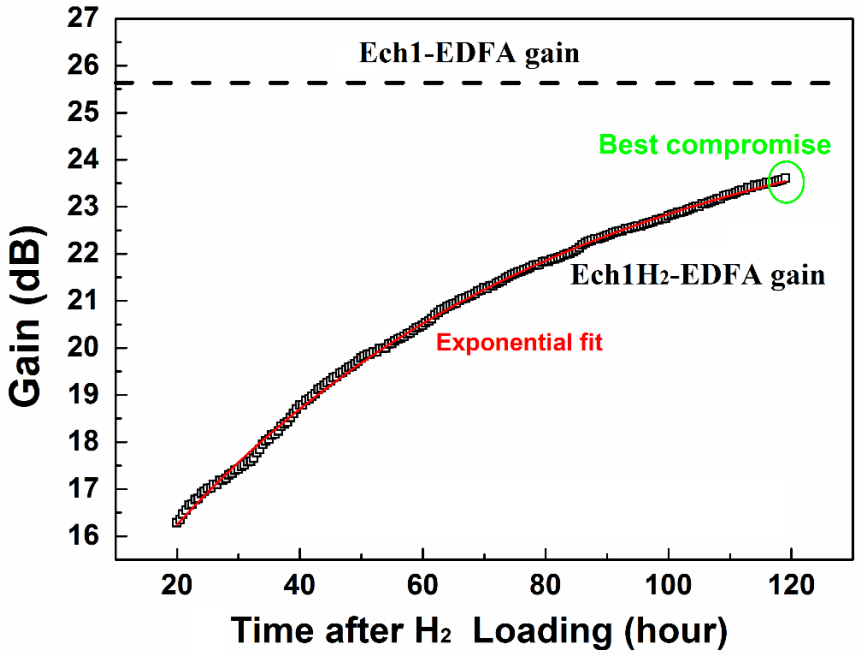

Figure IV. 1. EDFA-Ech1H$_2$ gain evolution with H$_2$ outgassing time at room temperature. In red is illustrated the best fit of the observed kinetic with a single exponential.

IV.2.3 Double clad geometry

For the design of high power EYDFA (dozens of Watts of input power at 940 nm), the use of a double clad geometry appears mandatory to prevent both the fiber core overheating and the non-linear effects. Indeed, for a 10 W input pump power injected into a single mode doped fiber having a 3 µm core diameter, the energy density becomes about 10^{13} W/m^2 ($D = P_P/A$ where P_p is the pump power in W and A is the doped core area. To reduce this energy density, the pump power can be injected in a multimode configuration exploiting the specific properties of the double clad fiber (figure IV.2).

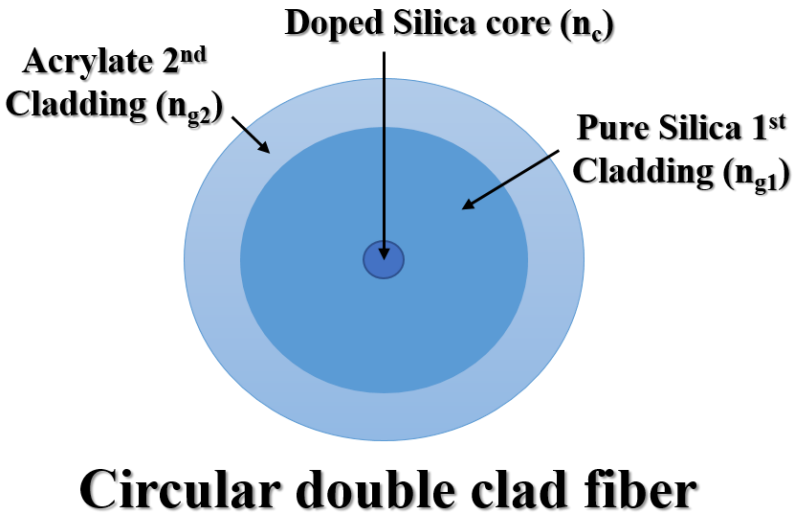

Figure IV.2. Circular double clad fiber geometry with ($n_c > n_{g1} > n_{g2}$)

In general, the Er-Yb-doped fiber geometry and refractive index are chosen to ensure that the fiber is single mode at the signal wavelength (~ 1550 nm) and multi-mode at the pump wavelength (~ 940 nm). Being multimode allows a better distribution of the pump power along the fiber longitudinal axis and therefore a more homogenous population inversion in the core. However, as the light amplification is ensured only by the RE fiber doped core (no ions in the first cladding), the pump travelling in the cladding has no interaction with the RE ions located in the fiber core. This is illustrated in Fig.IV.3 that gives the guided mode at 940nm calculated using COMSOL Multiphysics. This mode is not crossing the core and then is almost not absorbed by the ions affecting the pumping efficiency.

As shown in figure IV.3.A, the absorption of the pump power reaches a saturation level at ~10 dB/m even if the fiber length is increased. The propagated modes such as the one illustrated in Figures IV.3.B, C and D are explained by the fiber double clad geometry which induces a propagation in the first cladding. In order to avoid such phenomenon more complex geometry have to be used that can force the energy to visit the core region.

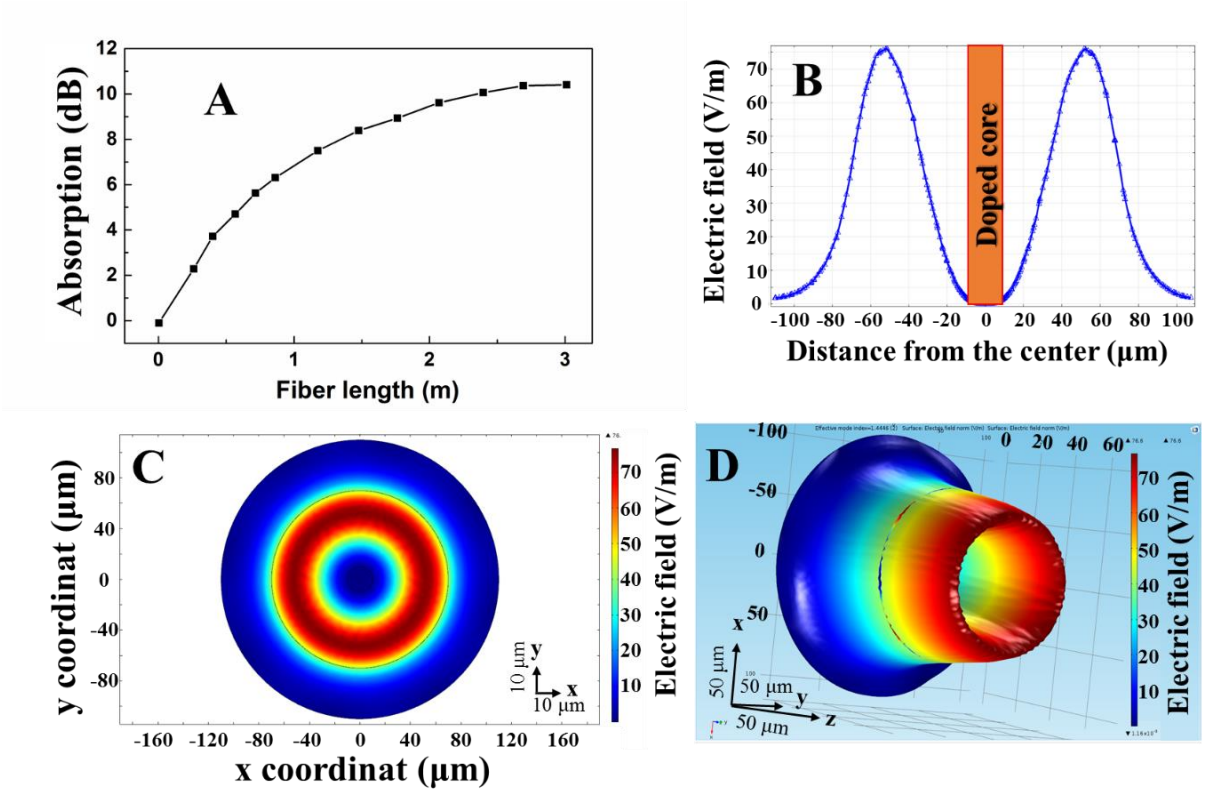

Figure IV.3. Circular DC fibers: A. absorption of a DC fiber as a function of its length from [100]. B, C, D represent 1,2 and 3D plots of a simulated normalized electric field illustrating a pump propagating mode that weakly interacts with the doped core area.

Figures 4. A, B, C and D represent some of the solutions that allow to mix the different modes by breaking the propagation symmetry in the inner cladding and then increase the overlapping of the pump light with the RE ions.

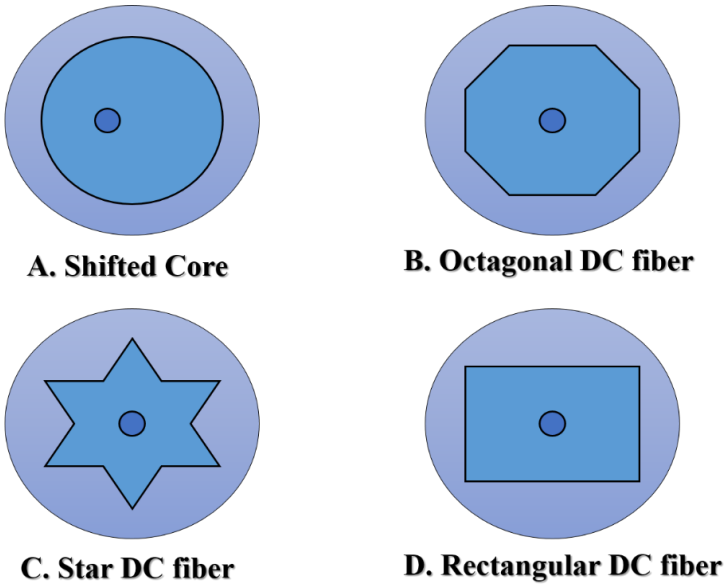

Figure IV.4. Different fiber geometries improving the pump draining along the active fiber length

The octagonal geometry (B) solution was chosen by iXBlue for the tested ErYb-doped DC optical fiber. In fact, this geometry remains close to the circular one allowing a better splice to the passive optical fibers used in the EYDFA assembly. Figure IV.5. gives an Energy Dispersive X-ray (EDX) image of this cleaved DC fiber. The phosphosilicate ErYb-codoped core has a 3.7 µm diameter, the first pure silica octagonal cladding is 125 µm diameter and the second acrylate cladding is about 160 µm (removed from the fiber for the cleave). The use of acrylate with a lower refractive index (~ 1.35) allows to increase the fiber numerical aperture resulting in a better coupling between this fiber and the multimode fibered pump laser diode.

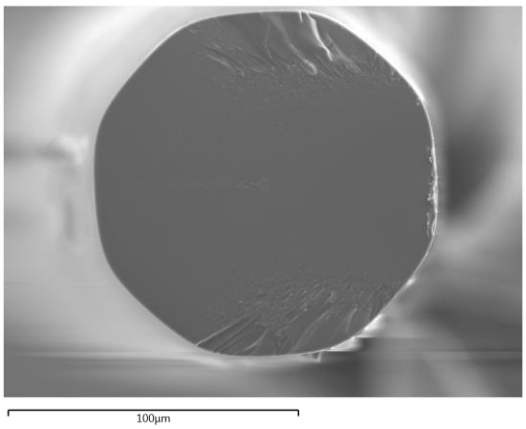

Figure IV.5. Energy dispersive X-ray image of ECH3 fiber produced by iXBlue highlighting the 1st octagonal silica cladding used to maximize the pumping of Yb ions

IV.3 AMPLIFIER CHARACTERIZATION UNDER IRRADIATION

IV.3.1 Irradiation test facility

X-ray irradiations were performed in order to investigate the active fibers and REDFA response when they are exposed to radiations. These *in situ* measurements allow to characterize both transient and permanent radiation effects on the device responses. X-rays are not directly representative of the space environment where in general, electrons, protons and heavy ions particles are the main radiation sources, but their effects on amorphous silica are indeed well representative of such particles. It was shown that both X-rays and protons lead to comparable ionization processes responsible for the defects generation [101, 102] (see section I.6). In other words, the amplifier performances are mainly affected by the amount of defects generated in the doped fiber due to the exposure (independently of the types of irradiation) [103].

X-ray irradiation have been performed at Hubert Curien laboratory (France) using the X-ray machine MOPERIX delivering photons of about 40 keV energy. Selected irradiation dose rates are the lowest (in the range of dozens of rad (SiO_2)/s) accessible with this machine and have been chosen to be the most representative of those encountered in space, even if the space ones are generally 10^4 lower than the ones used for our tests. This configuration (accelerated *tests*) appears mandatory to reduce the test duration with respect to the long duration of the space missions to achieve the expected investigations. For the tested fibers, as for nearly all fiber types, working at higher dose rate leads to an overestimation of the RIA as it favors the defect generation against the bleaching mechanisms [104].

In this work we performed the tests at total ionizing doses (TID) up to ~ 300 krad (SiO_2). This maximal value clearly exceeds the usual TIDs associated with up to 70 krad expected for a 30 years in orbits around Earth. However, by reaching higher TIDs, we aim to also cover the needs of future space missions and of the most challenging programs such as Jovian [105].

IV.3.2 Experimental setups: in situ REDFA Gain measurement

The radiation response of each developed REDFA architecture has been evaluated under X-rays in two different regimes. The first one called configuration ON corresponds to the case for which the

active fiber is pumped at 980 nm during the whole irradiation run. These test conditions are representative of an amplifier operated during the whole space mission. The second configuration OFF corresponds to the case where the fiber is not pumped during the irradiation. This test condition is representative of an amplifier used as a backup solution during a space mission, unbiased up to its potential reactivation in the case the main REDFA fails.

The input, output signals and input pump powers of the REDFA are monitored online under X-rays using an Agilent 81638 Lightwave Multimeter (PWM). The pumping laser diodes emitting either at ~ 980 nm for EDFAs or at ~ 915 nm for EYDFAs are controlled with a Thorlabs Pro8000 LD module. In order to evaluate the REDFA optical gain, the output and input signal spectra are continuously measured using a YOKOGAWA Optical Spectrum Analyzer (OSA) during the whole irradiation run. From these measurements, the REDFA gain is then calculated from the output and input power values at the same wavelength of 1550 nm. Moreover, the observed ASE contribution is removed to allow a direct comparison between the measured gain results and those obtained through our simulation codes that evaluate separately the REDFA signal and the noise powers.

Figure IV.6 represents the developed setup to investigate the amplifier performances *in situ* under X-rays for both EDFA (A) and EYDFA (B). The passive single clad fibers (SCF) used in this experiment are radiation tolerant and the effects of X-rays on them can be neglected compared to their impact on the RE-doped fibers.

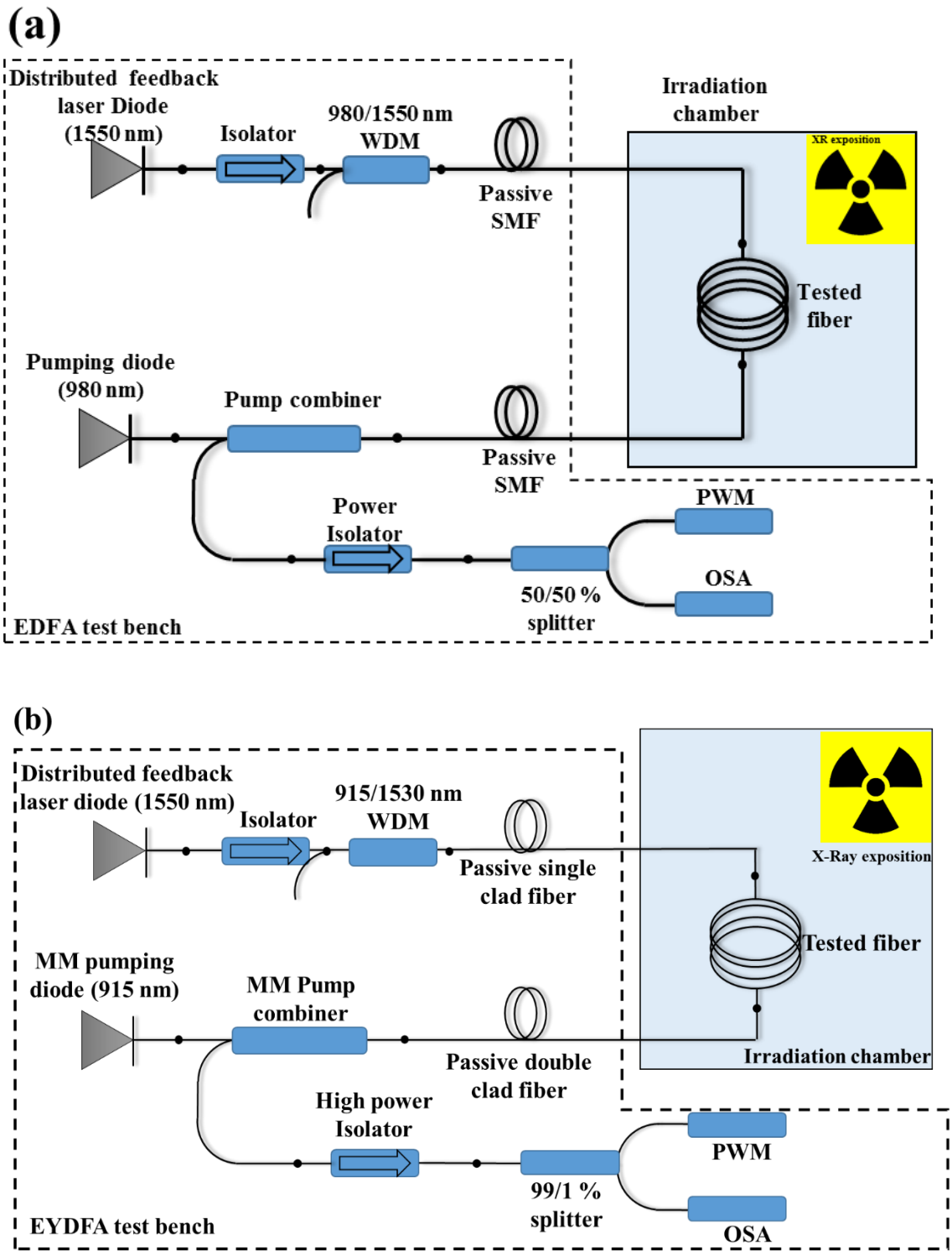

Figure. IV.6. Experimental setups used for the *in situ* amplifier characterization under X-rays; A) EDFA, B) EYDFA.

These experiments render possible the monitoring of the amplifier performances in terms of gain, noise figure before, during and after the end of the X-ray irradiation. Figure IV.7 illustrates the input and output spectra measured with the OSA of an EDFA made with 8 m length of the Ech1 fiber. The EDFA test conditions were 90 mW of pump power at 980 nm in a contra-propagative scheme and a 15 µW of input power at 1550 nm.

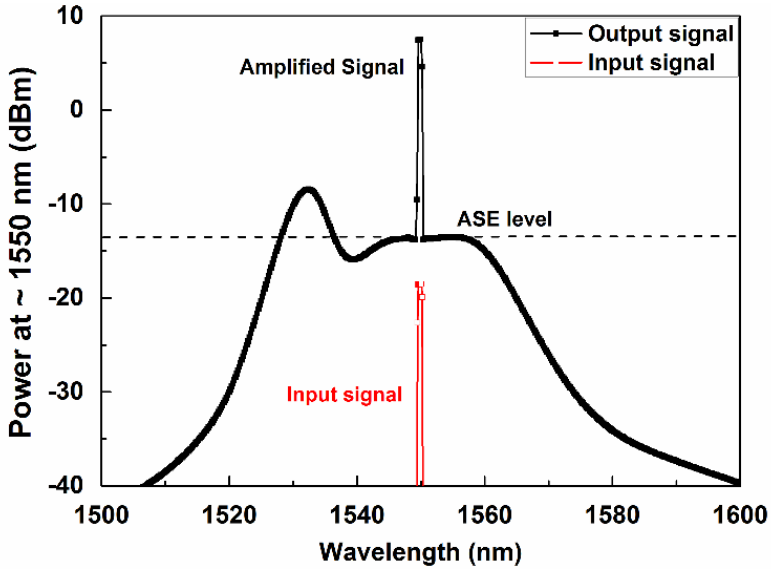

Figure IV.7. Input and output signals spectra of an EDFA made with 8 m length of the ECH1 fiber using 90 mW of pump power at 980 nm and 15 µW of input power at 1550 nm

IV.4 IN SITU RIA MEASUREMENT

The RIA values at the pump and signal wavelengths are the main parameters to be injected in the simulation codes to model the REDFA radiation responses. In other words, the accuracy of the simulations of amplifier degradation is directly related to the representability of the RIA measurements. Preliminary investigations [106] have shown that for EYDFA, the RIA measured on the Er.Yb-doped fibers using a white light source and a spectrophotometer permits to correctly explain the EYDFA behavior under radiation. As the injected light power levels strongly differ between the white light source and the pump power during the EYDFA operation this demonstrates that the photobleaching effect due to the 915nm pump can be neglected for this type of fiber. However, in the case of EDFAs, the work described in this PhD will demonstrate that it is

mandatory to measure the RIA at the two wavelengths in conditions representative of an operating EDFA as the RIA levels in aluminosilicate optical fibers are sensitive to photobleaching. In *section VI.2* the photobleaching effect will be more deeply studied for this class of fibers.

In order to achieve the RIA measurement in the most reproductive way of the operating EDFA conditions, we designed a setup allowing to perform this measurement in two different configurations; P_{MAX} and P_{MIN}.

- **P_{MAX} mode** means that the fiber is pumped 80 % of the time at 980 nm during the irradiation run (with the same pump power used for the EDFA). The RIA measured in this P_{MAX} configuration is as close as possible to the RIA that the fiber undergoes when the EDFA is 100% of the time in the ON mode during its irradiation. This mode partially takes into account the photo-bleaching influence even if its total effect may not be reached [107]. To achieve these RIA measurements, we changed between the pump and the white light source using a Thorlabs switch as illustrated in Figure IV 8. Doing so, we measure the RIA spectra every 10 minutes. The erbium-doped fiber is pumped during 8 minutes and then we switched to the white light source for the 2 next minutes, time needed for the RIA spectra acquisition.
- **P_{MIN} mode** corresponds to the case without 980 nm pumping of the active fiber during the irradiation (classical RIA setup), the RIA levels being continuously monitored with a white light source of very low power as usually done for RIA measurements of passive optical fibers. Measured RIA is then representative of the one encountered by an EDFA operating in the OFF mode, almost no photobleaching takes place.

Figure IV.8.B compares the RIA dose dependences measured in both P_{MAX} and P_{MIN} configurations for Ech1 sample. These results demonstrate the impact of the 980 nm pump power (90 mW) on the RIA levels and kinetics at both pump and signal wavelengths. It proves that photobleaching anneals part of the defects absorbing in these spectral ranges. The degradation in the P_{MIN} configuration exceeds the one in the P_{MAX} configuration for both the signal ($\alpha_{\boldsymbol{sPMAX}}$ = 0.8 dB/m, $\alpha_{\boldsymbol{sPMIN}}$= 3.5 dB/m at ~300 krad) and the pump ($\alpha_{\boldsymbol{PPMAX}}$= 5.6 dB/m, $\alpha_{\boldsymbol{PPMIN}}$= 9.9 dB/m at ~300 krad) wavelengths.

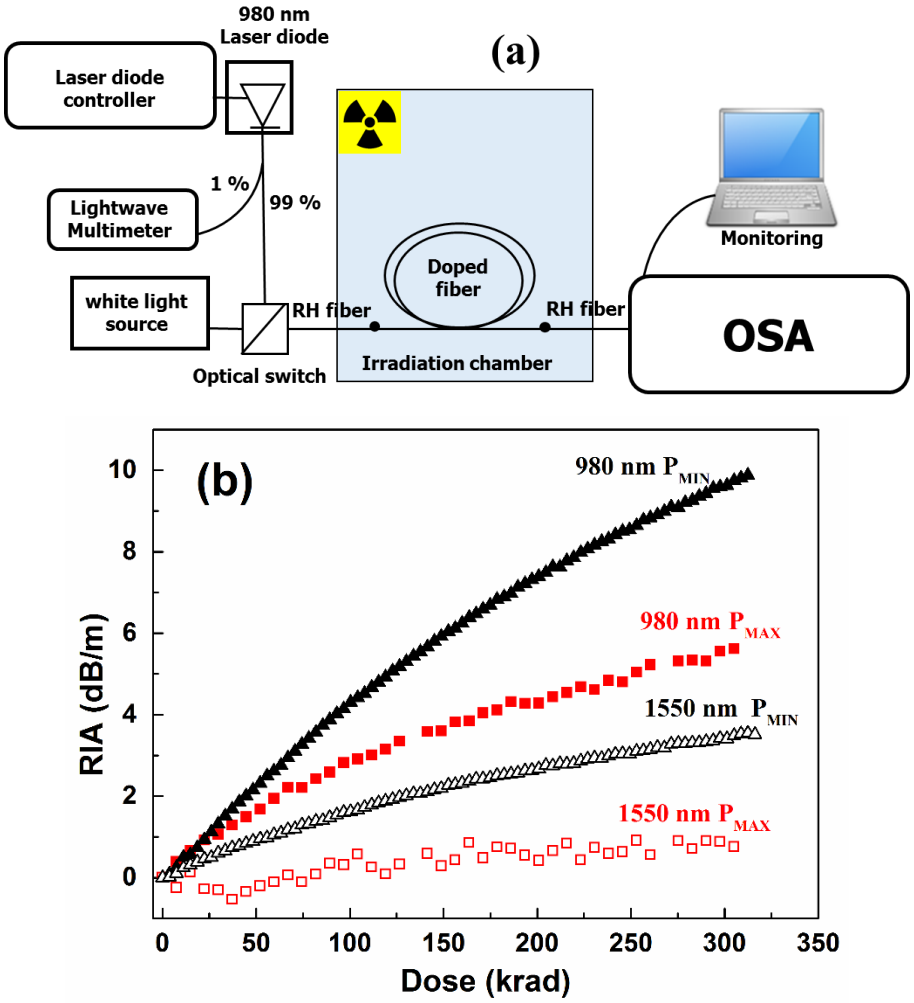

Figure 8. (a) RIA measurement setup in P_{MAX} configuration, (b) Dose dependence (dose rate of ~ 12.5 rad/s and at RT) of the RIA at 980nm and 1550nm in the ECH1 sample (about 1 m length) measured in both the P_{MAX} and P_{MIN} configurations with a.

IV.5 TIME-RESOLVED LUMINESCENCE

Time-Resolved Luminescence (TRL) technique is an effective way to determinate the electron states lifetimes and its kinetics, which allow to determine the processes involved in the relaxation of those excited optical centers.

IV.5.1 TRL theoretical backgrounds

When a luminescent material is excited and the excitation energy is absorbed, it can emit a photon. This is called luminescence. In general, the luminescence mechanisms can be classified into two categories [108]:

- The first one is the intra-centric luminescence occurring when the excitation process is localized on an isolated center without the ionization of any species in the material. In other words, the excitation and emission phenomena occurs due to electronic transitions at the optical center. However, in some cases the process can be more complicated, when the activator (studied element) does not absorb the excitation radiation directly but receives the energy from another center called 'sensitizer', which absorb the radiation and transfer the energy to the activator (Acceptor) (see section II.2.6).
- In the case of the second mechanism, the excitation is generated by radiations or particles with much higher energy than the band gap inducing an ionization. The luminescence is produced by the recombination of an electron or a hole at the ionized centers.

In the time-resolved luminescence procedure, a pulsed laser with short period (pico- to nano-second) is used as excitation. This kind of excitation allows the study of the luminescence decay as a function of the time following the pulse. The excited center will relax with the kinetic described by equation IV .2 which gives the time dependence of the excited state population.

$$\frac{dN(t)}{dt} = \left[k_R + k_{NR}(T)\right] N \qquad \text{IV.2}$$

Where N is the excited state population, k_R and k_{NR} are the radiative and non-radiative decay rates, respectively, N_0 is the initial population at the time t = 0 that corresponds to the exact moment where the excitation pulse is switched off. The solution of this equation has the form IV.3.

$$N(T,t) = N_0 \exp\left(\frac{-t}{\tau}\right) \qquad \text{IV.3}$$

Where $\tau = \dfrac{1}{k_R + k_{NR}(T)}$ is the excited state lifetime and T is the temperature.

The luminescence intensity is proportional to the energy level population; allowing to express equation IV.3 in the form:

$$I(\lambda_{EM},\lambda_{EX},T,t) = k_R F(\lambda_{EM}) N_0 \exp\left(\frac{-t}{\tau}\right) \qquad \text{IV.4}$$

Where $F(\lambda_{EM})$ is a function that describes the emission band profile. The luminescence intensity (I) depends on both the emission (λ_{EM}) and excitation (λ_{EX}) wavelengths.

The non-radiative decay is very sensitive to the temperature. In fact, at low temperature the non-radiative rate (k_{NR}) can be neglected so the lifetime τ is directly linked to the radiative transition rate and in this case: $\tau \sim \frac{1}{k_R}$.

IV.5.2 TRL experimental setup

The TRL measurements were performed at Hubert Curien laboratory using an integrated system made of a tunable-laser source (the excitation system), a spectrometer coupled to an infrared CCD (the detection chain), in addition to optics used to focus the laser excitation light and collects the luminescence from the samples;

-***The excitation system*** uses the third harmonic of a Nd:YAG laser (from Spectra Physics) delivering a typical energy of few mJ per pulse (depending on the working wavelength) with a repetition rate of 10 Hz and a laser pulse duration of about 5 ns. In this way, a tunable excitation wavelength ranging from 216 to 2000 nm can be generated using an optical parametric oscillator.

-***The detection chain:*** the luminescence is collected using a two-lenses-optical-systems and focalized onto spectrometers equipped with cameras allowing both UV/Visible and IR emission studies. In our case (IR study) the spectrometer uses 150, 300 or 600 grooves /mm optical gratings and a triggered ANDOR CCD camera.

The luminescence spectrum of Er^{3+} ions in the infrared range (1420-1640 nm), due to the transition $^4I_{13/2} \rightarrow {}^4I_{15/2}$, was recorded using an externally triggered ANDOR CCD camera and a 150 grooves /mm optical grating (see setup in Figure. IV.9.A). The luminescence spectrum of Yb^{3+} ions (850-1120nm), due to the transition $^2F_{5/2} \rightarrow {}^2F_{7/2}$, was analyzed using a photomultiplier coupled to an Agilent 7000B 500MHz oscilloscope.

Low temperature luminescence measurements were performed by sinking the optical fiber samples into a liquid nitrogen bath (77 K) and using two passive multi-mode optical fibers to inject the excitation laser pulse into the sample and to deliver the collected luminescence to the spectrometer. This experiment allows to measure the radiative decay lifetimes (see setup in Figure IV.9.B).

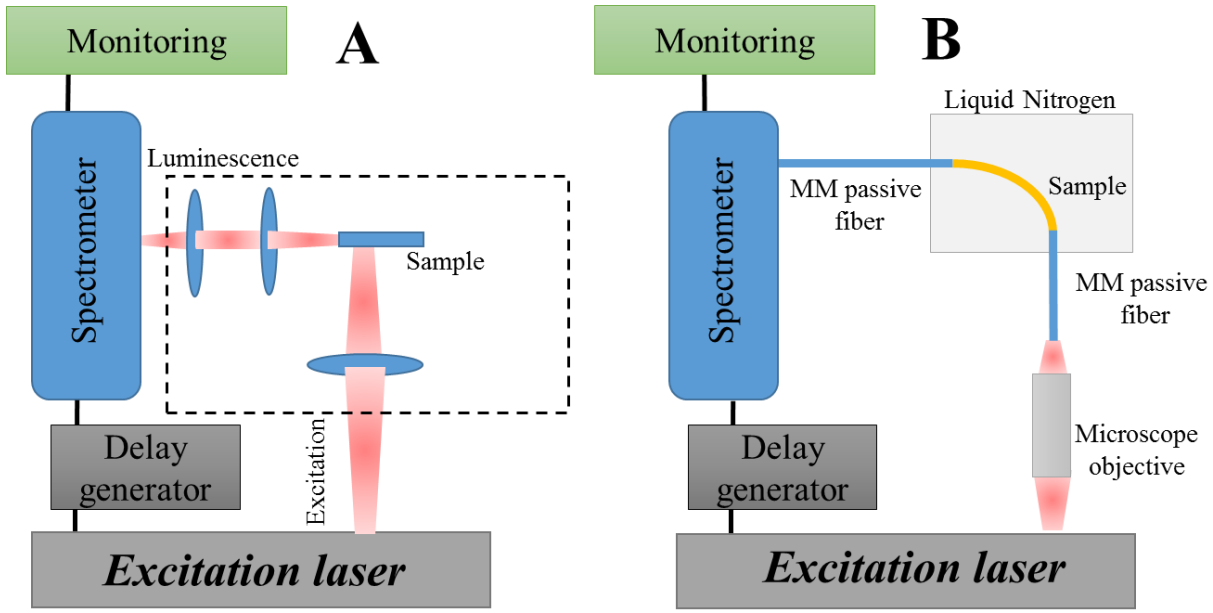

Figure IV.9 schematic setup of the TRL experiments A) Normal configuration B) Low temperature measurement configuration

In this fourth Chapter, we present the different samples selected for this PhD thesis work to build REDFAs as well as the hydrogen-loading procedure for some of them in *section IV.2*. Thereafter, the REDFA experimental characterization procedure under irradiation is introduced in *section IV.3* detailing the gain measurement method. In *section IV.4,* the radiation induced attenuation (RIA) *in situ* measurement procedures for the REDFs is explained to consider the photobleaching effect. The obtained RIA data will be used as input in the simulation to reproduce and/or predict the amplifier degradation during and after the exposure. The time resolved luminescence technique is described in *section IV.5*. This procedure was used to estimate the metastable energy levels lifetimes and their evolution during the irradiation.

EN

Dans ce quatrième Chapitre sont présentés les différents échantillons sélectionnés dans cette thèse pour construire les REDFAs ainsi que la procédure d'hydrogénation des fibres optiques (*section IV.2)*. Ensuite, la procédure de caractérisation des REDFAs sous irradiation est explicitée, en particulier la méthode de suivi de l'évolution du gain est décrite dans la *section IV.3*. Dans la *section IV.4*, la procédure de mesure de l'atténuation induite par radiation (RIA) dans les REDFs est expliquée, en particulier pour la prise en compte des effets du photoblanchiment. Les données obtenues servent de données d'entrée pour la simulation pour reproduire et/ou prédire la dégradation du REDFA pendant et après l'irradiation. La technique de luminescence résolue en temps est décrite dans la *section IV.5*. Cette procédure a été utilisée pour mesurer les durées de vie des niveaux d'énergies et leur évolution sous irradiation.

FR

Nel quarto capitolo, sono presentati i diversi campioni selezionati in questo lavoro di tesi per reallizzare l'REDFA e il processo di idrogenazione (sezione IV.2). In seguito, la procedura per caratterizzare sperimentalmente gli REDFA sotto irraggiamento, e in particolare il metodo per seguire l'evoluzione del guadagno, è riportata nella sezione IV.3. Nella sezione IV.4, il metodo per misurare in situ l'attenuazione indotta dalle radiazioni (RIA) nelle REDF è presentata, in particolare prendendo in cosiderazione l'effetto del photobleaching, ossia la ricombinazione indotta dalla luce. I valori della RIA ottenuti saranno utilizzati come input nella simulazione per riprodurre e/o prevedere il degrado dell'amplificatore durante e dopo l'irraggiamento. La tecnica di luminescenza risolta in tempo è descritta nella sezione IV.5. Questa procedura è stata utilizzata per stimare i tempi di vita dei livelli energetici e la loro evoluzione sotto irragiamento.

IT

Chapter V.
Simulation and Experiment confrontation

V.1 INTRODUCTION

The actual REDFA hardening approach is mainly based on the enhancement of the radiation resistance of each subparts of the amplifier. This approach usually gives good results improving also as a consequence the response of the whole system to radiations. This procedure is called '***The hardening by component strategy***'. However, using this technique if the system radiation tolerance is increased, it often appears that using these radiation hardened components, it becomes more complicated to achieve the same optical performances than with state-of-the-art COTS components. Furthermore, the levels of radiation hardness to be attained on the components can be reduced by acting simultaneously at the system level, designing a REDFA architecture that is by design and intrinsically more tolerant to radiations. For our particular application, we can imagine to design a REDFA that is optimized to present the best performances during the space mission rather than on Earth during labs experiments. Such an approach can be called '**H*ardening-by system-strategy***' and will be further detailed in the following sections. Our hardening approach includes:

***-A Hardening-by-component (here the active fiber) strategy*:** which consists in the exploitation of the EYDFA radiation hardening solutions described in section I.7 and well-studied in the previous PhD thesis works (Marilena Vivona, 2013 [109], Blandine Tortech, 2008 [110]) or some of our research papers [35, 36, 111].

-An Optimization of the REDFA architecture through a coupled Experiment/Simulation Approach: which consists in the building of simulation tools allowing optimization of the amplifier parameters in order to achieve the best performances in term of REDFA gain and noise figure during the mission. It should be noted that in the future these tools can be used to predict the degradation of a given amplifier during a specific mission profile, needing only a limited number of experiments at Earth's radiation test facilities.

Our procedure is summarized in the following schematic in which the parts investigated in this chapter V are highlighted in red.

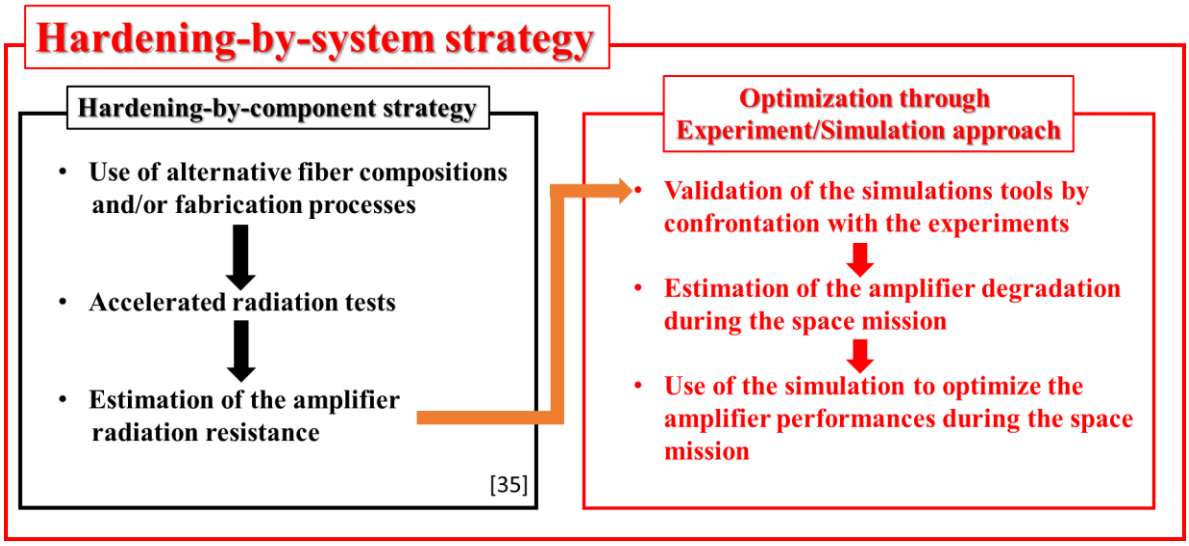

Fig. V. 1. Illustration of the hardening-by-system strategy used to mitigate the radiation effects on the EDFA Elements investigated in this chapter are highlighted in red.

The chapter is divided in four sections:

- First, we performed a parametric study on the influence of RE spectroscopic parameters on the EDFA gain and noise figure. This preliminary study appears mandatory as several of those input parameters cannot be calculated from first principles theory, are difficult to measure experimentally implying that we used data from the literature or that we recovered those parameters by simulation and confrontation to experimental data.
- Second, we validate the developed state-of-the-art simulation tools by comparing the calculated EDFAs output powers with the ones measured for the same architecture of EDFA. This comparison has been done for various pump currents and for EDFA designed using the non-irradiated Ech1 and Ech1H_2 fibers described in *Section IV.2.1*. This procedure allows us to determine the spectroscopic parameters of our fiber samples. These parameters will then be fixed for the other simulations involving radiation effects.
- Third, the RIA measurements at the pump and signal wavelengths have been injected in the validated simulation tools in order to predict the amplifier degradation for various active fibers and EDFA architecture. The obtained simulation results are then compared with the experimental data acquired during radiation tests of manufactured EDFA to validate the radiation module of our simulation chain. The reliability and robustness of the code were tested for several amplifiers with different active fiber lengths.

- Finally, we exploited the validated complete code, including radiation effects, in order to optimize the amplifier response during an irradiation by benchmarking different pumping configurations and active fiber lengths. Doing so, we have been able to find the best EDFA architecture with the the best performances during the whole space mission.

V.2 PARAMETRIC STUDY OF THE INFLUENCE OF RARE-EARTH SPECTROSCOPIC PARAMETERS ON THE EYDFA GAIN AND NOISE FIGURE

As explained in sections III.1 and 2, as our calculations are not from *ab initio*, we have to inject input parameters in our codes to describe the spectroscopic properties of RE ions incorporated in the active fiber cores. A part of them can be quite easily measured using the LabHC available facilities whereas others are more difficult to characterize using these setups. Then these last parameters have to be extracted from data reported in the literature. In this section, we demonstrate that the developed predicting tools can be improved by recovering these spectroscopic parameters through the PSO algorithm rather than using literature data. Of course, this implies to compare the simulation results to experimental data, which was possible in our case. In addition to this first goal, we can expect that the values of some of those parameters may evolve with dose (maybe at doses larger than space application related ones), as radiation modifies the surrounding electronic field of the host matrix through point defects generation. Then, we also study the impact of varying those parameters on the EYDFA gain and the noise figure. To this aim, a systematic and arbitrarily parameter variation from -20% to +20 % has been applied for various pump conditions. Our aim was to determine which parameters can significantly affect the amplifier performance if they are altered by irradiation. Outputs of this preliminary study can be used to identify the most crucial experiments to be done to measure most sensitive parameters. The performed study allows to improve the simulation efficiency and effectiveness leading ultimately to a more accurate EYDFA behavior prediction in more severe environment than space.

The RIA at the pump and signal wavelengths are today the only “radiation parameters” considered in the REDFA’s simulation at low doses. It was reported in [29] that the accuracy of the amplifier response to radiation prediction was within 10% using only the RIA at pump and signal

wavelengths as input for the amplifier degradation estimation during the exposure. Fig. V.2 summarizes this procedure highlighting the work made in this section in red.

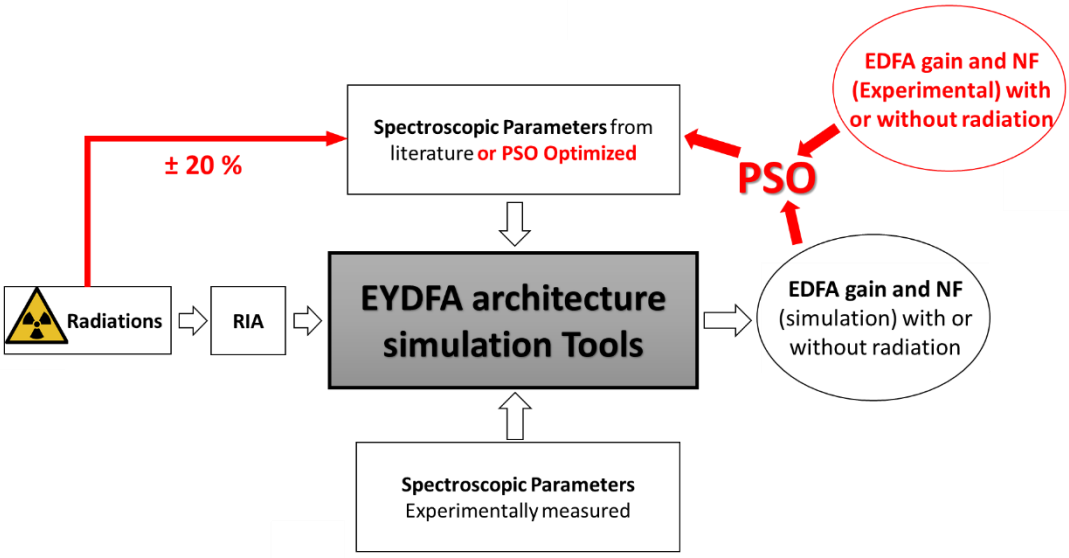

Fig. V. 2. Illustration of the simulation tools used to predict the radiation response of an EDFA. Parameters investigated in this section of chap. V are highlighted in red.

We choose to perform this study for EYDFA since the Er/Yb model is more complex than the one of Erbium: Energy transfer coefficient, Yb levels lifetimes…

V.1.1. EYDFA Experiments and simulation results.

V.1.1.A. Experiments

Gain measurements have been performed for an EYDFA designed with a backward pumping architecture. About 8 mW of input signal power at 1.55 µm is injected in one end of the 7 m long Ech3 doped fiber. This length was calculated to be optimal to achieve the highest gain in absence of radiations. From the opposite fiber output, pump light at ~915 nm from a multimode laser diode is injected through the double clad at its maximum power of 10.4 W.

An Agilent 81638 lightwave multi-meter and a Yokogawa OSA (Optical Spectrum Analyzer) measure the output power and signal spectrum, respectively. The output signal shape around 1.5 µm with 10.4 W input pump power is compared in fig. V.3. with the input signal. In our code,

we calculated the EYDFA gain by comparing the output and input signal powers at 1550 nm after the subtraction of the amplifier spontaneous emission (ASE).

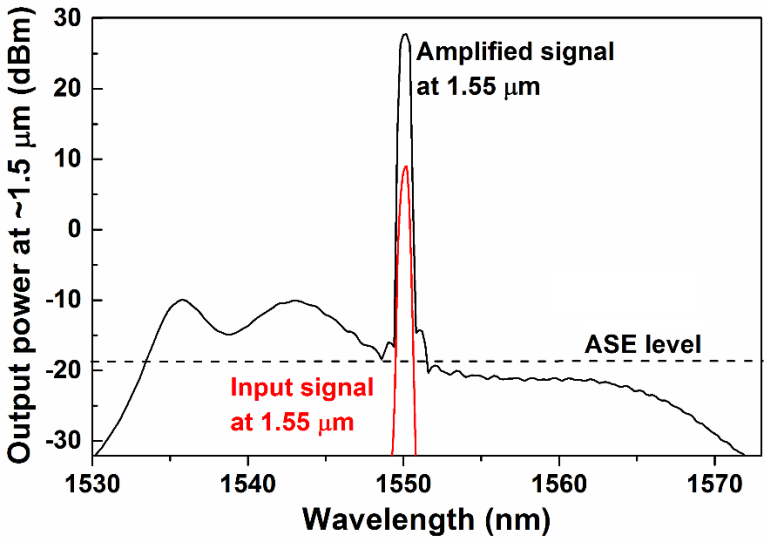

Fig. V.3 Input and Output signal power spectra of a backward EYDFA designed with 7m of ECH3 fiber: 8 mW input signal at 1550 nm and 10.4 W of 915 nm pump power.

V.1.1.B. Simulation Optimization through PSO

Using the PSO approach, the recovery of some RE ion spectroscopic parameters as energy transfer coefficients, up-conversion coefficients and lifetimes has been carried out. Indeed, some of those parameters are difficult to measure experimentally and as they depend on the fiber composition and manufacturing process, the values reported in literature may not be fully representative of our investigated fibers. By means of PSO these parameters can be numerically optimized using, as input data, the measured gains for different EYDFA operation conditions: pump power, fiber length, signal wavelength… In this case, the developed numerical code will adapt the fiber parameters, within a user defined range, to minimize the mean square error between all the experimental results and the numerical ones.

V.1.2 Results and discussion

V.1.2.A Comparison between experiments and simulation results: result improvements obtained using PSO approach

The simulations have been performed using the relevant EYDFA experimental parameters: fiber length (7 m), input signal (1550 nm), pump power (up to 10 W), pump wavelength (915 nm) and pumping configuration (backward). As input parameters to describe the Ech3 sample, we used a set of parameters measured experimentally by our consortium such as lifetimes, absorption and emission cross sections as well as parameters extracted from literature or recovered through the PSO. The resulting dependences of the output power at λ_s=1.55 μm versus the pump power are compared in Figure V.4. for both cases to the data measured on the manufactured EYDFA. The spectroscopic parameters that were experimentally determined through state-of-the-art measurement techniques are listed in *Table V.2.* whereas *Table V.3* lists the values for remaining parameters. For those, we first used literature data [112], and in a second time we recovered them using the PSO algorithm to achieve the best fit on our experimental data.

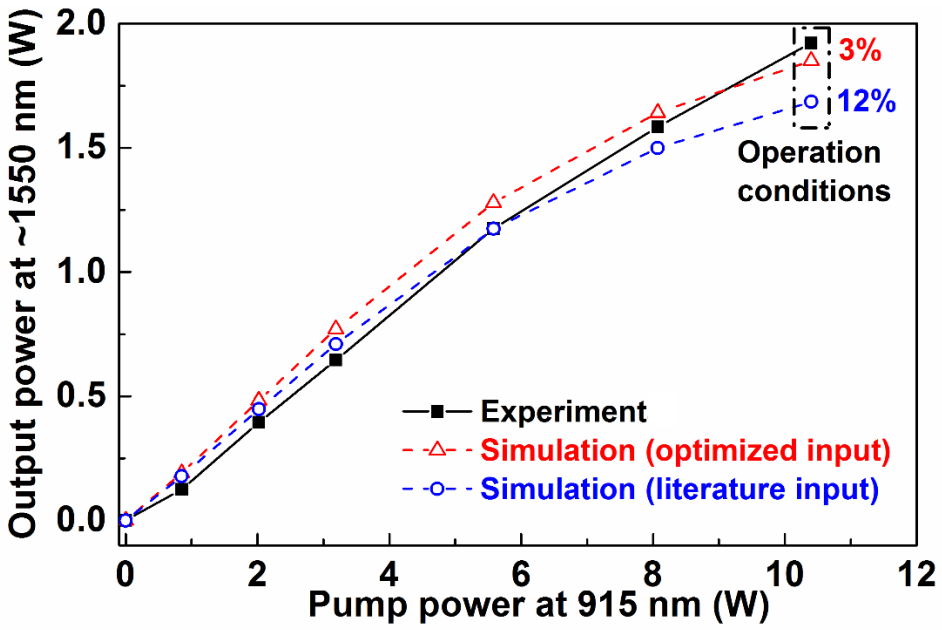

Fig. V.4. Measured and calculated output powers at λ_s=1.55μnm as a function of the input pump power using literature spectroscopic parameters and PSO-recovered parameters

Table V.2. Measured spectroscopic parameters

Parameter	value
$^4I_{13/2}$ Lifetime τ_{21}	8.9 ms
$^2F_{5/2}$ Lifetime τ_{65}	1.2 ms
σ_{65} Yb^{3+} emission cross section	2.1×10^{-26} m^2
σ_{56} Yb^{3+} absorption cross section	7.4×10^{-25} m^2
σ_{21} Er^{3+} @1.55 µm	1.24×10^{-24} m^2
σ_{12} Er^{3+} @1.55 µm	1.14×10^{-24} m^2

*Table V.*3 Literature and PSO-recovered parameters

Parameter	Literature value	optimized value
$^4I_{11/2}$ Lifetime τ_{31}	6.7 µs	10 µs
$^4I_{9/2}$ Lifetime τ_{41}	0.35 µs	0.1 µs
Up-conversion C_{up}	1.1×10^{-23} m^3s^{-1}	9.1×10^{-23} m^3s^{-1}
Up-conversion C_3	2.0×10^{-23} m^3s^{-1}	5×10^{-23} m^3s^{-1}
Energy transfer C_{ET}	3.0×10^{-22} m^3s^{-1}	4.9×10^{-22} m^3s^{-1}
Energy transfer C_{-ET}	3.0×10^{-23} m^3s^{-1}	4.7×10^{-22} m^3s^{-1}

A good agreement is observed between experiments and simulation results, for both cases: spectroscopic parameters from literature or recovered by PSO. For the case of practical interest that corresponds to the pumping at the max power of ~ 10W, a limited relative error of ~3 % has been obtained using PSO recovered parameters instead of ~12 % from the simulations based on the literature parameter values. This demonstrates the interest to optimize these parameters through the PSO if experimental data are available to apply it.

V.1.2.B. Systematic investigation of the influence of a -20/+20% evolution of each spectroscopic parameter on the EYDFA amplifier performance

RE ions properties are sensitive to their local environment: the surrounding electric field due to the host matrix affects the spectroscopic parameters, as reported section II.2. This occurrence can affect the gain and the noise figure of the EYDFA. It is well known that irradiation changes the ion surroundings by creating point defects in the host matrix, Therefore, the study of the spectroscopic parameters evolution on the fiber during the irradiation and their influence on the gain is needed, especially when the dose to be considered increases. Considering only the RIA kinetics at the pump

and signal wavelengths during the irradiation allows to correctly reproduce the EDFA's degradation in a space environment. However, we expected that at higher irradiation doses, the contribution of radiation-induced changes on the spectroscopic parameters can become significant. To estimate this, using our validated simulation tools, we performed a systematic study of these spectroscopic parameters on the EYDFA performances. A representative variation of 20% was applied to each parameter and its impact on both EYDFA gain and noise figure has been investigated using the amplifier architecture previously discussed. This systematic study highlights the main driving parameters while others have a negligible impact. Figure V.5.a shows the noticeable influence of the C_{ET} energy transfer coefficient on the EYDFA gain $G = P_{out} / P_{in}$ and its noise figure at λ_s=1.55 µm. We used as the reference case the PSO-recovered input parameters from *Table V.4* (Full Square, full line), and we varied this value by +20% (empty circle, dash dot line) and -20% (empty square, dash line).

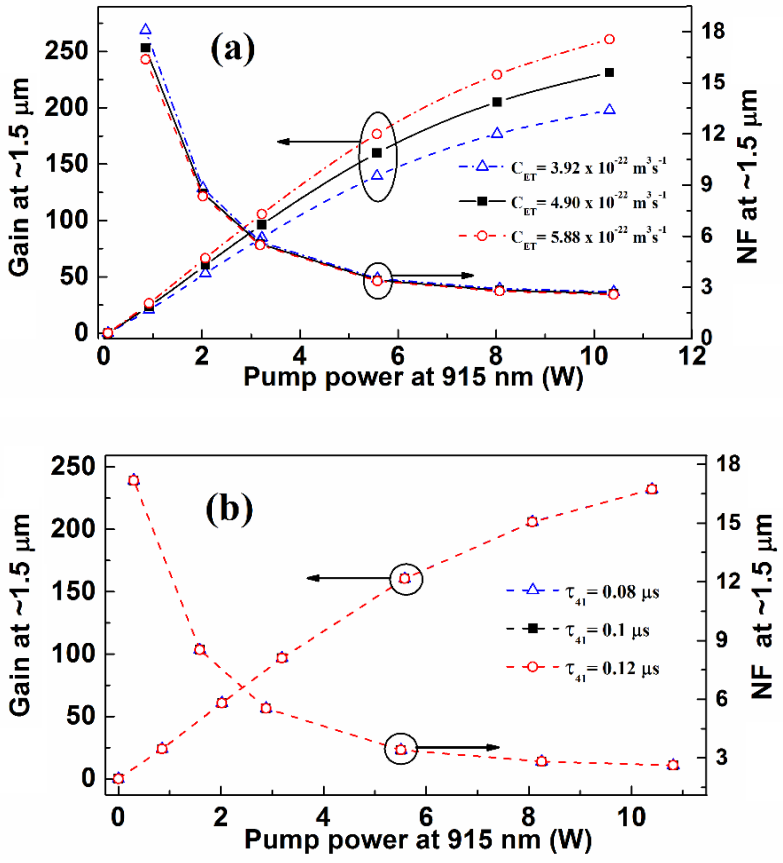

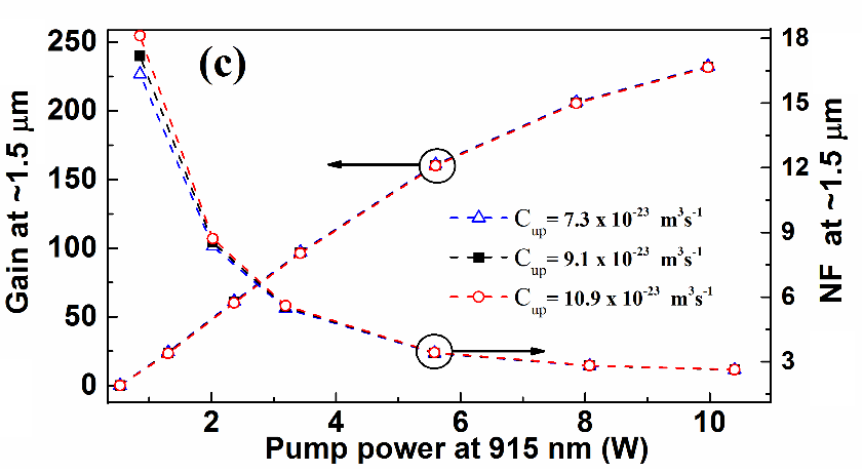

Fig. V.5. Influences of varying (±20%) spectroscopic parameters on the amplifier gain and its noise figure as a function of the pump power, (a) For C_{ET} (high influence on the gain and NF), (b) τ_{41} (low influence on the gain and NF) and (c) C_{up}: (low influence on the gain and high on the NF)

It is worthwhile to note that the influence of the C_{ET} parameter on the EYDFA gain appears more significant at higher pump power where it reaches ~17 % at the maximum pump power instead of ~13 % at 1 W input pump power. However, the noise figure has a different behavior where the highest influence is observed at lower pump powers with a maximum difference of ~ 6 % at 1 W pump power instead of ~3 % at maximum pump power. Therefore, the influence of the spectroscopic parameters on the amplifier performance depends on the pump power too. Figures V.5.b and V.5.c illustrate the same analysis for two other parameters: τ_{41} and C_{up}. Our simulations provide evidence for the negligible impact of the lifetime value variation in the ±20% range on the gain and noise figure for the various pumping conditions. For the C_{up} coefficient, its evolution can impact the noise figure but only at lower pump power that is not of practical use.

Results obtained for all the spectroscopic parameters are summarized in *Table V.4*.

Table V.4. Parameter's Impact on the gain and noise figure of EYDFA

Parameter	Parameter range	Max gain influence	Max NF influence
τ_{31} (µs)	[8.0 -12.0]	4.7 % **	3.2 % **
τ_{65} (µs)	[0.08-0.12]	< 0.01 % **	< 0.01 % **
C_{up} (m^3s^{-1})	[7.3÷10.92] $\times10^{-23}$	2.2 % *	5.1 % *
C_3 (m^3s^{-1})	[0.40÷0.60] $\times10^{-23}$	< 0.01 % ***	< 0.01 % ***
C_{ET} (m^3s^{-1})	[3.92÷5.88] $\times10^{-22}$	16.9 % ***	6.0 % *
C_{-ET} (m^3s^{-1})	[3.92÷5.88] $\times10^{-22}$	4.6 % *	2.5 % *

*** Higher effect at lower pump powers, ** homogenous effect at all pump powers, *** Higher effect at higher pump powers.**

The influence of the pump power has to be considered in the effect of the evolution of the spectroscopic parameters on the EYDFA gain and its noise figure. This will have to be considered in radiation environments as the RIA at the pump wavelength will strongly affect the pump distribution along the active fiber, in a way that could be also EYDFA architecture-dependent (forward, backward or double pumping). Indeed, some evolutions of parameters, such as C_{ET} and C_3, have a higher influence at high pump powers than at low pump powers. At the opposite, varying the C_{up} and C_{-ET} by ±20% is more impacting at lower pump powers. Parameters τ_{31} and τ_{65} have a homogenous limited and stable effect at all tested pump powers. Basing on this preliminary study, it is possible to group those parameters in three different categories, depending on the consequences of their possible evolutions under irradiation on an EYDFA amplifier performance. Some could have an important effect such as for C_{ET}, others a moderate impact such as τ_{31}, C_{-ET} and C_{up}, whereas last ones showed a negligible influence as for τ_{65} and C_3. According to those results the EYDFA simulations can be improved by recovering the parameters with a significant influence and keeping the literature values for those without impact. In this case, the calculation time can be strongly reduced without degrading the accuracy of the simulations.

V.3 SIMULATION TOOLS VALIDATION FOR AN EDFA IN ABSENCE OF RADIATIONS

In order to validate the simulation procedure, a comparison between calculations and experiments pertaining EDFA based on non-irradiated Ech1 and Ech1H_2 fibers was carried out. Two EDFA amplifiers using 8 m length of these optical fibers have been designed and manufactured with exactly the same architecture. For both of them the evolution of their output powers at 1550 nm (using 15 µW as signal input power) with the increase of the 980 nm pump diode current has been

characterized in a backward pumping configuration. By comparing the experimental results with the simulations, the strength and drawback of the developed numerical model can be evaluated.

V.3.1 Simulation input parameters

The $^4I_{13/2}$ lifetime and the absorption cross sections have been experimentally determined. Some other spectroscopic parameters more difficult to measure, such as energy transfer and up-conversion coefficients have been recovered using the PSO (Particle Swarm Optimization) as explained in the previous section V.2. Furthermore, to strengthen the confidence on the obtained values for these parameters, this comparison was done for EDFAs based on different fiber lengths and pump powers. In other words, the code optimizes the values of those parameters in order to obtain the best agreement between the simulation and the experiment for all the different configurations and pump powers using the same input spectroscopic parameters. Those results are reported in *TABLE V.5*. *TABLE V.6* reviews the fiber measured and calculated (using Mc-Cumber) spectroscopic parameters used for these simulations.

TABLE V.5. Recovered parameters using the PSO approach for the non-irradiated Ech1 fiber.

Parameter	Literature values	Recovered Value
C_2 x 10^{-23}	~ 0.8 m^{-3} s^{-1} [113]	1.2 m^{-3} s^{-1}
C_3 x 10^{-23}	10.9 m^{-3} s^{-1} [113]	7.1 m^{-3} s^{-1}
C_{41} x 10^{-23}	-	6.4 m^{-3} s^{-1}
τ_{32} ($^4I_{11/2}\rightarrow{}^4I_{13/2}$)	6.7 µs [112]	5 µs
τ_{43} ($^4I_{9/2}\rightarrow{}^4I_{11/2}$)	0.12 µs [114]	0.1 µs

TABLE V.6 Fiber measured (⊥) and calculated (◊) spectroscopic parameters.

Parameter	Value
$^4I_{13/2}$ Lifetime τ_{21}	8.9 ms (⊥)
σ_{31} Er^{3+} @ 0.98 µm	1.1×10^{-26} m^2 (◊)
σ_{13} Er^{3+} @ 0.98 µm	2.1×10^{-25} m^2(⊥)
σ_{21} Er^{3+} @ 1.555 µm	3.16×10^{-25} m^2(◊)
σ_{12} Er^{3+} @ 1.555 µm	1.94×10^{-25} m^2(⊥)

V.3.2 Simulation of the pristine Ech1 and Ech1H$_2$ EDFAs

The dependence of the output power as a function of the laser diode current is reported in Figure V.6 for the EDFA based on Ech1 (Figure V.6.A) and Ech1H$_2$ (Figure V.6.B) fibers, respectively. In both cases, the simulation results agree with the experimental ones with an error of about 3% at the maximum pump current that is the one representative of the operating conditions.

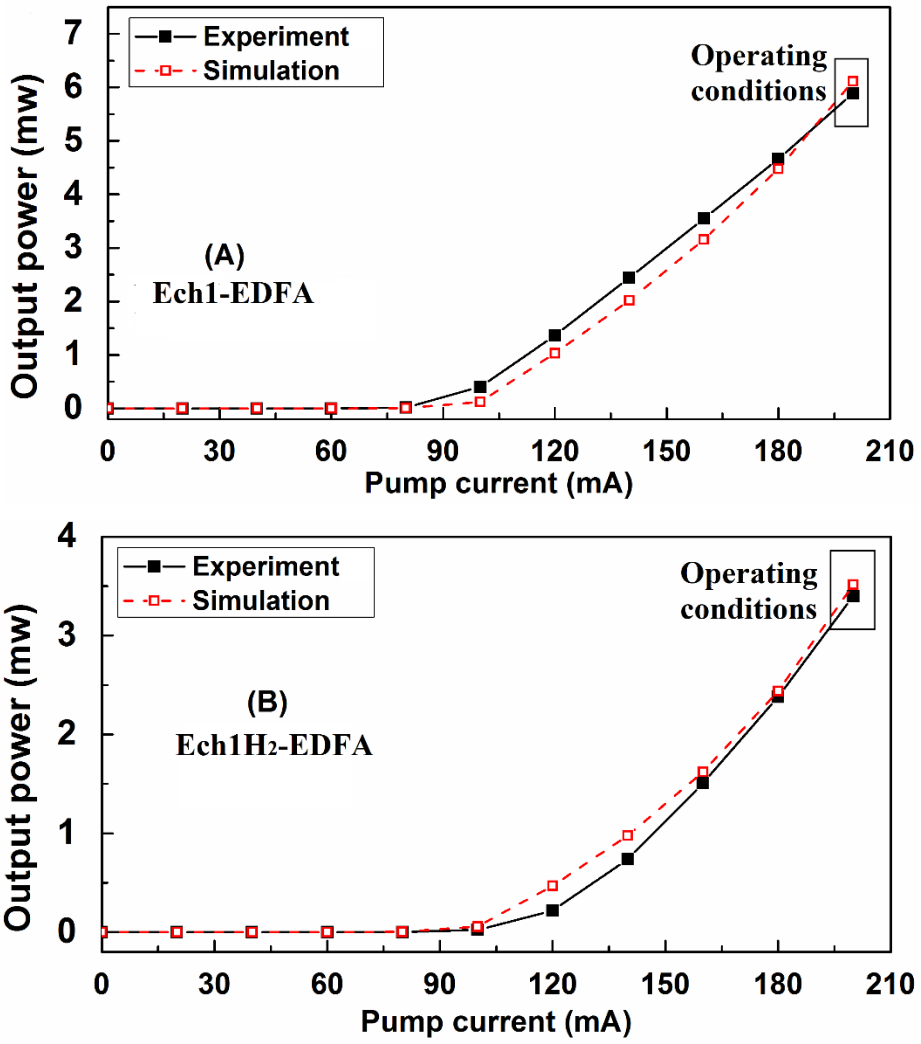

Fig. V.6. Output signal power as a function of the pump current for EDFAs made with 8 m length of (A) Ech1 sample, (B) Ech1H$_2$ sample

It is important to highlight that the same spectroscopic parameters, reported in *Tables V.5* and *V.6*, have been used to model the performances of amplifiers made with both fibers, considering that the hydrogen affects only the fiber attenuation: with 0.19 dB/m and 0.22 dB/m at about 1550 nm and 980 nm, respectively, instead of 0.02 dB/m and 0.04 dB/m in case of Ech1 sample.

V.4 VALIDATION OF THE RADIATION MODULE

V.4.1 Validation of the simulation of the Ech1 and Ech1H$_2$ EDFAs degradation under radiation

In [106], we have shown that for Er/Yb-doped optical amplifiers, it was possible to model the radiation effects on the gain by using state-of-the-art RIA measurements made with a low power white light source (P_{MIN} mode) at both the pump and signal wavelengths. Based on these previous works, we follow the same approach for the EDFA and perform simulations in various configurations, using RIA acquired in P_{MIN} mode (see Section IV.5). These preliminary results (not reported here) showed that in the EDFA case, greater attention has to be applied to the way the RIA is recorded, as photobleaching effects [115] are more intense in these aluminosilicate optical fibers. An accurate modeling of the gain degradation implies to record the RIA in the P_{MAX} mode.

The influence of hydrogen loading on the fiber response to radiation can also be analyzed from these results and simulations. It was reported in *Section I.7.A* that a fiber loaded with H_2 or D_2 provides a better response under irradiation. In Figure V.7 we reported both experimental and simulation results pertaining to Ech1 and Ech1H$_2$ amplifiers.

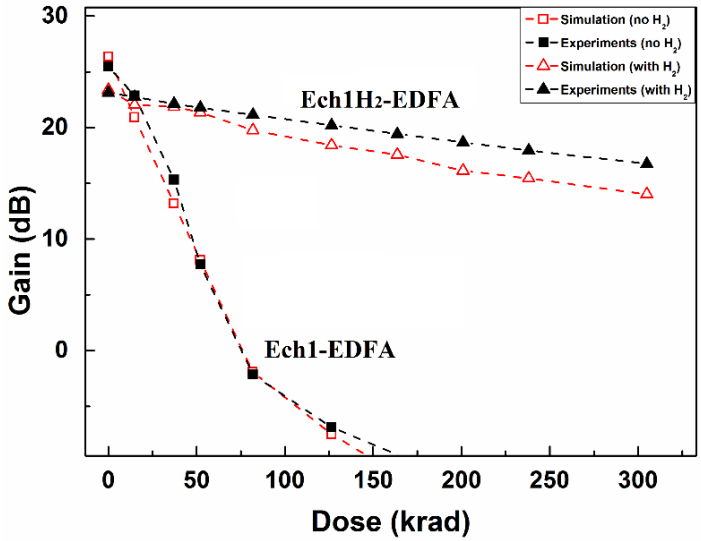

Fig. V.7. Measured and simulated gains before and during X-ray irradiation of EDFAs designed with 8m of Ech1 and Ech1H2 samples

It can be observed that the EDFA made with the hydrogenated fiber is less affected by radiations than the one done with the H_2 free fiber. Moreover, in both cases the good agreement between simulations and experiments is highlighted. The error at highest doses may be due to an overestimation of the RIA due to the limitation of our P_{MAX} configuration (only 80% of active pumping) to perfectly (<10% error) reproduce the EDFA tests where the pump in ON during the whole irradiation run. It is interesting to notice that in our simulations, the obtained RIA in the P_{MAX} configuration is the one considered for the whole length of the active fiber whereas we could expect that the RIA along the Er-doped fiber could vary as the pump power distribution is strongly not homogeneous and then the photobleaching level. A possible explanation is that for the whole range of pump powers along the fibers (from 90mW down to a few mW), the photobleaching effect is still very efficient and leads to a RIA that is caused by the part of the defects that are not sensitive to this excitation. A dedicated study is carried out in *Section VI.2* to fully characterize the photobleaching effect in such aluminosilicate Er-doped fibers.

As explained in section III.3 and III.4, the simulation also allows to calculate the EDFA associated noise figure and its evolution during the irradiation. The obtained results for both Ech1 and Ech1H_2 EDFAs are reported in Figure V.8.

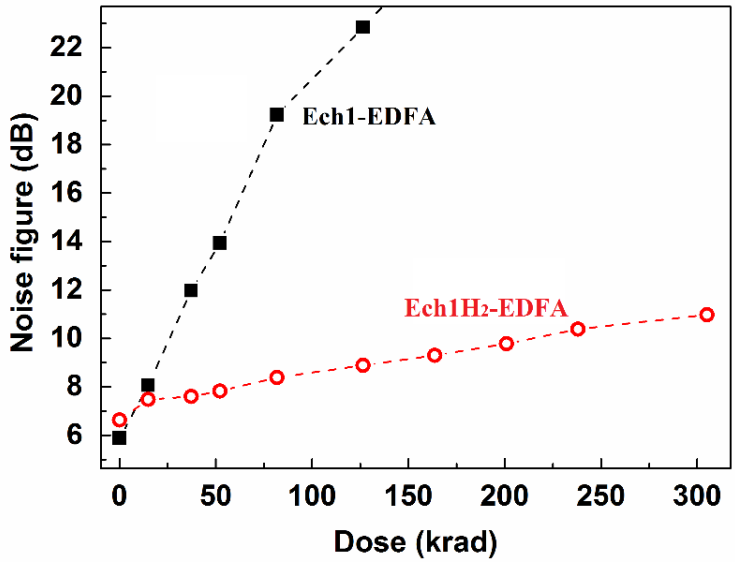

Fig. V.8 Simulated Noise figure evolution before and during X-ray irradiation of EDFAs designed with 8m of Ech1 and Ech1H_2 samples

The NF increases as a function of the irradiation dose for both EDFAs with a higher impact for the one based on the Ech1 fiber. If the NF dose dependence is compared with the gain behaviors a direct correlation can be observed.

V.4.2 Validation of the code robustness: simulation of EDFAs with different active fiber lengths

In this section, we investigate the ability of the code to predict the radiation response of different EDFA configurations using the same set of input parameters: spectroscopic parameters (see *Tables V.5 and V.6*). For this, we manufactured several EDFAs with various lengths of pristine or irradiated Ech1 fiber. Lengths of 2, 4, 8, and 12m are considered as well as three dose steps: 0, 15 and 52 krad. Figure V.9 compares the obtained experimental results and the simulation ones. To achieve these multiple comparisons, the same parameters reported in *Table V.5* and *V.6* were kept for the Ech1 fiber except the attenuation or RIA (P_{MAX} mode) values at the pump and signal wavelengths that are increasing with the dose.

For the non-irradiated sample, we observe that first the gain increases as function of the fiber length since the population inversion of excited Er^{3+} ions increases with the active fiber length. The gain is maximum for 8 m length of the active fiber and remains almost stable for longer lengths. This can be explained by the resonant absorption that compensates the stimulated emission. Indeed, a part of the pump power is drained along the fiber reducing the pumping efficiency to excite all the Er^{3+} ions at longer length. The output power starts to decrease at about 12 m length due to the pump depletion. In this case, a part of the fiber becomes not fully pumped and without the population inversion, the Er^{3+} ions strongly absorb the transmitted signal power (8.47 dB/m at 1550 nm) causing the observed fast gain degradation.

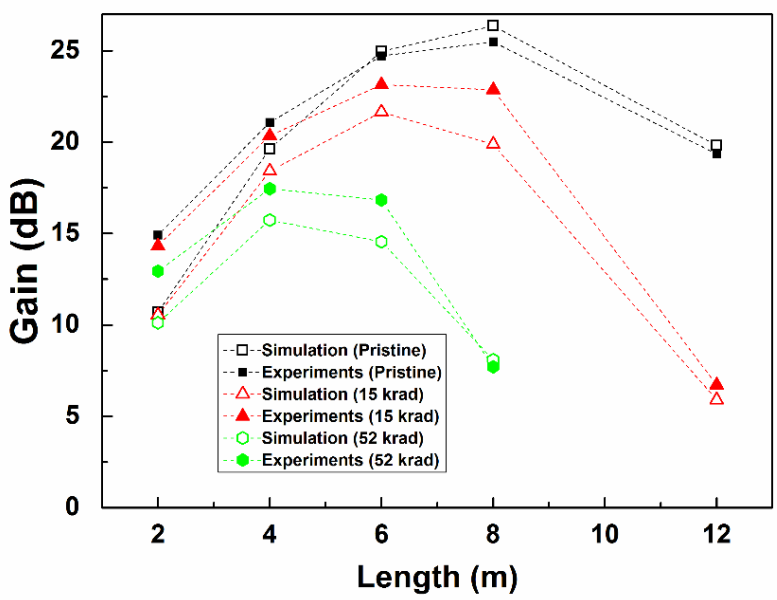

Fig. V.9 Comparison between the measured and the simulated gains of an EDFA as a function of the active Ech1 fiber length used in the design.

The fiber length is a crucial topic to be considered during the design of EDFA, even more when it has to operate in a radiation environment. The RIA causes a faster pump draining and as the dose increases an increasing proportion of the fiber may become no more pumped. In this case, the non-excited Er^{3+} ions will efficiently absorb the 1550 nm signal instead of amplifying it and then dramatically affect the amplifier performance.

Even in such complex configuration, the code shows a good ability to predict the different EDFAs degradations during the irradiation as it observed in Figure V.8. According to those results we can assume that our simulation tools are reliable and enough accurate to be used to optimize the amplifier performances in space.

V.5 USE OF THE CODE FOR THE OPTIMIZATION

After the validation steps, the developed simulation tools have been exploited to optimize the amplifier parameters in order to achieve the best radiation resistance at a given dose. In particular, the effects of both the fiber length and the pumping configuration scheme on the gain degradation with dose are investigated in the following section.

V.5.1 Optimization of the active fiber length

According to the previous results pertaining to the effect of the fiber length on the EDFA radiation response, we optimized the Ech1H$_2$ fiber length to get the best performance in the radiation environment. The numerical results are reported in Figure V.10. For a 300 krad dose, our results show that 6 m of Ech1H$_2$ fiber is the best choice for the active fiber length. It leads to an initial gain of 23 dB instead of the max gain of 24 dB using 7 m but limits its degradation down to 17 dB (-6 dB) instead of 14 dB (-10 dB). This example illustrates the fact that the optimization of the EDFA depends on the space mission profile (dose, dose rate) and will usually differ from the one that will be done on-ground without considering the radiation issues.

It is important to notice that the length optimization also improves the amplifier NF behaviors during the irradiation as shown in Figure V.10.b. In fact, the NF of the 6 m based EDFA increases from 4.8 to 6.3 dB after the 300 krad irradiation instead of from 6.9 to 10.8 in the case of the 8 m fiber length amplifier.

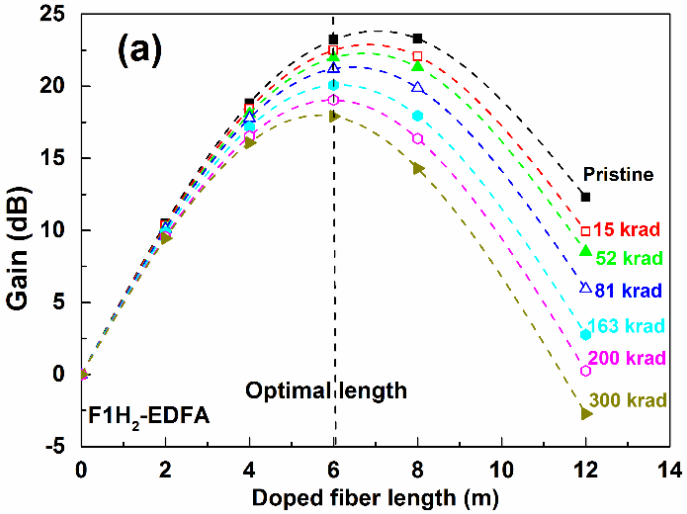

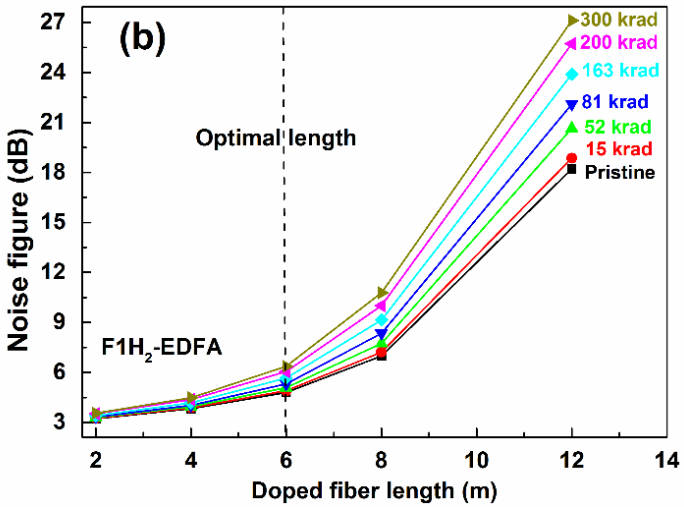

Fig. V.10 Simulation of EDFA gain (a) and NF (b) evolution with dose (up to 300 krad) for EDFAs built with various lengths of Ech1H$_2$ fibers (2, 4, 6, 8 and 12m).

V.5.2 Optimization of the pumping configuration

Different pumping configurations can also be theoretically investigated in order to evaluate their pertinences for space applications. In particular, considering the same pump (P=90 mW at 980 nm) the following simulation cases have been investigated:

- *Backward pumping* configuration, where the pump power (~90 mW) is injected from the opposite side to the signal injection. All the previously described experiments were performed using this configuration.
- *Forward pumping* configuration, where the pump power (~90 mW) is injected from the same side than the input signal.
- *Bidirectional pumping* configuration, where the pump power is injected from both sides of the RE-doped fiber (45mW at both fiber ends).

This optimization was performed for both loaded and unloaded Ech1 and Ech1H$_2$ samples using the same fiber length (~ 8m), in order to benchmark the various pumping configurations. The obtained results are reported in Figure V.11.

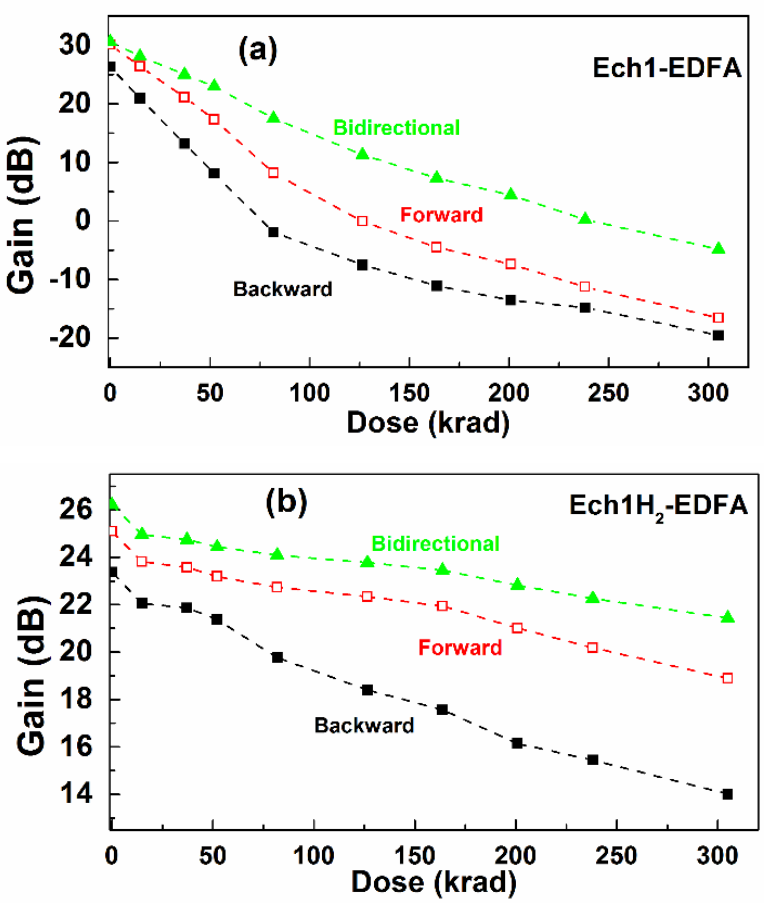

Fig. V.11. Gain evolution with the dose for EDFAs designed with different pumping configurations, backward (90 mW injected from the output), forward (90 mW injected from the same side of the input signal), double-pumping (2×45 mW injected from both sides), (A) using Ech1 sample, (B) using Ech1H$_2$ sample

According to these simulation results the bidirectional pumping configuration seems the most favorable architecture to enhance the amplifier radiation resistance in term of gain. Indeed, this configuration exploiting the Ech1H$_2$ sample is characterized by a gain degradation from ~26 dB to ~21 dB after ~300 krad, while the one based on the Ech1 sample exhibits a stronger gain degradation from ~30 dB to ~5 dB. Greater degradation is obtained for the backward pumping configuration: from ~23 dB to ~13 dB with Ech1H$_2$ sample and from ~25 dB to -19 dB for the Ech1 one. Finally, the forward pumping scheme provides moderate gain degradation results: from ~25 dB to ~18 dB for Ech1H$_2$ and from ~29 dB to -16 dB for Ech1.

According to the RIA measurements, we observed that the pump power at 980 nm is more affected by the RIA than the signal at 1550 nm (5 to 6× times more at 300 krad). The gain depends on both

the signal and pump power propagation so in the forward pumping configuration, the conversion of the pump power to amplified signal strongly occurs close to the input of the active fiber. So the converted power from 980 nm to 1550 nm undergoes losses at the signal wavelength and avoid the high attenuation at the pump wavelength along the active fiber. This explains the fact that the forward pumping scheme provides better performance than the backward one.

However, in this configuration the pump is quickly consumed and at the high doses the pump power is totally exhausted. As a result, a part of the active fiber (from the output side) is not totally inverted and the erbium ions will strongly absorb the signal power. In the case of the bidirectional pumping configuration, the pump power is better allocated along the whole fiber length than the other configuration. As a consequence, the axial population inversion inside the active fiber is more homogenous even for high dose of radiations giving the best fiber tolerance.

The previous results were obtained using the measured RIA (in P_{MAX} mode and backward pumping). So the RIA evolution during the irradiation can differ between the two configurations. However, we expected that RIA will be reduced in the bidirectional pumping configuration due to a better pump power distribution leading to a more homogenous and effective photo-bleaching effect along the active fiber. However, in the case of the forward configuration we think that the RIA should be more important at the end of the fiber where the pump power is quite low due to the strong amplification at the input of the fiber due to the pump consumption (see *Section VI.2*).

We also investigate the effect of changing the pumping configuration on the NF behaviors before and during the irradiation in both the Ech1 and Ech1H_2 EDFAs cases. The obtained results are reported in Figure V.12.

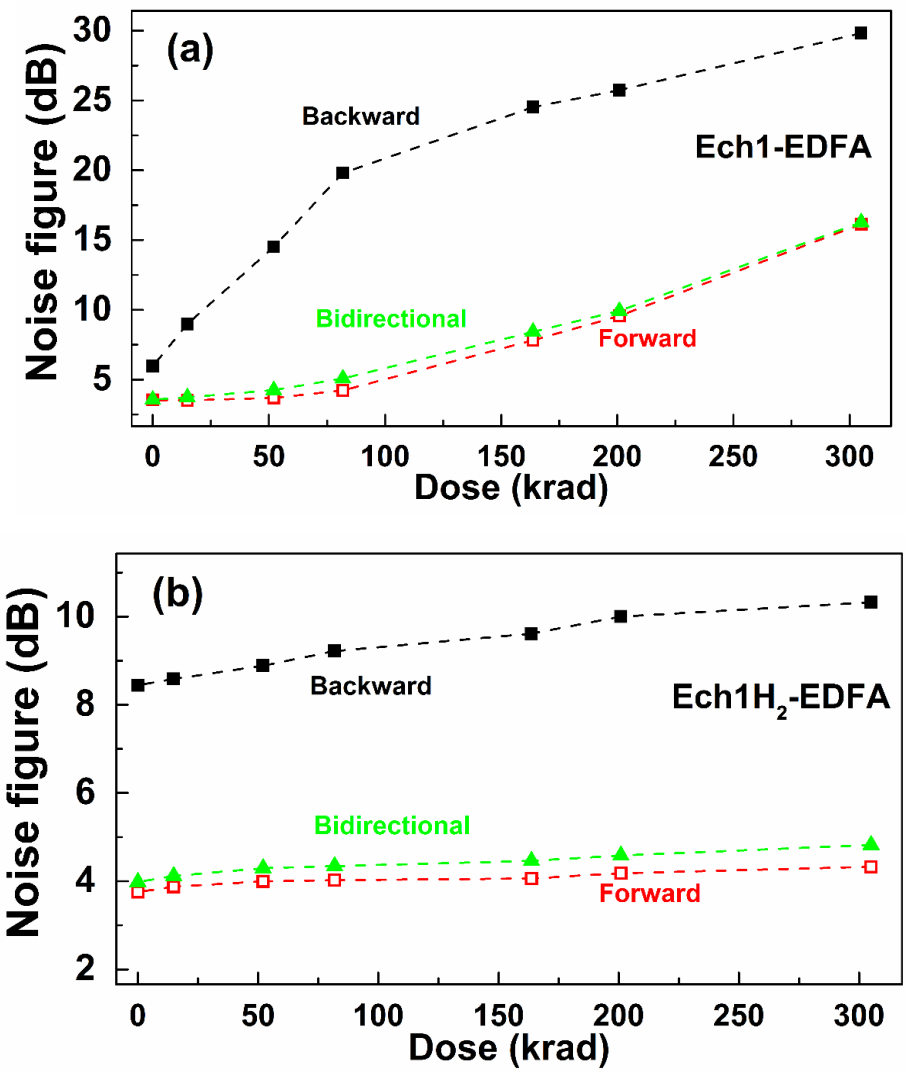

Fig. V.12. NF evolution with the dose for EDFAs designed with different pumping configurations, (A) using Ech1 sample, (B) using Ech1H$_2$ sample

In both EDFAs the backward pumping configuration induces a high NF before and during the irradiation. This result can be improved by changing the configuration to a bidirectional or forward pumping configuration. The two have quite similar behaviors, even if the forward configuration has a slightly better NF.

The NF strongly depends on the pump distribution along the fiber. In particular, if the signal is weak (at the input of the fiber), a low population inversion can induce a strong increase of the noise/signal ratio at the beginning of the fiber which will strongly affect the NF at the amplifier

output after the propagation. A better population inversion at the fiber signal input side can be achieved using the forward and the double pumping configurations.

It is also important to notice that the fiber hydrogenation induces an increase of the amplifier NF before the irradiation. Indeed, for all cases, a higher NF is observed in the Ech1H_2 EDFA compared to the Ech1 one for the same configuration. However, after few krad of irradiation, this behavior is reversed due to the fast degradation of the non-hydrogenated sample.

V.5.2 Combination of the best pumping configuration with the optimized fiber length

Finally, we combine the optimized fiber length (6 m) with the best pumping scheme bidirectional configuration to obtain the final optimized EDFA using the Ech1H_2 sample. The obtained results are reported in Figure V.13.

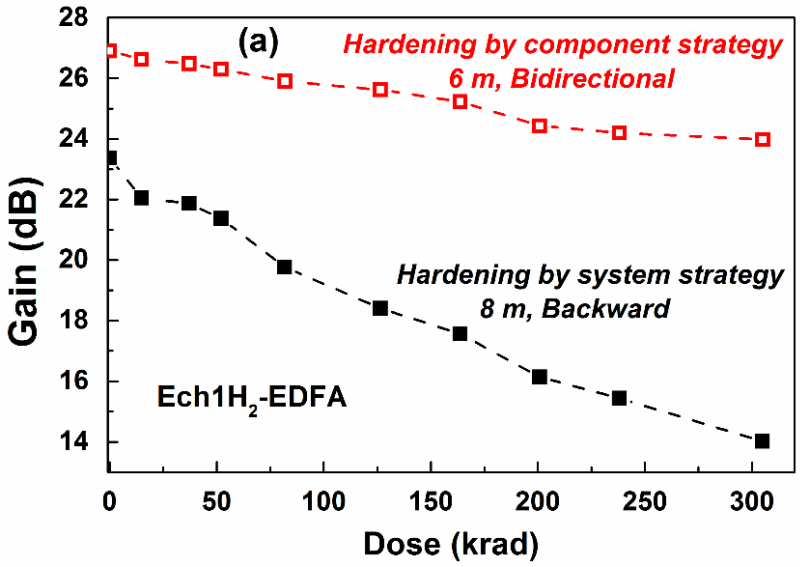

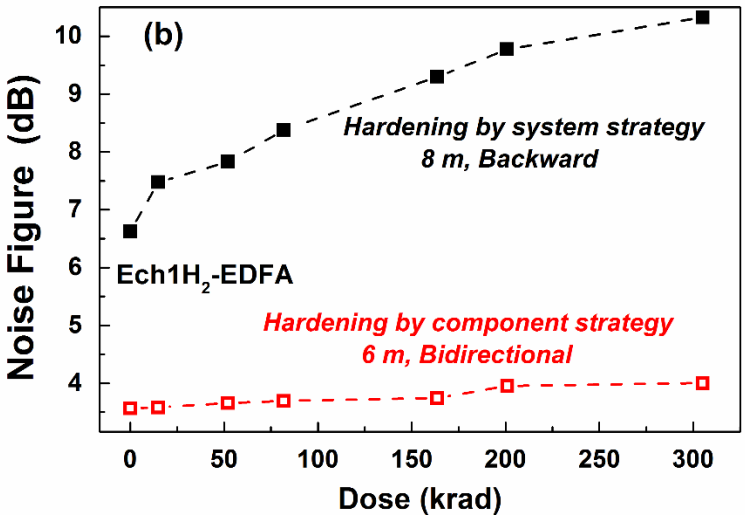

Fig. V.13 Comparison between the radiation responses of an EDFA optimized for space (6m fiber length, bidirectional pumping configuration) and for Earth operation (8m fiber length, forward pumping) a) gain b) noise figure

This optimized system for space exhibits promising radiation resistance capabilities with a gain degradation of less than 3 dB (instead of 10 dB for the original system) after 300 krad (Figure V.13.a).

It is important to notice that the optimization of the amplifier gain during the irradiation using the hardening by system strategy affects positively the EDFA NF behaviors too, which remains much lower than the non-optimized amplifier before and during the irradiation as demonstrated in figure V.13.b.

In this fifth Chapter, we compare the outputs from the experimental and simulation procedures in order to validate the developed code. In *section V.2*, we perform a parametric evaluation, through simulation, of the impact of an evolution of the main RE ion spectroscopic parameters on the gain and noise figure (NF) of the REDFA. This preliminary study allows identifying the most influential parameters and the interest of retrieving them by simulation through PSO. In *sections V.3* and *V.4* we validate respectively our model without and in presence of radiations by confronting the simulation results with the experimental ones. Finally, we use the validated code to optimize the REDFA architecture in order to mitigate the radiation effects and improve the REDFA performances before and during the space mission.

EN

Dans ce chapitre sont confrontés les résultats issus des simulations sur les REDFAs à ceux obtenus expérimentalement sur les mêmes architectures d'amplificateurs optiques afin de valider les codes développés. Dans la *section V.2*, l'influence des paramètres spectroscopiques des ions terres rares sur le gain et la figure de bruit du REDFA est évaluée numériquement par une approche paramétrique, permettant d'identifier les paramètres les plus importants et démontrant l'intérêt de remonter à leur valeur par simulation via l'approche PSO. Dans les *sections V.3* et *V.4*, les outils de simulation sont validés en absence et en présence de radiations à travers la comparaison entre les résultats théoriques et expérimentaux. Finalement le code validé est exploité pour optimiser l'architecture de l'amplificateur en vue de minimiser les effets des radiations et d'améliorer les performances du REDFA avant et pendant la mission spatiale.

FR

In questo capitolo, i risultati ottenuti dalle simulazioni vengono confrontati con quelli ottenuti sperimentalmente su amplificatori ottici dalle stesse architetture, in modo da convalidare il codice sviluppato. Nella sezione V.2, l'influenza dei parametri spettroscopici degli ioni Terre Rare sul guadagno e sulla figura di rumore del REDFA è stata valutata numericamente, attraverso la simulazione. Questo studio preliminare permette di identificare i parametri più influenti e di dimostrare l'interesse nel determinarne il valore mediante la simulazione per PSO. Nelle sezioni V.3 e V.4 il nostro modello di simulazione è convalidato in assenza e in presenza di radiazione, attraverso il confronto dei risultati delle simulazione con quelli sperimentali. Infine, il codice convalidato è utilizzato per ottimizzare l'architettura del REDFA, minimizzando gli effetti della radiazione e migliorando le prestazioni del REDFA prima e durante la missione spaziale.

IT

Chapter VI.
Implementation of additional physics in the tool: preliminary studies

VI.1 INTRODUCTION

This chapter details the experimental studies and associated numerical code developments that were conducted in order to improve the reliability and accuracy of developed simulation tools. In the first section, we characterized the photobleaching effects on the RIA of Erbium-doped fibers. This study appeared mandatory to measure the RIA in operation conditions representative to those of an operated EDFA amplifier as our results show that EDFA exhibit radiation responses that depend on their operation conditions. The results of this study strongly improve the simulation accuracy of the EDFA radiation response. Furthermore, several pumping conditions were tested to better estimate the photobleaching effect.

The second section aims to study the effects of radiation on the RE ions energy levels lifetime, focusing on those involved in the amplification process. As explained in section V.2, the spectroscopic parameters of the RE ions may change with the irradiation justifying a preliminary study of their evolution with the irradiation dose. Results of this work will also improve the accuracy of the simulation tools when applications at higher doses will be considered.

A very important issue for high power (>10 W) EYDFAs remains the thermal effects that strongly influence the amplifier performance even in absence of irradiation. A dedicated combined simulation and experimental study was carried out in the third section to evaluate the temperature increase in the fiber core and its impact on the amplifier performance in terms of refractive index profile changes, ions emission and absorption cross sections variations.

In the last section, we explain how the numerical code was finally upgraded to simulate the WDM amplifiers. Preliminary simulation results pertaining the amplification of two WDM channels using an EDFA are illustrated.

VI.2 STUDY OF THE PHOTOBLEACHING EFFECT

It was highlighted in previous section (V.3) and in [116, 117] that the degradation of an EDFA strongly depends on the amplifier conditions of operation (especially, on the selected pumping power) contrary to what was previously observed for EYDFAs [118]. As a consequence, for the

simulation of the EDFAs under irradiation, RIA measurements used as input parameters need to be measured in conditions representative of the application to obtain the best agreement between the calculated and measured amplifier gains. Particularly, in the current versions of the simulation models, the RIA is the unique input parameter used to predict the EDFA degradation [29]. Several studies demonstrate that other radiation effects such as change of RE metastable levels lifetimes [119, 120] or ion valences occur [121]. The expected impact of such spectroscopic parameters changes on the REDFA gain and noise figure was shown in section V.2 and [122]. According to this study, if such phenomenon contributes to the REDFA degradation, its impact is lower than the one related to RIA in the space dose range.

The EDFA operation conditions can widely vary from one mission to another resulting in different pump and signal powers, doped fiber lengths, dose rates etc. Furthermore, these conditions can also evolve during a mission. An example is that the main EDFA operating during the space mission is in the 'ON configuration' whereas a second backup amplifier remains unbiased in the 'OFF configuration' until it is switch ON if the main amplifier has a failure. Those evolutions induce different degradation levels of the REDFAs even if the same active fiber and length are used. In fact, the REDFA degradation during the irradiation involves several phenomena. The point defects are mainly generated due to the ionization process which is in competition with the photo/thermal-bleaching allowing their recombination [123]. The photo/thermal-bleaching phenomena are more effective in EDFAs using aluminosilicate Er^{3+}-doped glasses than in EYDFA generally based on phosphosilicate glasses with Er^{3+} and Yb^{3+} codoping (see section I.6).

In order to perform this photobleaching study, several pumping conditions (different pump powers and pumping durations) were used to characterize the RIA levels in the Ech2 fiber at fixed dose and dose rate. The main goal is to evaluate the variation range of the RIA levels when approaching the pumping conditions of the EDFA.

VI.2.1 Irradiation procedure and RIA measurement

The irradiations were performed using MOPEROX facility at Hubert Curien labs and at room temperature (RT) with a dose rate of about 0.19 Gy/s (19 rad/s) during about 4.5h to reach an

accumulated dose of about 3.3 kGy(SiO_2) (330 krad). For these RIA measurements at the pump and signal wavelengths, about 50 cm of the Ech2 fiber have been irradiated. This fiber length was optimized in order to get a homogeneous distribution of the pump power along the sample. The RIA measurement requires about 1 minute and was repeated every 19 minutes. Then, the active fiber remains pumped at about 95% of the irradiation time. The used setup is similar than the one reported in Figure IV.8.A.

VI.2.2 Pump power effect on the RIA.

To evaluate the influence of the pumping power on the RIA and then on the EDFA degradation, we performed several irradiations of ~50 cm samples of Ech2 fiber under the same conditions excepted for the injected 980 nm pump power ranging between 0 and 180 mW. RIA dose dependences for these different pump powers are reported in Figures VI.1.a (at ~980 nm) and VI.1.b (at ~1550 nm).

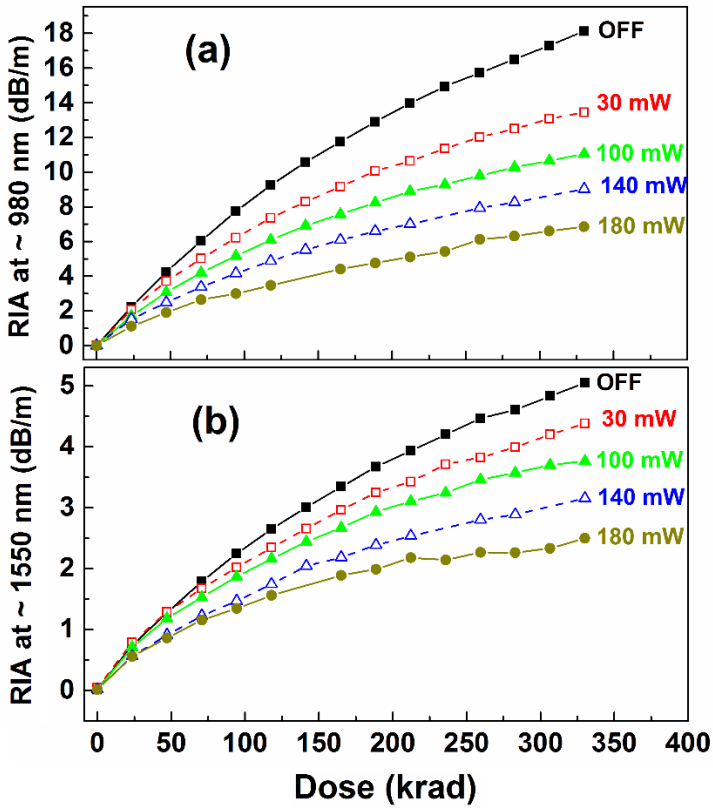

Fig. VI.1. Ech2 RIA dose dependences at a) 0.98 µm and b) 1.55 µm for various pump powers applied 95% of the irradiation time

We observe that the fiber RIA level strongly varies as a function of the injected pump power. At the maximum dose of 330 krad, RIA decreases from 18 to 6.8 dB/m and from 5 to 2.5 dB/m at the pump and signal wavelengths, respectively, between the OFF configuration (without pump power) and the P_{max} (180 mW) ON configuration. The RIA increase with the dose is observed for all the tested pump powers: a sublinear law for low doses with a saturation tendency at higher doses.

The photobleaching effect is stronger at the pump wavelength than at the signal one, with 60% less degradation at 980 nm instead of 50% at 1550 nm between the OFF and P_{max} configurations (Figure VI.2).

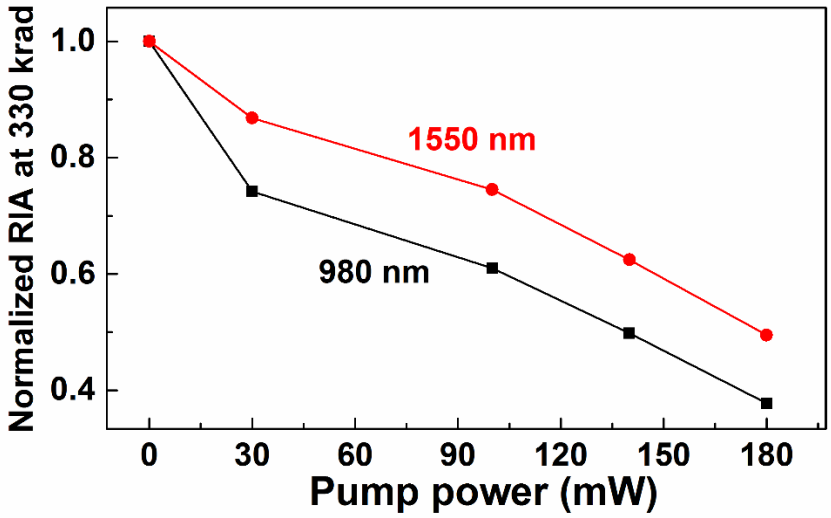

Fig. VI.2 Normalized RIA at 330 krad as a function of the injected pump power at 980 µm (black) and 1.55 µm (red)

From these results, we understand that the radiation tolerance of EDFA will depend on its operating conditions and that a 'backup' amplifier (OFF configuration) undergoes a more severe gain degradation than the 'main' amplifier (ON configuration). In addition, by an inspection of the previous results, we expect that the RIA can be non-homogenous along the doped fiber lengths in an EDFA as the pump power is drained during its propagation from hundreds of mW at the input to few mW at the amplifier output. It results in different RIA growth dose dependences due to various pump levels. Furthermore, this inhomogeneity can be reduced if suitable pumping configurations are used as for example a bi-directional pumping (see *Section V.5.2*). According to

this behavior, a more complex RIA dependence on the pump power along the fiber can be used in order to improve the EDFAs simulations under radiations.

The absorption spectra at the maximum dose (330 krad) for the different pumping powers are given in Figure VI.3.

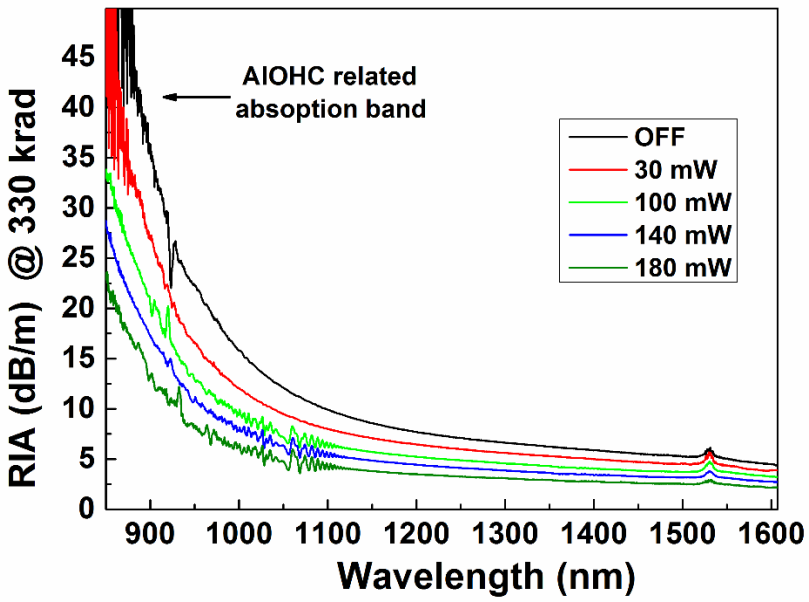

Fig. VI.3. Measured RIA spectra at 300 krad for different pumping powers

The RIA at both the signal and pump wavelengths can be explained by the tail of the absorption bands of the Al-OHC (Aluminum Oxygen Hole Centre) created during irradiation [124]. These defects are metastable at RT (transient defects), are sensitive to the temperature (thermal bleaching) and then to the light power (photobleaching) [125, 126].

IV.2.3 Effect of the pumping time on the RIA

The effect of the pumping time percentage during irradiation (ON time/ (OFF+ON) time ratio) is investigated, too. To this aim, three different tests were carried out changing the pumping time during the irradiation run. For the OFF case the pump is always unbiased and only the white source is used to probe the fiber. For the 25% ON configuration, the fiber is pumped for 5 minutes while the white light source is used for the remaining 15 minutes. The 95% ON configuration is equivalent to the one used in the previous section (19 minutes pumped and 1 minute using the white

source). For all these test cases, the P_{max} power was used. The obtained results are reported in Figure VI.4.

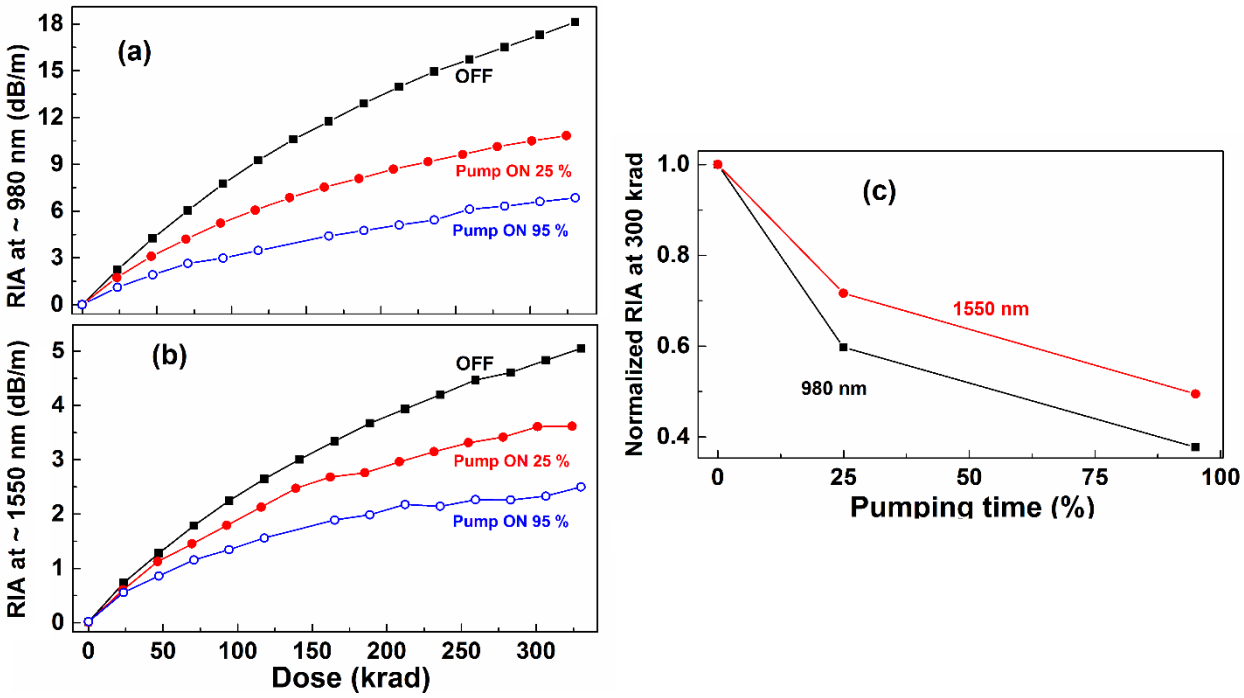

Fig. VI.4 RIA dose dependences at a) 980 nm and b) 1550 nm as a function of the pumping duration, c) normalized RIA as a function of the percentage of pumping time.

Figures VI.4 a) and b) show that the photobleaching effect depends on the pumping duration and that shortening the pumping time decreases it. This result demonstrates that the choice of the operating regime is crucial to predict the EDFA degradation; an unbiased amplifier will suffer from a larger degradation than an EDFA operated continuously during the mission.

IV.2.4 Pump effect on the fiber recovery after the irradiation

Finally, we investigate the photobleaching effect on the EDFA recovery after the end of the irradiation. To this aim, both OFF and ON configurations have been considered to attain a 330 krad dose, at the end of the runs the RIA at signal and pump wavelengths has been recorded as a function of the time after irradiation. The results are reported in Figure VI.4.a) at 980 nm and VI.4.b) at 1550 nm.

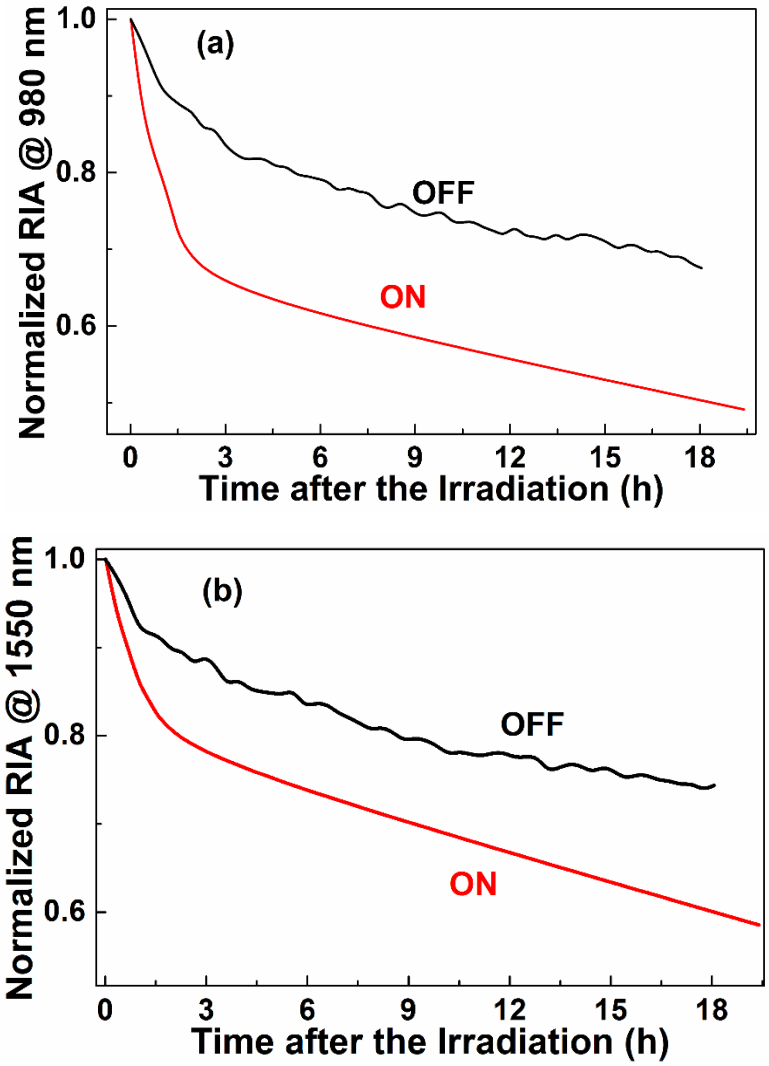

Fig. VI.4 RIA evolution as a function of time after a 300 krad irradiation in both ON and OFF configurations at a) at the pump wavelength and b) the signal wavelength.

We observe a more efficient recovery in the ON configuration at both signal and pump wavelengths compared to the OFF configuration. In fact, a 50 % recovery of the RIA is observed in the ON configuration instead of 30 % in the OFF one at the pump wavelength, and 40 % instead of 25 % at the signal wavelength.

All the obtained results highlight the photobleaching effects on the EDFAs radiation response for different configurations and operating modes. This better understanding of the RIA at the wavelengths of interest will be used as input parameters for the EDFAs simulations increasing the model accuracy.

VI.3 RADIATION EFFECT ON RARE-EARTH LIFETIMES

In this section, we investigate the evolution of the Erbium $^4I_{13/2}$ and the Ytterbium $^2F_{5/2}$ energy levels lifetime in phosphosilicate fibers, representative of state-of-the-art of commercial REDFs, from low doses (10 Gy) up to MGy levels. Moreover, this investigation was also performed on an Er/Ce codoped sample, being one of the most radiation resistant fiber ever reported in terms of RIA [37] to investigate if the Ce also preserves the optical ion properties [127]. Finally, low temperature measurements and spectroscopic analyses have also been carried out to improve our understanding of the different basic mechanisms taking place in irradiated silica-based optical fibers.

VI.3.1 Experimental procedure

VI.3.1.A Studied sample

For this study, a dedicated set of single mode (at 1550 nm) phosphosilicate optical fibers with octagonal DC geometry manufactured by iXBlue were considered. Samples PYb and PYbEr are Yb^{3+} and Er^{3+}/Yb^{3+} co-doped, respectively. PYbErCe sample is co-doped with Er^{3+}/Yb^{3+} and Ce^{3+}. Table VI.1 summarizes their main characteristics.

Sample	[P] (wt. %)	[Yb] (wt. %)	[Er] (wt. %)	[Ce] (wt. %)	Core diameter (μm)	Outer cladding diameter (μm)
PYb	8.7	3.3	-	-	8.3	125
PYbEr	8.8	3.5	0.08	-	12.9	125
PYbErCe	12.1	1.5	0.07	~0.6	6	135

VI.3.1.B Irradiation procedure

For this study, several facilities were used to cover the variety of radiation fields: X-rays, protons, γ-rays and electrons: For the X-rays, tests were performed using the MOPERIX X-ray facility with dose rate ranging from 3.6 to 180 kGy(SiO_2)/h. Proton irradiation was performed at the PIF facility from TRIUMF laboratories (Vancouver, Canada) with protons of 480 MeV energy. Gamma irradiations were performed using ^{60}Co sources having energy of 1.2 MeV. For low doses [30-300

kGy] the irradiation was performed at the IRMA facility of IRSN Institute (Saclay, France) using a dose rate between 0.2 and 2 kGy/h whereas higher doses [0.3-10 MGy] were carried out at the BRIGITTE facility of SCK-CEN (Mol, Belgium) using dose rates ranging between 10 and 30 kGy/h. Electron irradiations were carried out at CEA DAM center of Gramat (France) with the ORIATRON facility delivering electrons with energy of ~6 MeV at dose rate ranging from 42 to 78 kGy/h. All these irradiations were executed at RT between 20 and 35°C. All the reported measurements were performed more than 3 days after the end of these irradiations, meaning that our study is limited to the permanent radiation-induced changes.

VI.3.1.C Lifetime estimation

It was established that in an amorphous silica glass, the RE-ions-decay follows a stretched experimental law as given in Equation VI.1 [128]:

$$I(t) = A\exp\left(-t/\tau\right)^{\beta} \qquad \text{(VI.1)}$$

where A_1 is the initial luminescence amplitude, t is the time after the end of excitation, τ_1 is the lifetime of the involved energy level and β is the stretching parameter. We then used this stretched experimental law to fit the luminescence decay as a function of the time and to extract the lifetime values, it was observed that $\beta = 0.98$ provides the best fits for all the luminescence decays.

VI.3.2 Lifetimes evolution with the irradiation dose

The investigation of the dependence of Yb^{3+} $^2F_{5/2}$ energy level lifetime on the irradiation dose was done on the PYb samples irradiated at different doses and at different radiation facilities and using a 940 nm excitation wavelength. A review of the whole set of results is reported in Fig. VI.6. The lifetime obviously decreases when the dose increases: two different behaviors can be clearly distinguished. In the non-irradiated sample (reference), the measured lifetime is about ~1.8 ms. In the first zone (up to 100 kGy), the lifetime tends to decrease linearly in a log-log scale down to the 0.65 ms value at 100 kGy. For higher doses (zone 2), the lifetime remains nearly unchanged.

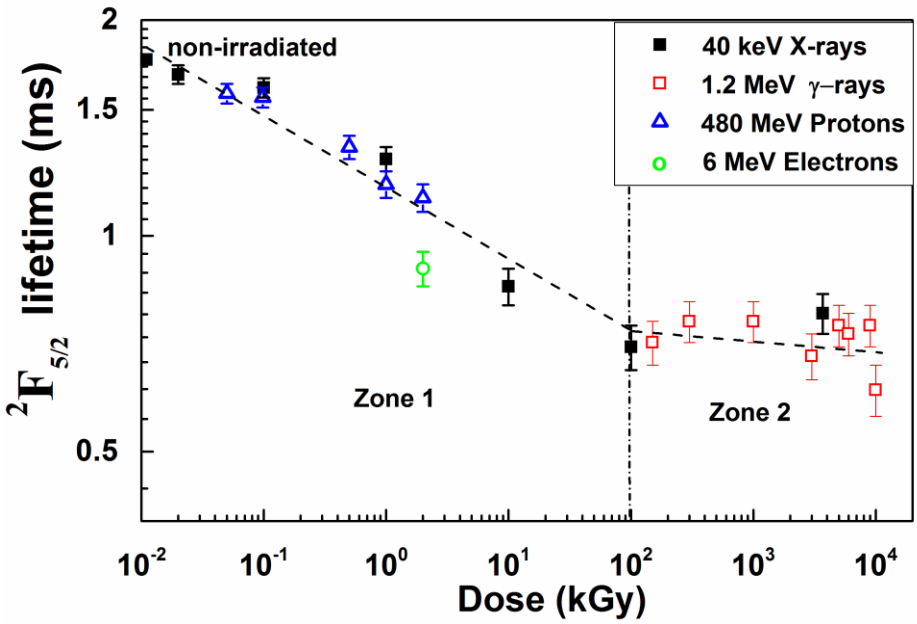

Fig. VI.6: Equivalent Dose dependence of the $^2F_{5/2}$ energy level lifetime of PYb samples irradiated with X-rays, γ-rays, protons and electrons

The luminescence lifetime of the Er^{3+} $^4I_{13/2}$ energy level was investigated under 976 nm laser excitation. In particular, its evolution with the deposited dose was studied using the samples of PYbEr irradiated in the various radiation facilities. The obtained results are shown in Fig. VI.7. In this case, three different behaviors (zones) can be easily distinguished. In zone 1 (up to 100 kGy), we also measure a linear decrease (in a log-log scale) of the luminescence lifetime from ~ 9ms (non-irradiated sample) down to ~7.5 ms at 100 kGy. Between 100 kGy and 3 MGy, the lifetime remains mostly unchanged, around 7.5 ms (zone 2). For doses exceeding 3 MGy, the lifetime starts again to decrease following another linear curve (log-log) characterized by a higher slope (zone 3).

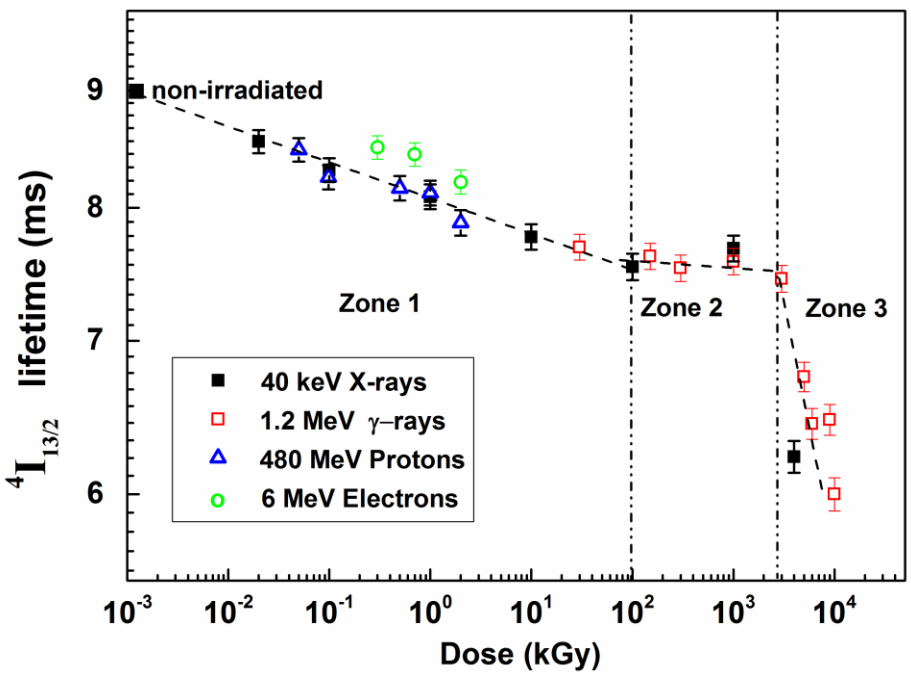

Fig. VI.7: Equivalent Dose dependence of the $^4I_{13/2}$ energy level lifetime of PYbEr samples irradiated with X-rays, γ-rays, protons and electrons

It is important to notice that similar lifetime evolutions are observed for the very different types of irradiations for both Er^{3+} $^4I_{13/2}$ and Yb^{3+} $^2F_{5/2}$ energy levels. This result highlights that, in first approximation, the RE lifetime is similarly affected by all types of radiation at equivalent doses. This is in agreement with the previous results regarding the RIA after γ-rays and proton exposures, and supporting ionization processes at the main origin of this radiation-induced effect [129, 130].

To investigate the Ce^{3+} co-doping influence on the radiation effects on Erbium lifetime, the X-rays and γ-rays irradiated samples of PYbErCe fiber were studied and the lifetimes of the Erbium $^4I_{13/2}$ energy level extracted. All obtained results are reported in Fig. VI.8.

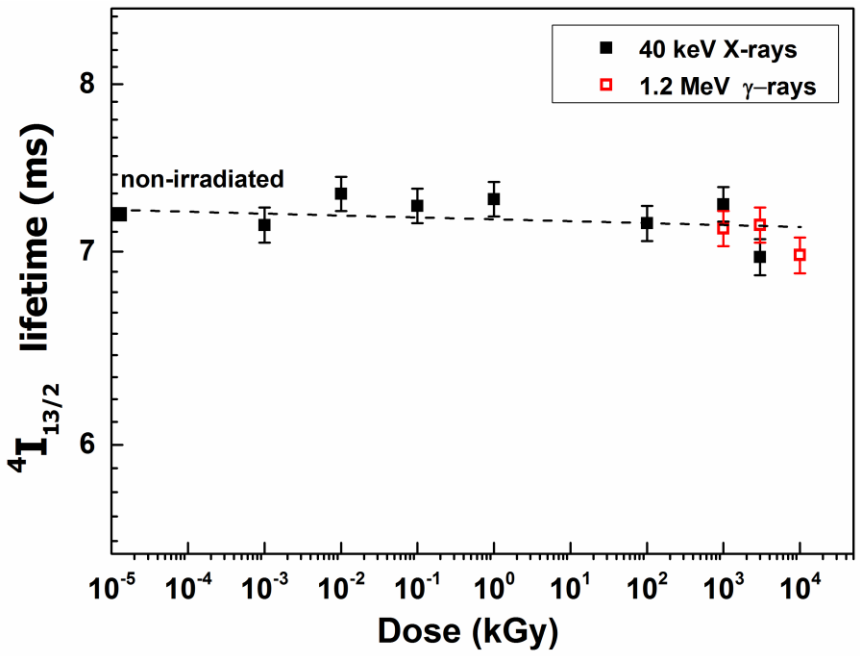

Fig. VI.8: Dose dependence of the Lifetime of the $^4I_{13/2}$ energy level lifetime of PYbErCe samples irradiated with X-rays and γ-rays.

For this Ce-codoped fiber, the erbium lifetime remains almost unaffected by irradiation. From our results, we observe a slight decrease from 7.2 ms (non-irradiated sample) to 6.9 ms (for a cumulated dose of 10 MGy) while the lifetime of the Ce free sample decreases from 9 ms to 6.9 ms under the same test conditions. Cerium is known to act as a matrix stabilizer that allows the manufacturing of radiation hardened Er^{3+}-doped and Er^{3+}/Yb^{3+}-codoped fibers [35, 131]. Fig. VI.9 illustrates the normalized Erbium infrared luminescence spectra of both non-irradiated and 10 MGy irradiated samples of PYbEr and PYbErCe fibers.

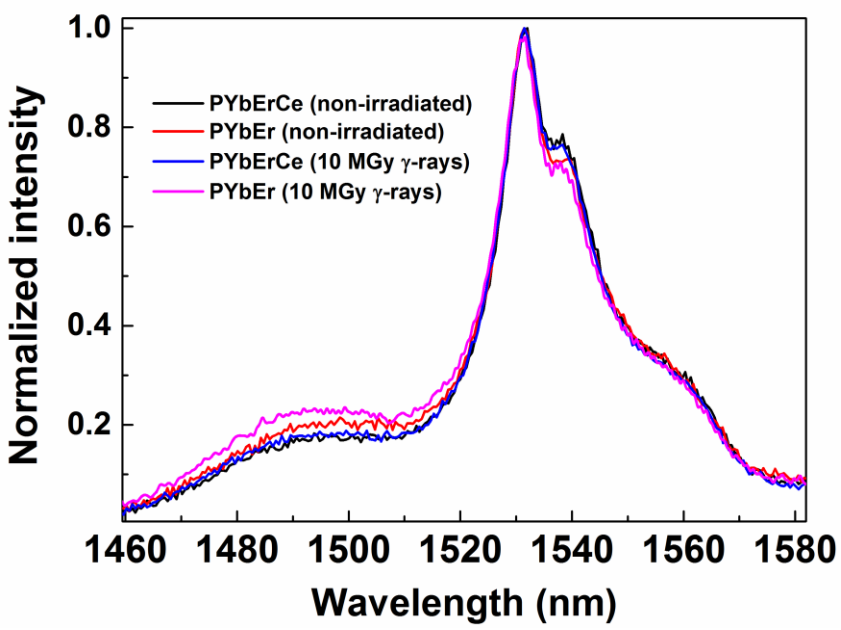

Fig. VI.9: Normalized luminescence of the Er^{3+} $^4I_{13/2}$ energy level with 976 nm pumping wavelength for both PYbErCe and PYbEr samples, non-irradiated and irradiated with γ-rays at 10 MGy dose level.

The Er^{3+} infrared normalized emission spectra have similar shapes in both samples (with and without Ce^{3+}), and this spectral shape remains mostly preserved even after 10 MGy dose.

VI.3.3 RIA evolution during the irradiation

It is interesting to characterize the dose dependence of the RIA at ~ 1550 nm during the irradiation (Fig. VI.10.a). Under irradiation, a large number of defects are created in the phosphosilicate host matrix of both PYbEr and PYbErCe samples. Due to Ce codoping, there is a decrease of the IR absorbing species (mainly P1-defects described in *section I.6.b*) in the Ce-doped sample [35] resulting in lower RIA level and different growth kinetics than those observed for the Ce-free sample. For this last class of samples, two kinetics for the RIA growth are present that seem compatible with the zones observed investigating the lifetimes in this fiber. The results were obtained in very different configurations: online for the RIA and post mortem for the lifetime. Nevertheless, for what concerns the IR absorption band of P1 defect, it is known that these active centers are stable at room temperature allowing to compare the results obtained during and after the irradiation for this particular defect [115, 132, 133]. Fig VI.10.b represents the RIA in the infrared spectral domain where we observe the P_1 related absorption band responsible of the

attenuation around 1550 nm and the Phosphorus Oxygen Hole Centers (POHC) tail which induce the RIA around 980 nm [134]. Despite this, a considerable RIA level is generated in the matrix even with the presence of Ce in the glass-composition. However, the Ce ions stabilize the Er^{3+} spectroscopic parameters during the irradiation preserving a constant value of the lifetime even at very high irradiation doses.

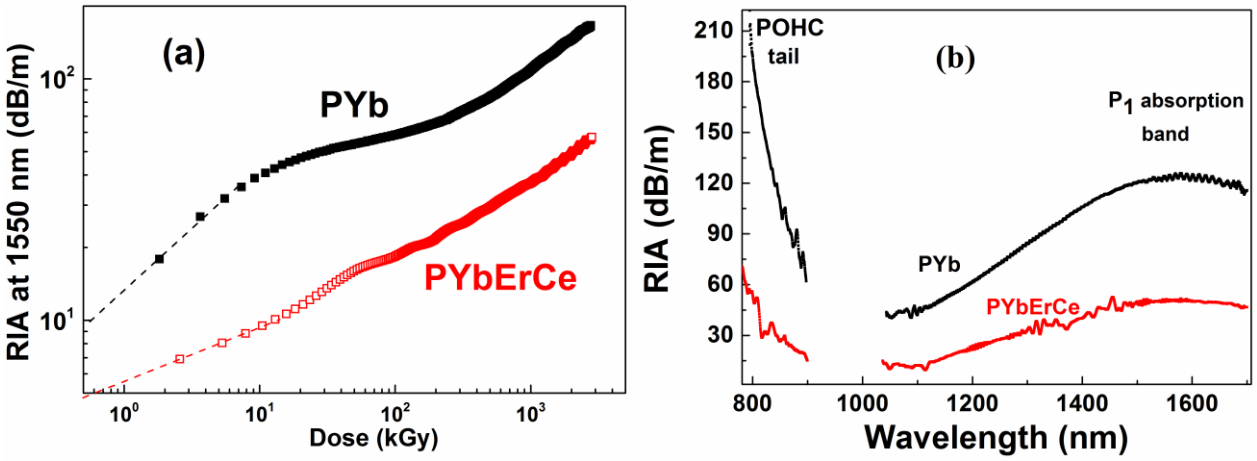

Fig. VI.10: RIA measurement on PYb and PYbErCe samples; (a) 1550 nm RIA growth dependence with dose during exposure to X-rays. (b) RIA spectra measured at the end of the X-ray irradiation at ~ 3 MGy

VI.3.4 Low-Temperature lifetime measurements

Low-Temperature (LT, at 77 K) lifetime measurements have been performed in order to investigate the behaviors of Erbium ions with and without Ce^{3+} ion presence. Fig. VI.11 compares for both PYbEr and PYbErCe samples the normalized $^4I_{13/2}$ Er^{3+} luminescence decays measured under the same conditions at RT (300 K) and LT (77 K) for both pristine and irradiated samples.

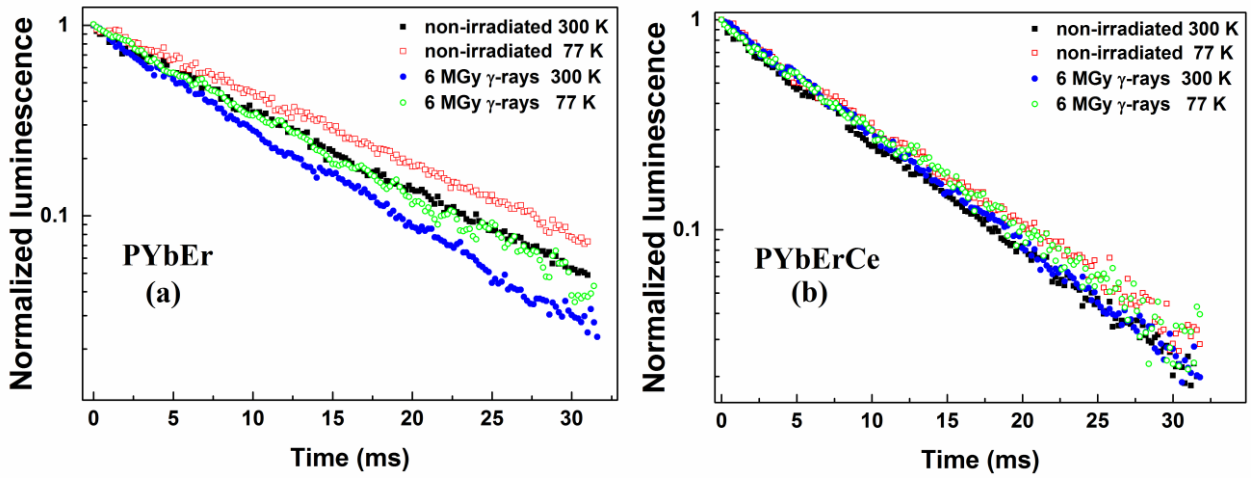

Fig. VI.11: Normalized luminescence decays of the $^4I_{13/2}$ Er^{3+} energy level at RT and LT for non-irradiated and 6 MGy γ-ray irradiated samples (a) PYbEr and (b) PYbErCe.

These results show that the lifetime increases when decreasing the temperature in both non-irradiated and 6 MGy irradiated samples of PYbEr fiber. This behavior can be explained by the decrease of the non-radiative decay rate which directly impacts the lifetime of the $^4I_{13/2}$ Er^{3+}-energy level. However, in the case of the Ce-doped PYbErCe sample, the lifetime of this $^4I_{13/2}$ Er^{3+}-energy level in presence of Ce^{3+} ions (PYbErCe) seems less affected by temperature, providing again evidence that Cerium stabilizes the Er^{3+} $^4I_{13/2}$ energy level lifetime to temperature as it does for irradiation.

Fig. VI.12 compares the luminescence spectra at RT (300 K) and LT (77 K) temperatures. Lowering the temperature clearly changes the emission spectrum and this for the two investigated optical fibers. The emission bands become sharper because of the decrease of the homogeneous line broadening mechanisms and changes of transfer-channels at 77 K. For PYbEr sample (Fig. VI.12.a) a larger diminution of the emission signal at low temperature occurs than in PYbErCe sample (Fig. VI.12.b). This behavior is caused by the reduction of the non-radiative $^4I_{11/2} \rightarrow {}^4I_{13/2}$ transition at LT which directly impacts the $^4I_{13/2} \rightarrow {}^4I_{15/2}$ transition. For PYbErCe sample the intensity is mostly preserved between RT and LT measurements. The presence of Ce^{3+} ions triggers an energy transfer phenomenon which promotes the $^4I_{11/2} \rightarrow {}^4I_{13/2}$ non-radiative transition [135].

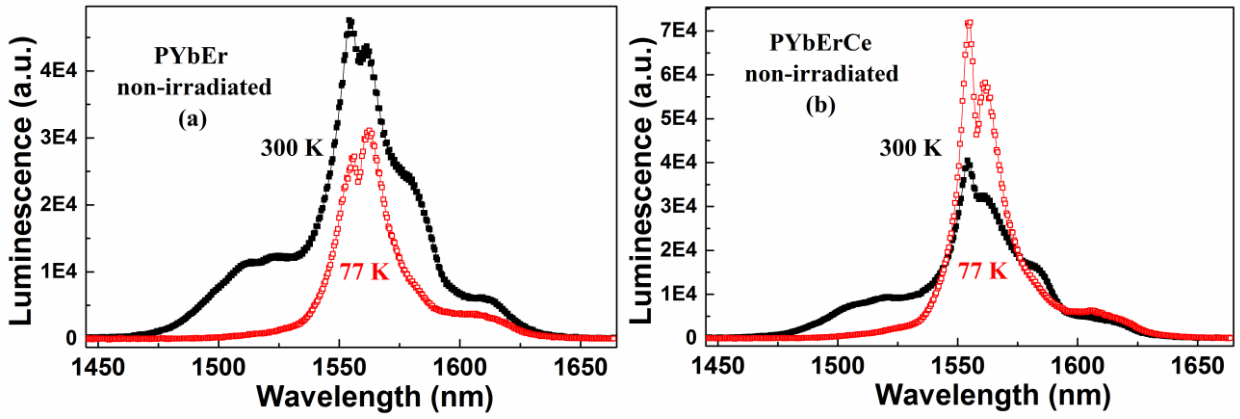

Fig. VI.12: Luminescence intensity spectra at RT (black squares) and LT (77 K, empty red squares) temperature (a) for PYbEr sample without Ce^{3+}-doping and (b) for PYbErCe sample with Ce^{3+}-doping.

VI.4 THERMAL EFFECTS ON THE EYDFA SIMULATION

The understanding of the overheating impact and its modeling is a key challenge in the design and optimization of high power REDFAs. In fact, an evolution of the temperature along the active fiber will strongly affect the amplification process and then the REDFA performance, especially if the heat is not homogeneously distributed along the fiber length and/or along its cross section.

VI.4.1 Thermal source in REDFAs

There are at least three physical mechanisms that have been identified as heating sources in the REDFA (Figure VI.13). The first one pertains the difference between the pump photon energy (λ_p=915÷980 nm) and the photon energy of the signal to be amplified (λ_s≈1500 nm). The second is due to upconversion phenomena and multiphonon relaxations. The last one is due to the intrinsic fiber losses at both signal and pump wavelengths. In absence of radiations, the first mechanism appears as the preponderant heat source. However, radiation strongly enhances the contribution related to the third process since RIA drastically increases with the dose.

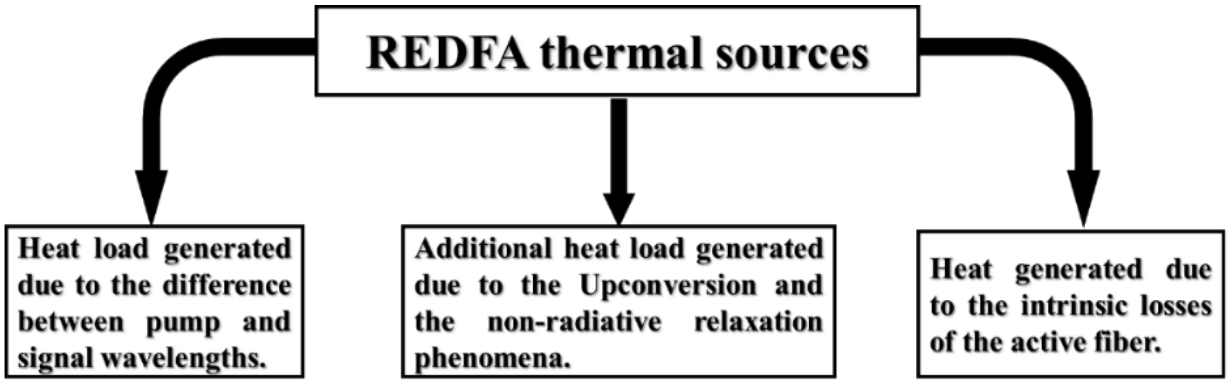

Figure VI.13. Typical thermal sources in an REDFA

VI.4.1.A Pumping and signal energy difference heat load

In high power EYDFAs, the pump energy absorbed by the RE ions is partially converted into an amplified signal via the radiative transition $^4I_{13/2} \rightarrow {}^4I_{15/2}$. As the pumping wavelength, responsible of the population inversion, is lower than the amplified signal wavelengths, a part of the input pump power is converted to heat by the fast non-radiative decay $^4I_{11/2} \rightarrow {}^4I_{13/2}$. This phenomenon induces a temperature increase of the fiber silica-based material. The amount of energy dissipated through heating is proportional to the pump and signal wavelengths ratio as described by the equation VI.2:

$$C_T = 1 - \frac{\lambda_p}{\lambda_s} \qquad \text{VI.2}$$

where λ_s and λ_p are the signal and pump wavelengths, respectively, and C_T quantifies the heat loss due to the energy difference between the pump and signal wavelengths. The C_T can be very large in the case of EDFA and EYDFA. In fact, in this class of amplifiers the pump wavelength is centered at about 915 nm while the amplified signal wavelength is at about 1550 nm. As a consequence, value of about 40% occurs.

VI.4.1.b Up-conversion and non-radiative relaxation heat load

An additional heat load can be observed in REDFAs due to the up-conversion and non-radiative relaxation phenomena. In fact, there is a coupling between the lattice vibrations and the energy levels of the higher excited states ions. The process of relaxation can occur by the energy transfer

from the excited state to the matrix phonons inducing a heat generation. Figure VI. shows the general phenomena occurring when an Erbium/ Ytterbium system is pumped at ~ 980 nm, the non-radiative transitions are represented in red dashed lines (the transition from the $^4I_{11/2}$ excited state to the $^4I_{13/2}$ energy level is the phenomenon induced by the pump and signal wavelengths difference described above).

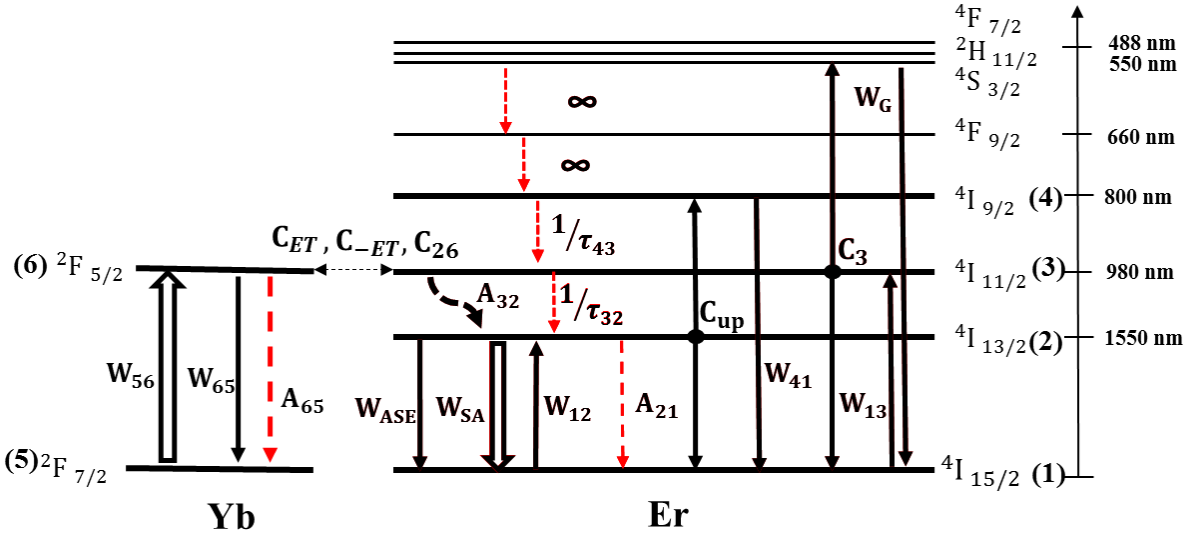

Figure VI.14. Non-radiative mechanisms (red dashed lines) responsible of the heat load in an Erbium/Ytterbium doped fiber

VI.4.1.C Fiber intrinsic losses heat load

This heat load is generated by the absorption of the pump and signal power by point defects inside the doped silica matrix. The excited point defect can relax by non-radiative transition inducing a temperature increase. This effect is usually limited in active fibers due to their low intrinsic losses (few dB/km). However, in the case of irradiated fibers the radiation-induced attenuation (RIA) that is on the order of a few dB/m can strongly extend this effect inducing an extra heat load in both core and cladding of the active optical fiber [136-142]. This effect is expected to be predominant when the EYDFA will be exposed to radiation, even at low dose levels.

VI.4.2 Heating impact on the amplifier performance and properties

The heating of the active fiber can induce different deleterious phenomena that are reviewed in Figure VI.15. The first one is the refractive-index profile change which can affect the electromagnetic field propagation and therefore the amplification of the optical signals along the fiber. The second one is a change of the material properties in particular its thermal conductivity. This last effect has a direct impact on the spectroscopic parameters of the RE ions as the emission and absorption cross sections or the homogeneous broadening.

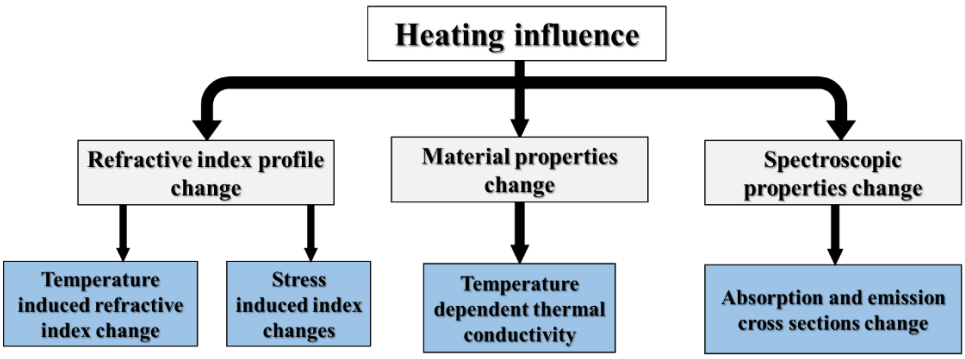

Figure VI.15. Heating influence on the different silica based materials constituting the optical ErYb amplifiers

VI.4.2.A Theoretical model

As illustrated in Figure VI.16, the cladding pumped optical fiber can be represented by a superposition of 3 successive long cylindrical layers. Considering a single mode optical fiber and the variable transformation

$$\theta(r,z) = T(r,z) - T_{\infty} \qquad \text{(VI.3)}$$

the general steady-state heat equations under air cooling are given by

$$
\begin{aligned}
&\frac{\partial^2\theta_i(r,z)}{\partial r^2}+\frac{1}{r}\frac{\partial\theta_i(r,z)}{\partial r}+\frac{\partial^2\theta_i(r,z)}{\partial z^2}+\frac{Q_i(r,z)}{k_i}=0 \quad i=1,2,3\\
&k_3\left.\frac{\partial\theta_3(r,z)}{\partial r}\right|_{r=R_3}+h\,\theta_3(r,z)\big|_{r=R_3}=0\\
&\left.\frac{\partial\theta_i(r,z)}{\partial z}\right|_{z=0}=0 \qquad i=1,2,3\\
&\left.\frac{\partial\theta_i(r,z)}{\partial z}\right|_{z=L}=0 \qquad i=1,2,3\\
&\theta_i(r,z)\big|_{r=R_i}=\theta_{i+1}(r,z)\big|_{r=R_i} \qquad i=1,2\\
&k_i\left.\frac{\partial\theta_i(r,z)}{\partial r}\right|_{r=R_i}=k_{i+1}\left.\frac{\partial\theta_{i+1}(r,z)}{\partial r}\right|_{r=R_i} \qquad i=1,2
\end{aligned}
\qquad \text{(VI.4)}
$$

where h is the convection heat transfer coefficient, k_i is the material thermal conductivity, T_∞ is the ambient temperature, $Q_i(r,z)$ is the nonhomogeneous heat source. Considering $k_1=k_2$, the thermal problem can be modeled using only two cylindrical layers having radius R_2 and R_3, respectively. As result, the equations to be taken into account are:

$$
\begin{aligned}
&\frac{\partial^2\theta_i(r,z)}{\partial r^2}+\frac{1}{r}\frac{\partial\theta_i(r,z)}{\partial r}+\frac{\partial^2\theta_i(r,z)}{\partial z^2}+\frac{Q_i(r,z)}{k_i}=0 \quad i=1,2\\
&k_3\left.\frac{\partial\theta_2(r,z)}{\partial r}\right|_{r=R_3}+h\,\theta_2(r,z)\big|_{r=R_3}=0\\
&\left.\frac{\partial\theta_i(r,z)}{\partial z}\right|_{z=0}=0 \qquad i=1,2\\
&\left.\frac{\partial\theta_i(r,z)}{\partial z}\right|_{z=L}=0 \qquad i=1,2\\
&\theta_1(r,z)\big|_{r=R_2}=\theta_2(r,z)\big|_{r=R_2}\\
&k_2\left.\frac{\partial\theta_1(r,z)}{\partial r}\right|_{r=R_2}=k_3\left.\frac{\partial\theta_2(r,z)}{\partial r}\right|_{r=R_2}
\end{aligned}
\qquad \text{(VI.4)}
$$

where the heat source into second layers is equal to 0 ($Q_2=0$). In the first layer the heat source Q_1 is

$$Q_1(r,z)=Q_p(z)+Q_s(r,z) \qquad \text{(VI.5)}$$

Q_p and Q_s being the pump and signal heat sources, respectively, given by

$$Q_p(z) = \frac{\left[\alpha_a(z)\eta + \alpha_p\right]\left[P_p^+(z) + P_p^-(z)\right]}{\pi R_2^2} \qquad \text{(VI.5)}$$

$$Q_s(r,z) = \alpha_s\left[P_s^+(z) + P_s^-(z)\right]\left|E(r,z)\right|^2$$

In eq. VI.5, α_a is the absorption coefficient at the pump wavelength, α_p and α_s are the intrinsic fiber losses, due to the RIA, at the pump and signal wavelengths, respectively, η is the fractional thermal loading expressed as

$$\eta = F_{ETU} + (1 - F_{ETU})\left(1 - \frac{\lambda_p}{\lambda_s}\right) \qquad \text{(VI.6)}$$

and $F_{ETU,}$ the fractional reduction of the population inversion due to upconversion processes is given by

$$F_{ETU} = 1 - \frac{\Delta N(z) - \Delta N_0(z)}{\Delta N_{noETU}(z) - \Delta N_0(z)} \qquad \text{(VI.7)}$$

where $\Delta N(z)$ and $\Delta N_0(z)$ are the pumped and unpumped population-inversion densities, respectively, with upconversion processes, $\Delta N_{noETU}(z)$ is the pumped population-inversion density without any upconversion effect. Solving, equations (VI.4)-(VI.7) the temperature field along both *r* and *z* coordinates can be calculated.

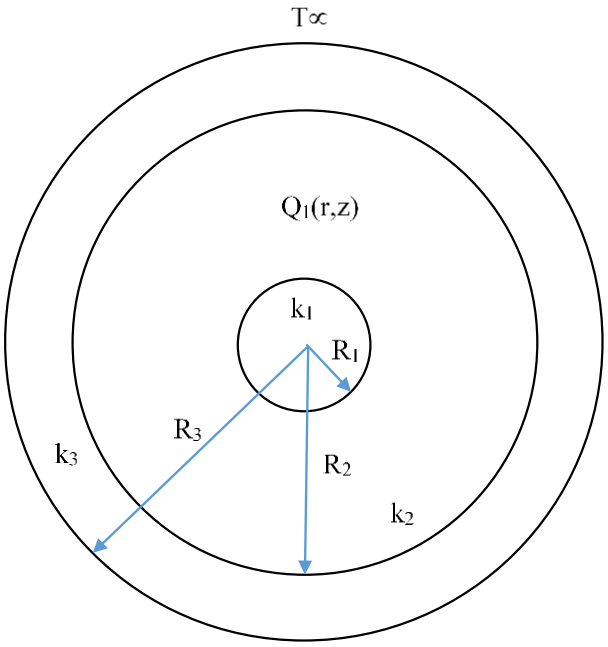

Figure VI.16: Optical fiber geometry used to solve the thermal problem.

VI.4.2.A.a. Temperature induced refractive index change

The temperature rising in the optical fiber core affects the material refractive index. In particular, if the temperature is non-homogeneously distributed in the fiber, a spatial variation of the refractive index profile occurs. This variation, changing the electromagnetic field profile during the propagation along the fiber longitudinal axis, can modify the fiber amplifier performance. The refractive index variation as a function of the temperature can be evaluated using the equation

$$\Delta n_I(r,z) = \frac{\partial n}{\partial T}\left[T(r,z) - T_\infty\right] \qquad \text{(VI.8)}$$

where T_∞ is the ambient temperature and $\partial n / \partial T$ is the thermo-optic coefficient depending on the material properties. Table I reports the thermo-optic coefficient values for different optical glasses from [143].

Table I. Thermo-optic coefficients for different optical glasses [143]**.**

Material	∂n/∂T ($\times 10^{-6}$/°C)
SiO_2	10.4
GeO_2	19.4
P_2O_5	-92,2
Al_2O_3	13.1
B_2O_3	-35.0

In the case of a doped material the $\partial n / \partial T$ can be calculated as a function of the dopant concentration f_{dopant}, normalized to 1, the thermo-optic coefficient, $\partial n_{dopant} / \partial T$, of the dopant glass and the thermo-optic coefficient, $\partial n_{host} / \partial T$, of the host glass

$$\frac{\partial n_{\text{material}}}{\partial T} = f_{dopant}\frac{\partial n_{dopant}}{\partial T} + \left(1 - f_{dopant}\right)\frac{\partial n_{host}}{\partial T} \qquad \text{(VI.9)}$$

VI.4.2.A.c. Stress induced refractive index change

As the fiber is composed of different material layers with different dilatation coefficients, the temperature variation can generate a variation of the internal stress of the fiber. This internal stress

in turn will impact the refractive index profile. Considering that the optical fiber length *L* is more important than the fiber radius r_c ($L \gg r_c$), the plane strain approximation $\varepsilon_{zz} = \varepsilon_{rz} = \varepsilon_{\theta z} = 0$ can be used. In this case, the radial, tangential and longitudinal stresses can be calculated using the equations (VI.10-VI.12) [144].

$$\sigma_{rr}(r,z) = \frac{M\alpha_V}{1-\upsilon}\left[\frac{1}{b^2}\int_0^b rT(r,z)dr - \frac{1}{r^2}\int_0^r rT(r,z)dr\right] \quad \text{(VI.10)}$$

$$\sigma_{\theta\theta}(r) = \frac{M\alpha_V}{1-\upsilon}\left[\frac{1}{b^2}\int_0^b rT(r,z)dr + \frac{1}{r^2}\int_0^r rT(r,z)dr - T(r,z)\right] \quad \text{(VI.11)}$$

$$\sigma_{zz}(r) = \frac{M\alpha_V}{1-\upsilon}\left[\frac{2\upsilon}{b^2}\int_0^b rT(r,z)dr - T(r,z)\right] \quad \text{(VI.12)}$$

Where *M* is the Young's modulus, υ is the Poisson's ratio and α_V is the thermal expansion coefficient. The index profile changes can be calculated as a function of the stress using the equation [144,145]

$$\nabla\left(\frac{1}{n^2}\right)_i = \mathbf{\Pi\sigma} = \sum_{i,j=1}^{6}\pi_{ij}\sigma_j \quad \text{(VI.13)}$$

where π_{ij} are the photo-elastic coefficients. Moreover, if we made the approximation of $\nabla\left(\frac{1}{n^2}\right)_i \cong -\frac{2\Delta n_i}{n^3}$ equation (VI.13) can be rewritten as

$$\begin{bmatrix}\Delta n_{II}^{r}(r,z)\\ \Delta n_{II}^{\theta}(r,z)\end{bmatrix} = -\frac{n^3}{2}\begin{bmatrix}B_{\parallel}\sigma_r(r,z) + B_{\perp}\left(\sigma_\theta(r,z) + \sigma_z(r,z)\right)\\ B_{\parallel}\sigma_\theta(r,z) + B_{\perp}\left(\sigma_r(r,z) + \sigma_z(r,z)\right)\end{bmatrix} \quad \text{(VI.14)}$$

where

$$B_{\parallel} = \frac{1}{E}\left(p_{11} - 2\upsilon p_{12}\right) \quad \text{(VI.15)}$$

$$B_{\perp} = \frac{1}{E}\left[p_{12} - \upsilon\left(p_{11} + p_{12}\right)\right] \quad \text{(VI.16)}$$

p_{11}, p_{12} are the elasto-optic coefficients.

VI.4.2.B Temperature dependent thermal conductivity

When the material thermal conductivity depends on the temperature the conduction problem is non-linear. A method to overcome such drawback transforming the nonlinear conduction problem in a linear one is based on the Kirchhoff transformation

$$\eta(\theta) = \frac{1}{k_0}\int_0^T k(\theta)\, d\theta \qquad \text{(VI.17)}$$

giving

$$\frac{d\eta}{d\theta} = \frac{k}{k_0} \qquad \text{(VI.18)}$$

where k and k_0 are the temperature dependent thermal conductivity and the thermal conductivity at the ambient temperature respectively, expressed in ($Wm^{-1}K^{-1}$). Using

$$\frac{d\theta}{dr} = \frac{d\theta}{d\eta}\frac{\partial\eta}{\partial r} = \frac{k_o}{k}\frac{\partial\eta}{\partial r} \qquad \text{(VI.19)}$$

$$\frac{d\theta}{dz} = \frac{d\theta}{d\eta}\frac{\partial\eta}{\partial z} = \frac{k_0}{k}\frac{\partial\eta}{\partial z} \qquad \text{(VI.20)}$$

the transformed steady-state heat equation becomes:

$$k_0\left[\frac{\partial^2\theta(r,z)}{\partial r^2} + \frac{1}{r}\frac{\partial\theta(r,z)}{\partial r} + \frac{\partial^2\theta(r,z)}{\partial z^2}\right] + \bar{Q}(r,z) = 0 \qquad \text{(VI.21)}$$

with the following boundary conditions

$$\left.\frac{\partial\eta(r,z)}{\partial z}\right|_{z=0} = 0 \qquad \text{(VI.22)}$$

$$\left.\frac{\partial\eta(r,z)}{\partial z}\right|_{z=L} = 0 \qquad \text{(VI.23)}$$

$$k_0 \left.\frac{\partial \eta(r,z)}{\partial r}\right|_{r=R_3} + h\eta(r,z)\big|_{r=R_3} = 0 \qquad \text{(VI.24)}$$

$$\eta(0,z) \rightarrow finite \qquad \text{(VI.25)}$$

Successful transformation is limited to the following two boundary conditions

1. specific temperature at the outer boundary

$$T(R_3,z) = T_\infty \qquad \text{(VI.26)}$$

2. specific heat flux at the outer boundary

$$-k \left.\frac{\partial T(r,z)}{\partial r}\right|_{r=R_3} = q_0 \qquad \text{(VI.27)}$$

VI.4.2.C Temperature effect on the Rare-earth emission and absorption cross sections

The Rare-earth ions emission and absorption cross sections are very sensitive to the temperature. Typically, the emission cross section can be linked with the absorption cross using the McCumber theory [146]

$$\sigma_e(\lambda_k,T) = \sigma_a(\lambda_k,T)\exp\left(\frac{\varepsilon - h\nu}{k_B T}\right) \qquad \text{(VI.28)}$$

where ε is the energy difference between the two lowest energy manifolds calculated at the maximum emission wavelength, T is the considered temperature, h and k_B are the Planck and Boltzmann constants, respectively. However, this dependence cannot be estimated using the McCumber theory (equation VI.28). In fact, as it was demonstrated in recent studies that this theory seems to break down at high temperature. This aspect has been studied more in detail during this PhD thesis by investigating experimentally the temperature dependence of the absorption and emission cross sections of Erbium ions and the absorption one of Ytterbium ions. In order to characterize the evolutions of these cross sections as a function of the temperature, about 1 meter of the Ech1 (*Erbium doped Aluminosilicate single mode fiber*) for the Erbium and 2 cm of Ech 3 (*Erbium/Ytterbium doped phosphosilicate fiber*) were spliced to SMF 28 pigtails connected to the

signal source and detector. The absorption and luminescence measurements were performed using a white light source and a 980 nm pump diode (with 90 mW output power). The switching between the pump probe and the white light source has been performed using a Thorlabs OSW8104 - PRO8 Series Optical Switch, and a YOKOGAWA Optical Spectrum Analyzer was used to record the emission and absorption spectra.

The samples were kept in a Nabertherm oven with a temperature stability of about 2 °C. The range from 23°C to 496 °C was investigated with about 100 °C steps. Moreover, the temperature was stabilized for 20 minutes before the measurement. For each measurement, a restoring step at a temperature of 50 °C was used in order to avoid that the applied temperature affecting the fiber guiding properties affects the quality of measurements. Figure VI.17 illustrates the used experimental setup.

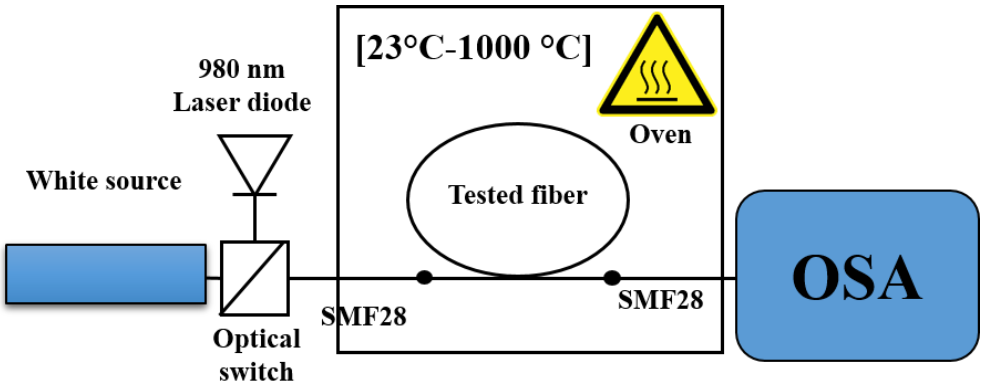

Figure VI.17. Experimental setup for the absorption and emission cross section measurement

a) Erbium emission and absorption cross sections temperature dependency

Figure VI.18. illustrates the Erbium emission and absorption cross sections versus the temperature in the range 23÷496 °C. Increasing the temperature, both emission and absorption are affected and a simultaneous decrease of the 1530 nm peak values intensity is observed.

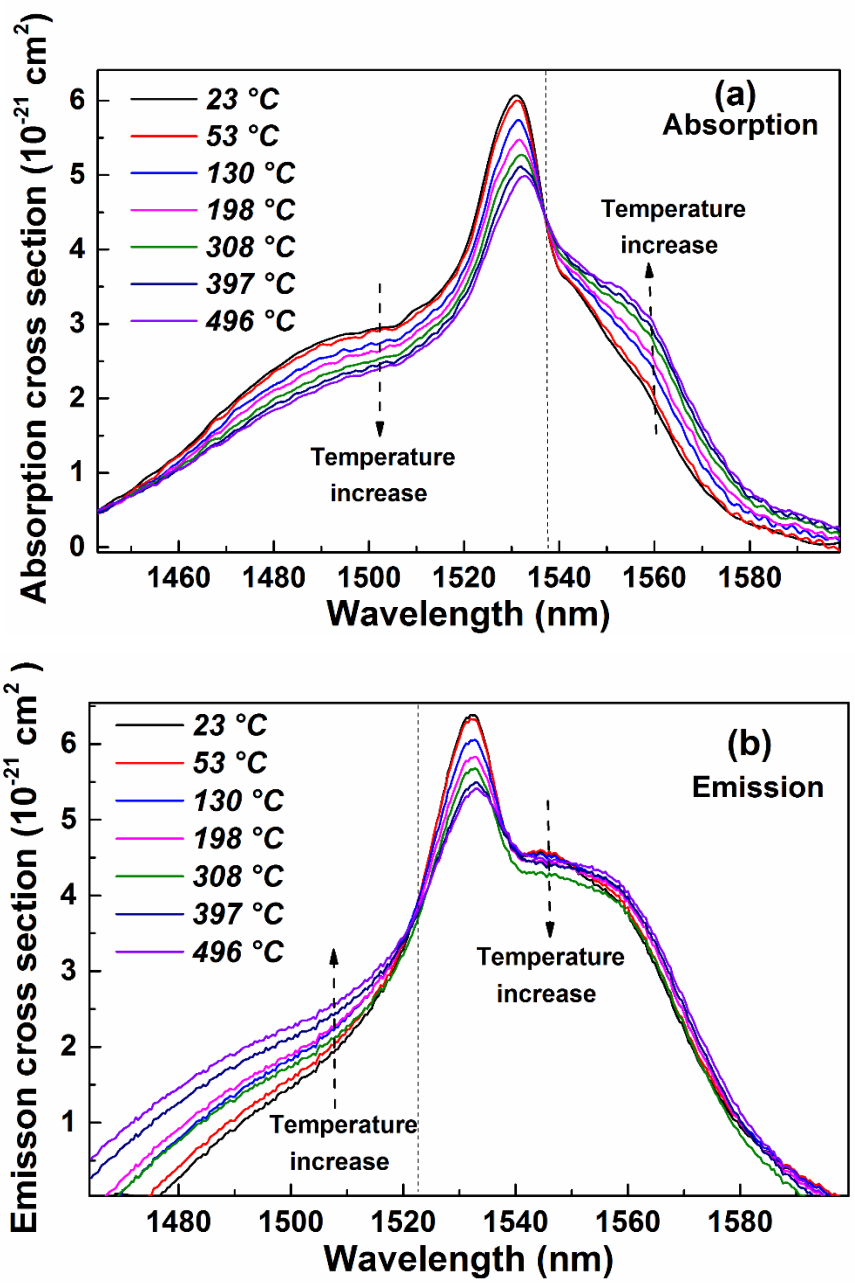

Figure VI.19. Experimental absorption (a) and emission (b) cross sections for different temperatures in a range 23÷ 496 °C of the Ech1 sample

Figure VI.19. represents the evolution of the integrated intensity over the whole spectrum as a function of the temperature for the emission (Full Square) and the absorption (Empty Square) cross sections. We noticed a 22% decrease of these integrated values for both emission and absorption spectra when temperature increases from 23 to about 500 °C.

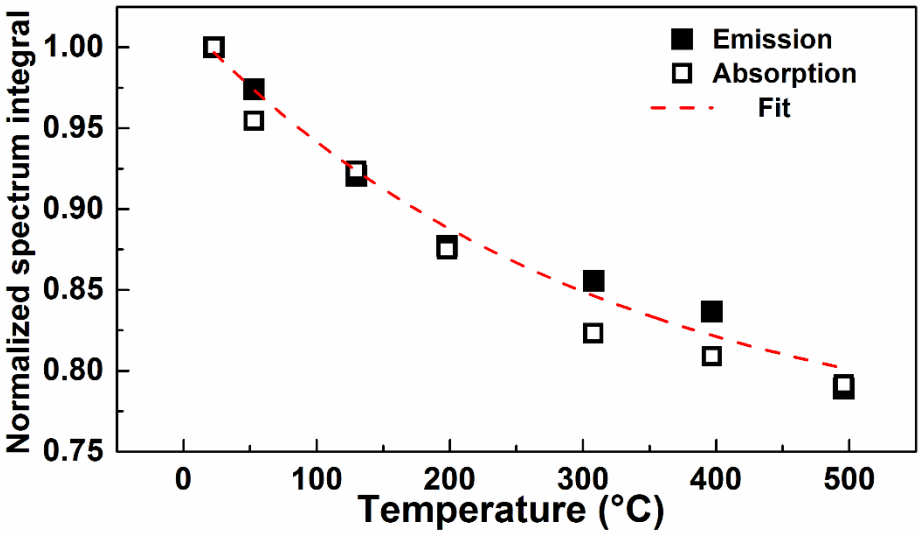

Figure VI.19. Normalized emission and absorption integrated intensity as a function of the temperature for Ech1 sample.

b) Ytterbium absorption cross sections temperature dependency

For the Ytterbium ions, the absorption cross section around the pumping wavelength of 915 nm was measured for various temperatures between RT and 500°C; the obtained results are reported in Figure VI.20.a) and b).

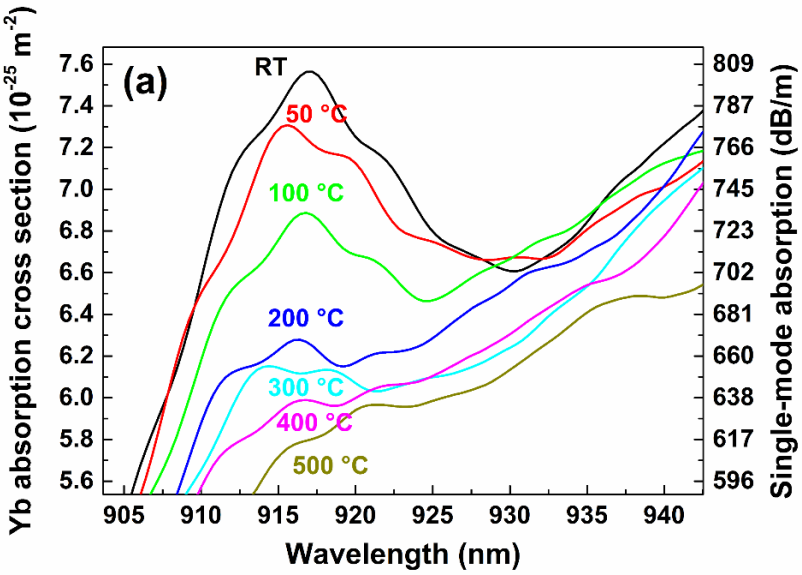

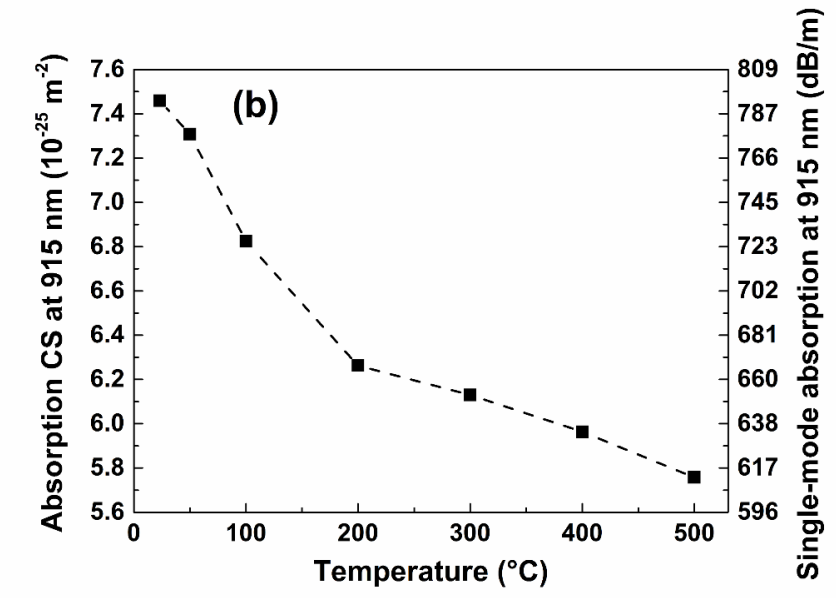

Figure VI.20. Experimental Ytterbium absorption cross sections for different temperatures in a range of [23-500 °C] of the Ech3 sample a) spectrum, b) at pumping wavelength 915 nm.

From these results, we observe that the absorption cross section at the pump wavelengths is strongly affected by the temperature and decreases from ~7.5×10^{-25} m^2, at 23 °C, to ~5.7×10^{-25} m^2, at 496 °C leading to a ~25 % decrease of the fiber pump absorption efficiency.

Of course, this decrease can strongly affect the amplification efficiency of the active fiber and needs to be included in the thermal effects simulation procedure.

VI.4.3 Physics included into the simulation chain

Figure 7 highlights in green which of the thermal effects are included in the upgraded version of our simulation chain. These are 1) the temperature impact on the refractive-index change and 2) on the spectroscopic properties of the rare-earth ions. These two parameters have been selected because they have been identified as the preponderant parameters on REDFA performance. Indeed, we expected the temperature induced change in the thermal conductivity to be negligible at the first order and this last effect will be included later if needed.

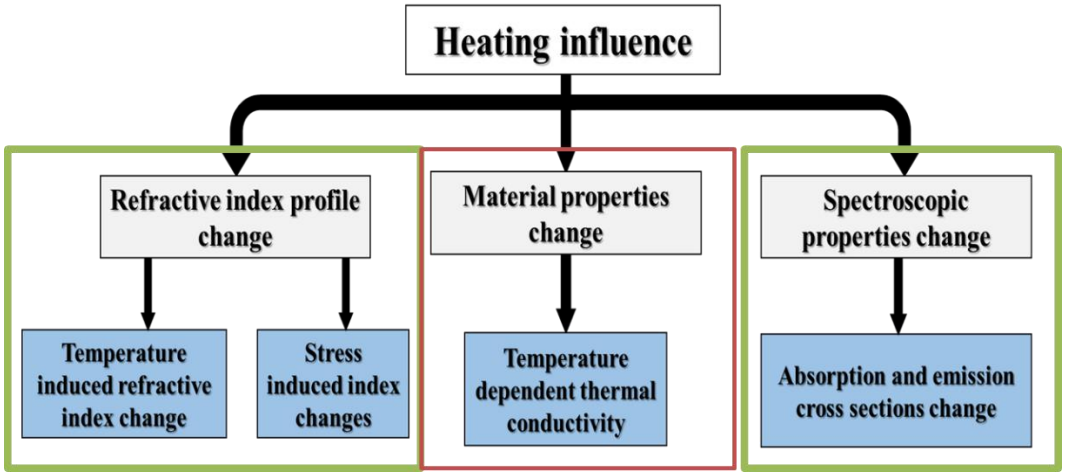

Figure VI.21. Illustration of the new physical phenomena included (green) or not (red) in the current version of the simulation chain

VI.4.4. Preliminary results of thermal effect simulations

In order to test the feasibility of the advanced numerical code coupling thermal effects with amplification phenomena, a number of simulations have been carried out. In the simulations, a double cladding fiber having a core and inner cladding diameter equal to 6 μm and 125 μm, respectively, as well as a coating thickness of 62.5 μm has been considered. The core is made of phosphosilicate glass, the inner cladding of silica glass and the coating of acrylate material. The fiber intrinsic losses are α_p=0.16 dB/m and α_s=0.04 dB/m at pump and signal wavelength, respectively. The core/cladding and coating thermal conductivity are $k_1=k_2$=0.2 $Wm^{-1}K^{-1}$ and k_3=1.38 $Wm^{-1}K^{-1}$, respectively. The convection heat transfer coefficient is h=10 $Wm^{-2}K^{-1}$.

Figure VI.22. shows the temperature on the fiber axis along the longitudinal direction for (a) different fiber lengths and (b) different input pump powers. It worth to notice a non-uniform temperature distribution and a temperature enhancement for shorter optical fibers. Moreover, the temperature exhibits a maximum corresponding to the fiber place where the pump is injected.

Figure VI.23. illustrates the longitudinal dependence of the overlapping factor for (a) different fiber lengths and (b) different input pump powers. These calculations highlight the effects on light propagation of the temperature induced refractive index change. In particular, they are stronger for shorter fibers and higher input pump powers.

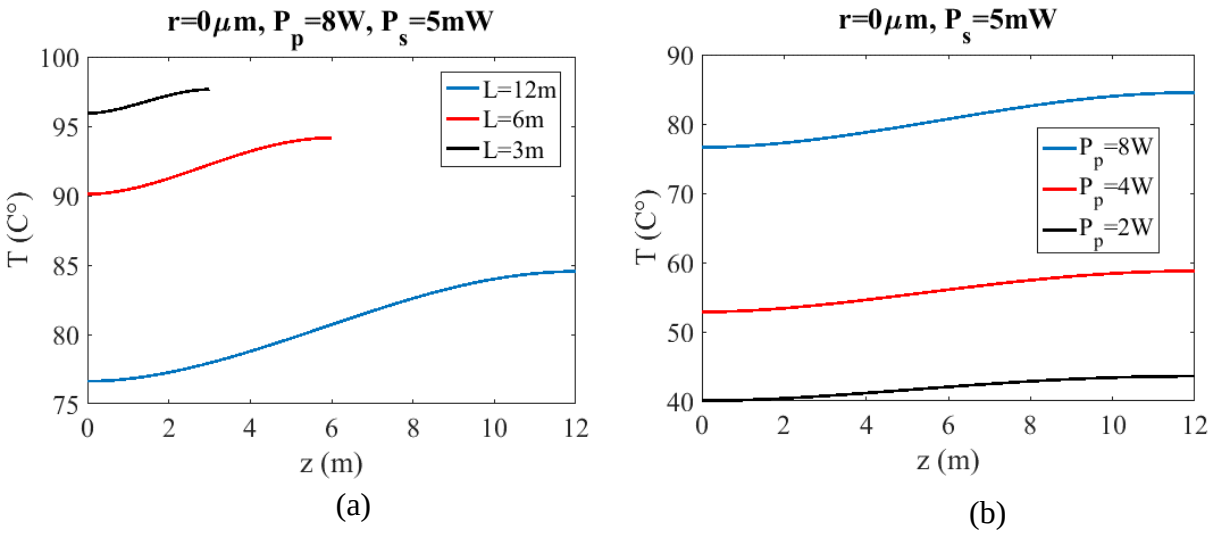

Figure VI.22. Temperature along the longitudinal direction for (a) different fiber lengths and (b) different input pump powers.

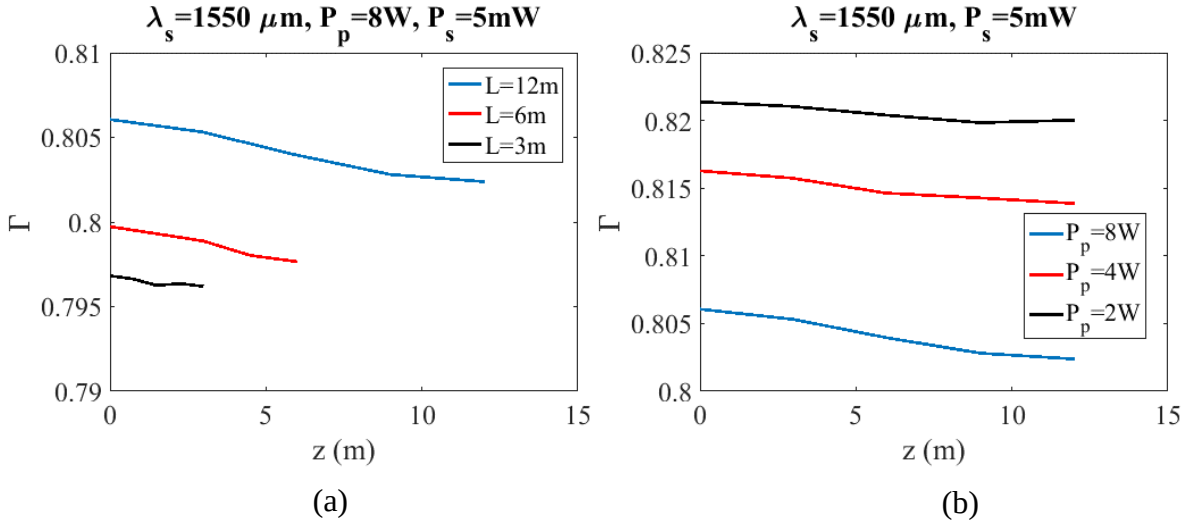

Figure VI.23 Longitudinal dependence of the overlapping factor for (a) different fiber lengths and (b) different input pump powers.

Besides the temperature increasing, the thermal effects also modify the amplifier performance in terms of gain, noise figure and pump conversion efficiency. Figure VI.24. reports the main numerical results confirming such claims. In particular, by an inspection of Figure VI.24. (a-d), a residual pump enhancement and an optical gain lowering due to the thermal effects are clearly

observed. Furthermore, a rising of both forward and backward ASE powers suggests a degradation of the noise figure with respect to the case where the thermal effects are neglected.

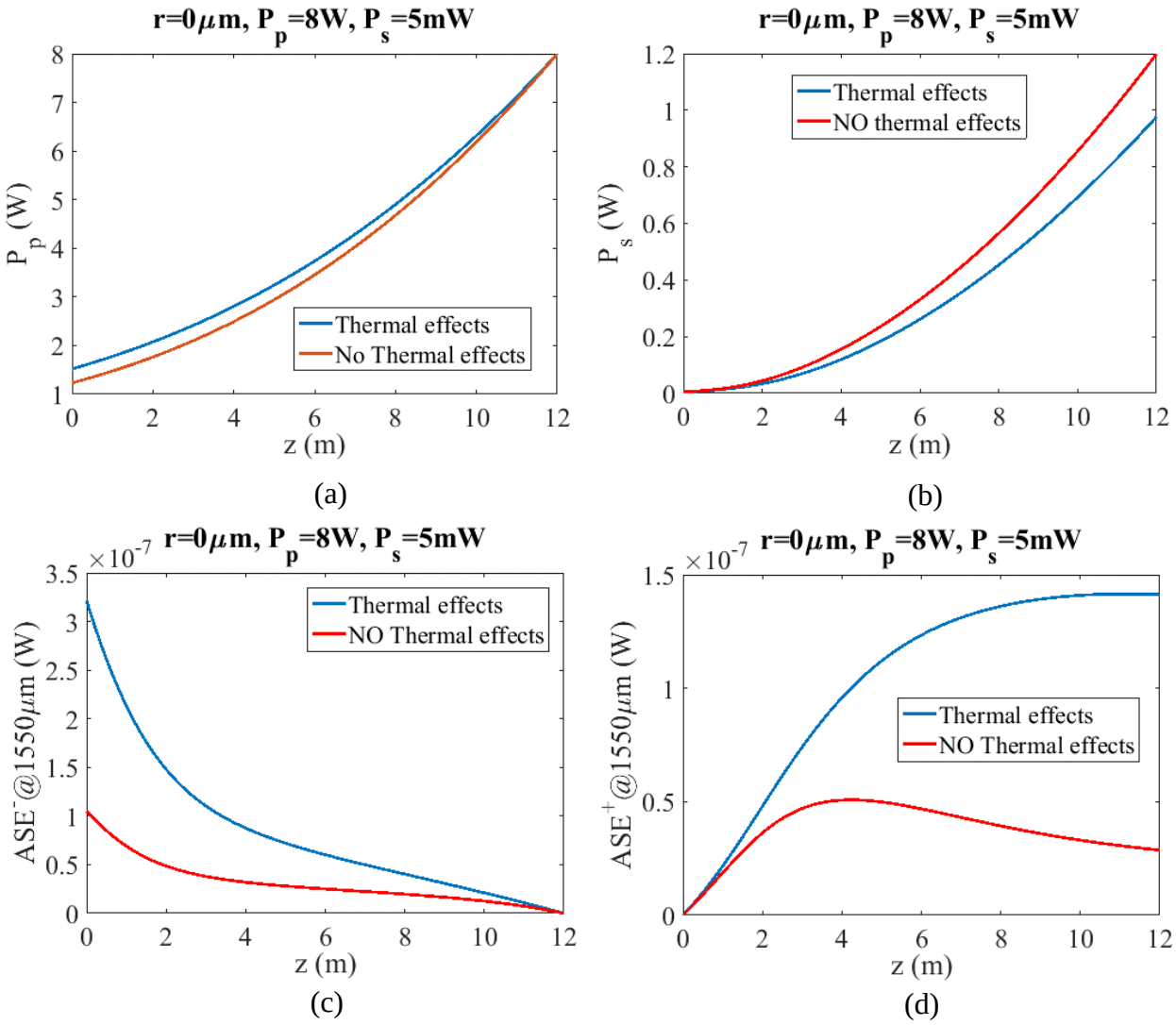

Figure VI.24. Longitudinal dependence of (a) input pump power, (b) input signal power, (c) backward ASE and (d) forward ASE by considering and neglecting the thermal effects.

VI.5 WDM AMPLIFICATION SIMULATIONS

The WDM (Wavelength Division Multiplexing) amplification using REDFAs is an important issue for the inter-satellite and satellite-earth telecommunication systems. In fact, the WDM improves

the telecommunication bandwidth allowing to reach the Gb/s of transmission speed. The integration of such technologies in space can open new perspectives in various domains as the internet coverage of poorly-covered areas or the transfer of large amounts of data from space to the ground (high resolution images, raw data of environmental analysis…).

The WDM amplification using REDFAs in the ground telecommunication systems is well-studied in the literature. However, the impact of radiation on such systems is not yet treated. The preliminary objective of this PhD work is to demonstrate that such system can be enough reliable in a harsh environment allowing their integration in space missions.

VI.5.1 Numerical Code update for WDM amplification

In order to integrate the WDM amplification in the numerical codes including the radiation effects too, we follow the same approach combining experiments and simulations that we used to validate the EDFAs modeling [1, 2] presented in the previous chapters.

The existing code was upgraded in order to consider a vector of signals input, with different wavelengths and powers, instead of a scaler value (one signal at one wavelength). In the current software version, the different channels are not able to directly exchange energy in the steady state or time-independent model of the amplifier. The interaction between channel modes is indirect through the sharing of the pump power. The changes in the code are explained in Figure VI.25.

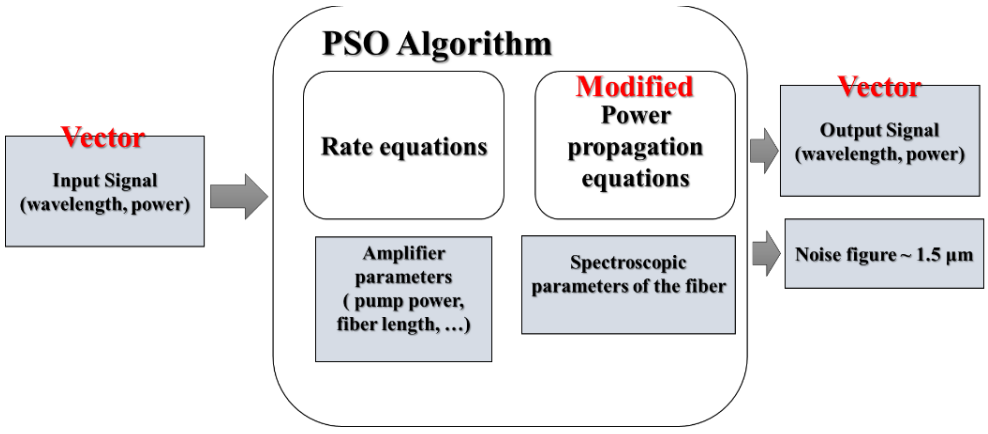

Figure VI.25. Flux diagram of the updated numerical code simulating WDM amplification.

Thanks to this upgrade, we can calculate the amplification gain and the corresponding noise figure of several signals during their propagations along the doped fiber. In other words, the number of

the power propagation equations at signal, pump and noise wavelengths increase by the number of the added input signals and the equation system becomes as follow:

$$\begin{cases} \dfrac{dP_{s1}^{\pm}(z)}{dz} = \pm\Gamma_s(\lambda_{s1})\left[\sigma_{21}(\lambda_{s1})N_2 - \sigma_{12}(\lambda_{s1})N_1 - \alpha(\lambda_{s1})\right]P_{s1}^{\pm}(z) \\ \dfrac{dP_{s2}^{\pm}(z)}{dz} = \pm\Gamma_s(\lambda_{s2})\left[\sigma_{21}(\lambda_{s2})N_2 - \sigma_{12}(\lambda_{s2})N_1 - \alpha(\lambda_{s2})\right]P_{s2}^{\pm}(z) \\ \vdots \\ \dfrac{dP_{sN}^{\pm}(z)}{dz} = \pm\Gamma_s(\lambda_{sN})\left[\sigma_{21}(\lambda_{sN})N_2 - \sigma_{12}(\lambda_{sN})N_1 - \alpha(\lambda_{sN})\right]P_{sN}^{\pm}(z) \end{cases} \quad \text{(VI.29)}$$

$$\frac{dP_p^{\pm}(z)}{dz} = \pm\Gamma_p\Big[\sigma_{31}(\lambda_p)N_3 - \sigma_{13}(\lambda_p)N_1 - \sigma_{56}(\lambda_p)N_5 + \sigma_{65}(\lambda_p)N_6 - \alpha(\lambda_p)\Big]P_p^{\pm}(z) \quad \text{(VI.30)}$$

$$\frac{dP_{ASE}^{\pm}(z,\lambda_k)}{dz} = \pm\Gamma_{ASE}(\lambda_k)\left[\sigma_{21}(\lambda_k)N_2 - \sigma_{12}(\lambda_k)N_1\right]P_{ASE}^{\pm}(z,\lambda_k) \mp \alpha(\lambda_k)P_{ASE}^{\pm}(z,\lambda_k) \pm \frac{2hc^2}{\lambda_k^3}\Delta\lambda_k\Gamma_{ASE}(\lambda_k)\sigma_{21}(\lambda_k)N_2 \quad \text{(VI.31)}$$

where $P_{sN}^{\pm}$ (with $N = 1, 2, \ldots, N$) are the signal powers concerning the different WDM channels, $P_p^{\pm}$ is the pump power, $P_{ASE,k}^{\pm}$ is the ASE power of the *k*th wavelength slot at wavelength λ_k with a $\Delta\lambda_k$ bandwidth, the + and – signs specify the forward and backward propagation waves, respectively, σ_{ij}^{e} and σ_{ij}^{a} are the stimulated emission and absorption cross sections. $\alpha(\lambda_p)$, $\alpha(\lambda_s)$ and $\alpha(\lambda_k)$ are the intrinsic background loss coefficients at the pump, signals and ASE wavelengths, respectively.

The approximation that can be applied is that the losses $\alpha(\lambda_{sN})$ and the overlapping factors $\Gamma_s(\lambda_{sN})$ at the different signal wavelengths are the same. This is true if the wavelength range of the WDM is small enough (few nanometers) so that the variation of these parameters from one signal to another remains negligible.

VI.5.2 Primary simulation results

In order to test the updated numerical code some simulations have been carried out and compared with experimental data in WDM amplification configuration. To this aim, a 10 m Ech1 fiber length amplifier was considered. We used two input signals with 1 nm separation; the first is at 1549.7 nm (channel 1) and the second at 1550.7 nm (channel 2), both with 35 µW power. The output power was calculated using as input parameters the experimental data previously acquired on this fiber. The results obtained at 278 mW of pump power at 976 nm in backward pumping configuration are reported in Figure VI.26.

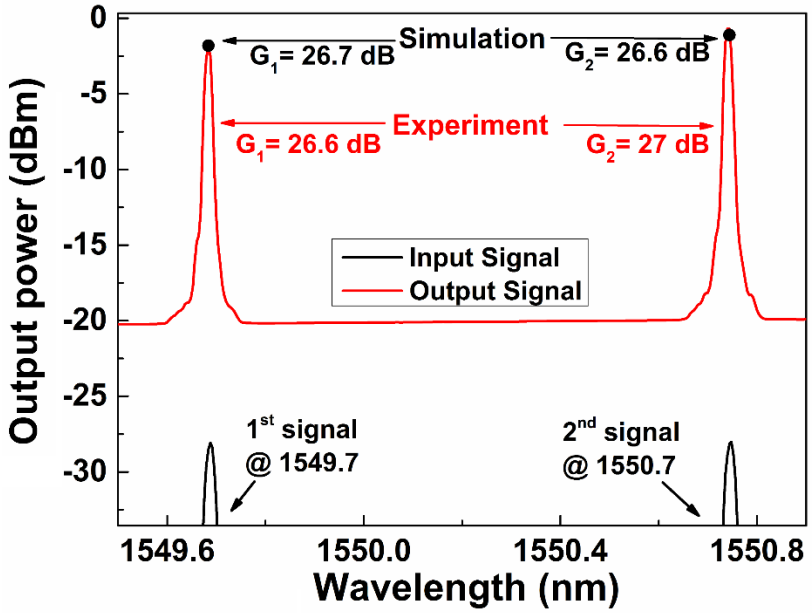

Figure VI.26. Input and output signals (experiment 'red line' and simulation 'black points') of an EDFA amplifier in the case of two input signals at different wavelengths.

We observe a good agreement between the calculated gains represented by the black dots and the measured ones represented in red lines with maximum relative errors of about 2 % observed for the second channel. The power is shared between the different channels with a ratio that appears as proportional to the flatness of the gain spectrum (about ~ 48/52 % in the case of experiments compared to ~ 50/50 % in the case of simulations).

We also compared the measured output signal power with the calculated one as a function of the pump power for both channels. The results are reported in Figure VI.27 a) at 1549.7 nm and b) at 1550.7 nm.

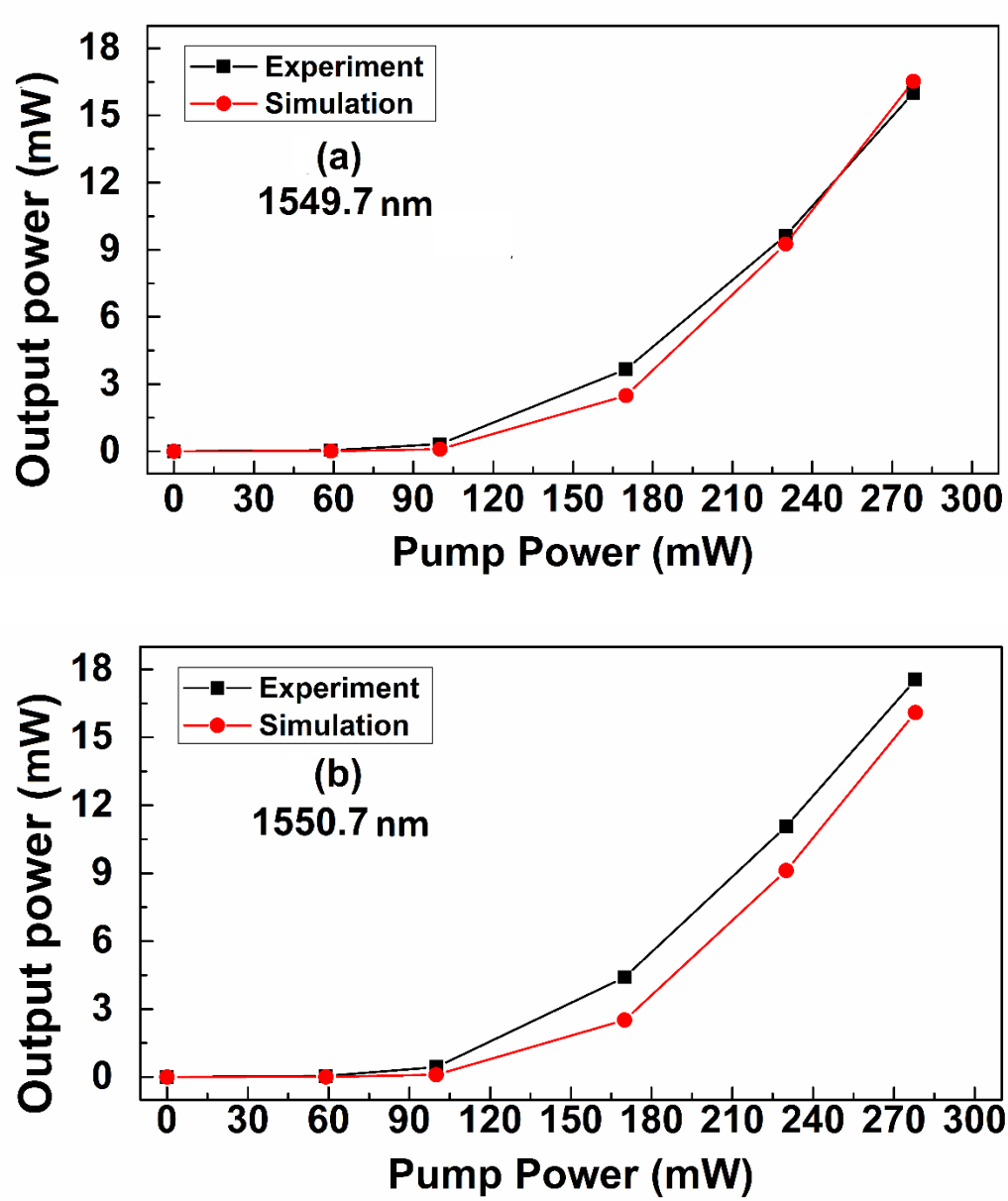

Figure VI.27. Calculated and measured output signal powers versus the pump power at a) at 1549.7 nm and b) at 1550.7 nm

A good agreement between the calculated output powers and the measured ones is observed in both cases with a relative error of about 8 % at the maximum pump power observed at the second channel. However, these simulations were performed using the recovered spectroscopic parameters reported in Table V.5 of the previous section (V.3) and the accuracy of the model can be improved by using more suitable parameters for this configuration by the means of PSO.

According to the previous results, we assume that our model is partially validated for the pristine configuration (without the radiation effects). As a perspective, the code will be validated, following the same methodology used in chapter V, for both pristine and irradiated samples in the next months.

In this last Chapter, several studies were performed in order to upgrade and enhance the accuracy of the validated code by considering additional effects expected at higher dose levels, for high power EYDFA and WDM REDFA architectures. Concerning the experimental procedure, an investigation of the photobleaching effects on the RIA in Er-doped fibers during the irradiation was carried out in *section VI.2* to increase the predictability of the code. In *section VI.3*, we study the change in the RE ions energy levels lifetimes during an exposure to different types of irradiations (X, protons, gamma, electrons…) in a large dose range. Regarding the simulation procedure, a complete modeling of the thermal effects on the REDFAs was added to our code allowing to consider their impact on the performances of EYDFA as explained in *section VI.4*. The code was also updated in order to consider complex amplification schemes such as WDM REDFAs as described in *section VI.5.*

EN

Dans ce dernier chapitre, différentes études sont présentées, menées avec l'objectif d'enrichir le code validé en incorporant des effets additionnels attendus à des doses d'irradiation plus élevées, pour des EYDFA à forte puissance, et des architectures de REDFAs multiplexées. Concernant la partie expérimentale, une étude approfondie des effets du photo-blanchiment sur la RIA des EDFAs durant l'irradiation a été menée dans la *section VI.2* afin d'améliorer la prédictibilité du code. Dans la *section VI.3* l'évolution des durées de vie des niveaux d'énergies des ions de Terres Rares durant l'exposition à différents types de radiations (X, protons, gamma, électrons…) a été étudiée dans une large gamme de doses de radiations. Au niveau des outils de simulation, une modélisation complète des effets thermiques dans les REDFAs a été implémentée dans le code afin de modéliser leur impact sur les performances d'EYDFAs (*section VI.4*). Le code a aussi été augmenté de façon à pouvoir traiter des configurations plus complexes de REDFA, notamment celles pour lesquelles le signal d'entrée est multiplexé (*Section VI.5).*

FR

Nell'ultimo capitolo, diversi studi sono presentati con l'obiettivo di migliorare l'accuratezza del codice convalidato aggiungendo gli effetti attesi a livelli più elevati di dose, per gli EYDFA a grande potenza e per le architetture degli REDFA multiplexabili. Per quanto riguarda la procedura sperimentale, è stato condotto uno studio approfondito sugli effetti del photo-bleaching sulla RIA nelle fibre dopate con Er, come riportato nella sezione VI.2, per aumentare la prevedibilità del codice. Nella sezione VI.3, l'evoluzione dei tempi di vita dei livelli energetici degli ioni Terre Rare durante l'esposizione a diversi tipi di radiazione (X, protoni, gamma, elettroni ...) è stata studiata in un'ampia gamma di dosi. Per quanto riguarda la procedura di simulazione, al nostro codice è stata aggiunta una completa modellizzazione degli effetti termici sugli REDFA, in modo da modelizzare il loro impatto sulle prestazioni degli EYDFA (sezione VI.4). Il codice è stato inoltre migliorato in modo da considerare configurazioni più complesse di amplificazione, come quelle in cui il segnale d'ingresso è multiplexato (sezione VI.5).

IT

CONCLUSION

The main objective of this PhD thesis work was to develop and exploit a new approach in order to improve the radiation hardness of existing RH REDFs based devices in order to facilitate their integration for the future space missions associated with higher radiation doses and doses rates. In this case, the conventional *hardening by component strategy* (generally by improving the active fiber radiation hardness) may not be sufficient to offer a suitable solution to these challenges, and more elaborated hardening techniques sound necessary. To this aim, the potential of an optimization of the REDFA at the system level is investigated in this work, exploiting an approach coupling simulations and experiments offering the opportunity to benefit from the outputs of this *hardening by system strategy* in addition to other state-of-the-art approaches.

To achieve our goals, we consider a state-of-the-art REDFA simulation code, routinely used to optimize their optical performances in terms of gain and noise figure for Telecom-based applications. Thereafter, we update this code to take into account the radiation effects on such devices. This implies to perform RIA measurements at the pump and signal wavelengths and at the different aimed doses. By injecting these values in the code, it can be used to optimize the amplifier performances during the space mission rather than on-Earth. The simulation tools also appear efficient to investigate how an evolution of the REDFA architecture could help in mitigating the degradation mechanisms at the dose and dose rate of interest.

The simulation chain was validated by confronting its outputs with experimental data acquired on real devices based on the simulated amplifier architectures. The ability to predict the amplifier degradation during a radiation exposure is demonstrated. A high reliability was observed even for complex configurations with a maximum relative error less than 10 % at the highest degradation levels. Subsequently, the simulation tools were exploited to increase the amplifier tolerance to radiations selecting the most adapted system parameters and configurations to mitigate the radiation effects. Using this approach, the amplifier gain degradation can be reduced by ~ 65 % through optimized fiber lengths and pumping configuration adapted to the mission constraints without changing significantly the amplifier performances before irradiation.

Finally, several additional studies were carried out to improve this simulation tool, working both at the experimental and simulation levels.

For the experimental procedure:

- The photobleaching effects caused by the pump power on the RIA at the pump and signal wavelengths were investigated as our study highlights their strong influence for EDFA. We showed that the RIA of the investigated Erbium-doped fiber at the pump and signal wavelengths is reduced by about 60 % and 50 % respectively, between the unpumped fiber (OFF configuration) and the 180 mW pumped one.
- We also investigated the evolution of the RE ions metastable energy levels lifetimes as a function of the irradiation dose and that for different types of radiations (protons, gamma, neutrons,..). We demonstrate that the lifetimes of the Er^{3+} $^4I_{13/2}$ and the Yb^{3+} $^2F_{5/2}$ energy levels respectively reduce by about 30 % and 65 % between the pristine and the 10 MGy irradiated sample. We also characterized the impact of cooping the fiber with Cerium that stabilizes the Er^{3+} $^4I_{13/2}$ lifetime which remains constant even at high irradiation doses.

For the Simulation procedure:

- The code was updated to also consider the thermals effects on the amplifier characteristics. In fact, the variation of temperature can affect the amplifier performances at different levels such as the refractive index, the RE cross sections and the material thermal conductivity. By adding such effects to our model, more accurate simulations can be performed, in particular, in the case of high power EYDFAs.
- We also update the code to simulate complex amplification configurations such as the WDM one. This kind of amplification is very important to increase the data transfer speed in the inter-satellite and satellite-ground telecommunication systems. The code was validated without radiation for two input signals at different wavelengths and for various pumping powers by a comparison with experimental data.

BIBLIOGRAPHIES

[1] S. B. Poole, D. N. Payne, and M. E. Fermann, “Fabrication of low loss optical fibers containing rare earth ions”, Electron. Lett. 21, 737 (1985).

[2] V. Ter-Mikirtychev, Fundamentals of Fiber Lasers and Fiber Amplifiers, Springer, 2014.

[3] M.J.F. Digonnet, Rare-earth-doped fiber lasers and amplifiers, Marcel Dekker Inc. 2001.

[4] A. D’Orazio, M. De Sario, L. Mescia, V. Petruzzelli, Refinement of Er^{3+}-doped hole-assisted optical fiber amplifier, Opt. Express, 25 (2005) 9970-9981.

[5] B. Pedersen, K. Dybdal, C.D. Hansen, A. Bjarklev, J.H. Povlsen, H. Vendeltorp-Pommer, C.C. Larsen, Detailed theoretical and experimental investigation of high-gain erbium-doped fiber amplifier, IEEE Photon. Technol. Lett, 2 (1990) 863-865.

[6] M. De Sario, L. Mescia, F. Prudenzano, F. Smektala, F. Deseveday, V. Nazabal, J. Troles, L. Brilland, Feasibility of Er^{3+}-doped, $Ga_5Ge_{20}Sb_{10}S_{65}$ chalcogenide microstructured optical fiber amplifiers, OPT LASER TECHNOL 41 (2009) 99-106.

[7] Barry Coyle, ‘Applications of Fiber Amplifiers for Space: Laser Altimetry and Mapping,’ ESA-NASA Working Meeting on Optoelectronics, 2005

[8] Benoît Brichard , Alberto Fernandez Fernandez , Ez Fern , Hans Ooms , F. Berghmans, ‘Gamma dose rate effect in erbium-doped fibers for space gyroscopes,’. url: http://citeseerx.ist.psu.edu/viewdoc/download?doi=10.1.1.59.3242&rep=rep1&type=pdf

[9] T. Buret, D. Ramecourt, J. Honthaas, Y. Paturel, E. Willemenot, and T. Gaiffe, "Fibre Optic Gyroscopes for Space Application," in Optical Fiber Sensors, OSA Technical Digest (CD) (Optical Society of America, 2006), paper MC4.

[10] C. Claeys and E. Simoen, Radiation Effects in Advanced Semiconductor Materials and Device, (Springer Science & Business Media, 11 nov. 2013 - 404 pages).

[11] K. E. Holbert, Radiation effects and damage, http://holbert.faculty.asu.edu/eee560/RadiationEffectsDamage.pdf

[12] Mike Xapsos, Modeling the Space Radiation Environment, IEEE NSREC Short Course, 2006.

[13] Janet Barth, Modeling Space Radiation Environments, NSREC Short Course 1997.

[14] Janet L. Barth, ‘Space and Atmospheric Environments: from Low Earth Orbits to Deep Space’, DOI:10.1007/1-4020-2595-5_2.

[15] J. L. Barth, C. S. Dyer and E. G. Stassinopoulos, "Space, atmospheric, and terrestrial radiation environments," in IEEE Transactions on Nuclear Science, vol. 50, no. 3, pp. 466-482, June 2003.

[16] O. Amutkan, ‘Space radiation environment and radiation hardness assurance tests of electronic components to be used in space missions,’ PHD Thesis JULY 2010 url: https://etd.lib.metu.edu.tr/upload/12612238/index.pdf

[17] M. Schulz, L. J. Lanzerotti, ‘Particle Diffusion in the Radiation Belts’ (Springer Science & Business Media, 6 déc. 2012 - 218 pages) p 2-8

[18] Wikipedia The Free Encyclopedia, https://en.wikipedia.org/wiki/Cosmic_ray

[19] Peter B. de Selding, 'SpaceX's new price chart illustrates performance cost of reusability,', url: http://spacenews.com/spacexs-new-price-chart-illustrates-performance-cost-of-reusability/

[20] Fox, B. P., Simmons-Potter, K., Kliner, D. A. V., & Moore, S. W. (2013). Effect of low-earth orbit space on radiation-induced absorption in rare-earth-doped optical fibers. Journal of Non-Crystalline Solids, 378, 79-88

[21] M. Lezius et al., "Radiation Induced Absorption in Rare Earth Doped Optical Fibers," in IEEE Transactions on Nuclear Science, vol. 59, no. 2, pp. 425-433, April 2012.

[22] H. Henschel, O. Kohn, H. U. Schmidt, J. Kirchhof and S. Unger, "Radiation-induced loss of rare earth doped silica fibres," RADECS 97. Fourth European Conference on Radiation and its Effects on Components and Systems (Cat. No.97TH8294), Cannes, 1997, pp. 439-444.

[23] A. N. Chester, S. Martellucci and A.M. Verga, 'Optical Fiber Sensors,' Springer Science & Business Media, 6 déc. 2012 - 466 pages.

[24] S. Girard et al., "Radiation Effects on Silica-Based Optical Fibers: Recent Advances and Future Challenges," in IEEE Transactions on Nuclear Science, vol. 60, no. 3, pp. 2015-2036, June 2013.

[25] D. L. Griscom, M. E. Gingerich, and E. J. Friebele, 'Radiation-induced defects in glasses: Origin of power-law dependence of concentration on dose,' Phys. Rev. Lett. 71, 1019 – Published 16 August 1993.

[26] E.V. Anoikin, V.M. Mashinsky, V.B. Neustruev, Y.S. Sidorin, Effects of exposure to photons of various energies on transmission of germanosilicate optical fiber in the visible to near IR spectral range, Journal of Non-Crystalline Solids, Volume 179, 1994, Pages 243-253, ISSN 0022-3093.

[27] D. L. Griscom, M. E. Gingerich and E. J. Friebele, "Model for the dose, dose-rate and temperature dependence of radiation-induced loss in optical fibers," in IEEE Transactions on Nuclear Science, vol. 41, no. 3, pp. 523-527, Jun 1994.

[28] M. Lezius et al., "Radiation Induced Absorption in Rare Earth Doped Optical Fibers," in IEEE Transactions on Nuclear Science, vol. 59, no. 2, pp. 425-433, April 2012.

[29] O. Berne, M. Caussanel and O. Gilard, "A model for the prediction of EDFA gain in a space radiation environment," in IEEE Photonics Technology Letters, vol. 16, no. 10, pp. 2227-2229, Oct. 2004.

[30] T. S. Rose, M. S. Hopkins and R. A. Fields, "Characterization and control of gamma and proton radiation effects on the performance of Nd:YAG and Nd:YLF lasers," in IEEE Journal of Quantum Electronics, vol. 31, no. 9, pp. 1593-1602, Sep 1995.

[31] M. Lezius et al., "Radiation Induced Absorption in Rare Earth Doped Optical Fibers," in IEEE Transactions on Nuclear Science, vol. 59, no. 2, pp. 425-433, April 2012.

[32] S. Girard, A. Boukenter, Y. Ouerdane, J.-P. Meunier, J. Keurinck, Properties of phosphorus-related defects induced by γ-rays and pulsed X-ray irradiation in germanosilicate optical fibers, Journal of Non-Crystalline Solids, Volume 322, Issues 1–3, 15 July 2003, Pages 78-83.

[33] Q. Zeng, J.F. Stebbins, A.D. Heaney, T. Erdogan, Hydrogen speciation in hydrogen-loaded, germania-doped silica glass: a combined NMR and FTIR study of the effects of UV irradiation and heat treatment, Journal of Non-Crystalline Solids, Volume 258, Issues 1–3, November 1999, Pages 78-91, ISSN 0022-3093.

[34] J. E. Shelby, 'Radiation effects in hydrogen-impregnated vitreous silica,' Journal of Applied Physics, Volume 50, Issue 5, 1978, 3702-3706

[35] Sylvain Girard, Marilena Vivona, Arnaud Laurent, Benoît Cadier, Claude Marcandella, Thierry Robin, Emmanuel Pinsard, Aziz Boukenter, and Youcef Ouerdane, "Radiation hardening techniques for Er/Yb doped optical fibers and amplifiers for space application," Opt. Express 20, 8457-8465 (2012).

[36] S. Girard et al., "Proton Irradiation Response of Hole-Assisted Carbon Coated Erbium-Doped Fiber Amplifiers," in IEEE Transactions on Nuclear Science, vol. 61, no. 6, pp. 3309-3314, Dec. 2014.

[37] S. Girard, A. Laurent, E. Pinsard, T. Robin, B. Cadier, M. Boutillier, C. Marcandella, A. Boukenter, and Y. Ouerdane, "Radiation-hard erbium optical fiber and fiber amplifier for both low- and high-dose space missions," Opt. Lett. 39, 2541-2544 (2014).

[38] J. Stroud,' Photoionization of Ce^{3+} in Glass,' J. Chem. Phys., vol. 35, p. 844, 1961.

[39] Zhenan Gu, Spectroscopic properties of doped silica glasses, Journal of Non-Crystalline Solids, Volume 52, Issue 1, 1982, Pages 337-345, ISSN 0022-3093.

[40] E. Anoikin, A. Guryanov, D. Gusovskii, V. Mashinskii, S. M. V. Neustruev, V. Tikhomirov et Y. B. Zverev, 'Photoinduced defects in silica glass doped with germanium and cerium,' Sov Lightwave Commun., vol. 1, p. 123, 1991.

[41] B. D. Evans and G. H. Sigel, "Radiation Resistant Fiber Optic Materials and Waveguides," in IEEE Transactions on Nuclear Science, vol. 22, no. 6, pp. 2462-2467, Dec. 1975.

[42] M. Vivona, 'Radiation hardening of Rare-Earth doped fiber amplifier,' Phd thesis, Université Jean Monnet, Saint Etienne, France, 2013.

[43] J. Thomas, M. Myara, L. Troussellier, E. Burov, A. Pastouret, D. Boivin, G. Mélin, O. Gilard, M. Sotom, and P. Signoret, "Radiation-resistant erbium-doped-nanoparticles optical fiber for space applications," Opt. Express 20, 2435-2444 (2012).

[44] R. G. Ahrens et al., "Radiation reliability of rare earth doped optical fibers for laser communication systems (LT)," MILCOM 1999. IEEE Military Communications. Conference Proceedings (Cat. No.99CH36341), Atlantic City, NJ, 1, 694-697 (1999).

[45] B. P. Fox, K. Simmons-Potter, W. J. Thomes Jr. and D. A. V. Kliner, "Gamma-Radiation-Induced Photodarkening in Unpumped Optical Fibers Doped With Rare-Earth Constituents," in IEEE Transactions on Nuclear Science, vol. 57, no. 3, pp. 1618-1625, June 2010

[46] V. Ter-Mikirtychev, 'Fundamentals of Fiber Lasers and Fiber Amplifiers', XXI, 253p, Springer 2014.

[47] M. Sauer, J. Hofkens, and J. Enderlein, 'Handbook of Fluorescence Spectroscopy and Imaging'. WILEY-VCH Verlag, Weinheim 2011.pp 13

[48] M Moreno and M T Barriuso and J A Aramburu, 'The Huang-Rhys factor S(a 1g) for transition-metal impurities: a microscopic insight', Journal of Physics: Condensed Matter, 4, 47 p9481, 1992.

[49] Orazio Svelto, 'Principles of Lasers', Springer Science & Business Media 2010, p 1-10.

[50] Brian Henderson, G. Frank Imbusch, 'Optical Spectroscopy of Inorganic Solids', Clarendon Press, 2006 - p 158-160.

[51] Dipak K. Basu, 'Dictionary of Material Science and High Energy Physics', CRC Press 25 2001, p 66-68.

[52] Moody G, Kavir Dass C, Hao K, et al. 'Intrinsic homogeneous linewidth and broadening mechanisms of excitons in monolayer transition metal dichalcogenides'. Nature Communications. 2015, 6, 8315.

[53] C. B. Layne, W. H. Lowdermilk, and M. J. Weber, Multiphonon relaxation of rare-earth ions in oxide glasses, Phys. Rev. B 16, 10 – Published 1 July 1977.

[54] Hotan Shalibeik, Rare-Earth-Doped Fiber Lasers and Amplifiers, Cuvillier Verlag, 2007, p 21-23.

[55] Castor, S. B., & Hedrick, J. B. (2006). Rare earth elements. Industrial minerals volume, 7th edition: Society for mining, metallurgy, and exploration, Littleton, Colorado, 769-792.

[56] Taylor, S.R. and McLennan, S.M. (1985). The Continental Crust; Its composition and evolution; an examination of the geochemical record preserved in sedimentary rocks. Blackwell, Oxford. 312.

[57] A.P. Jones, F. Wall, C.T. Williams, 'Rare Earth Minerals: Chemistry, Origin and Ore Deposits', Springer Science & Business Media, 31 déc. 1995 - 372 pages.

[58] E.C. Subbarao, 'Science and Technology of Rare Earth Materials', Elsevier, 2 déc. 2012 - 439 pages.

[59] Daniel Timothy Bowron, 'a study of rare earth doped silicate and phosphate glasses', PhD thesis, The University of Kent at Canterbury 1994.

[60] G.N Greaves, 'EXAFS and the structure of glass,'J. Non-Cryst. Solids, 71, 203-217, 1985.

[61] V. McGahay and M. Tomzawa,' Microstructure and its relaxation in FeB amorphous system simulated by molecululular dynamics,' J. Non-Cryst Solids, 159, 246-252, 1993.

[62] John P. Dakin, Robert G. W. Brown, 'Handbook of Optoelectronics,' (CRC Press, 12 déc. 2010 - 1680 pages) 588-589.

[63] L. Qian, 'Experiment on Erbium-Doped Fiber Amplifiers,' Advanced Labs for Special Topics in Photonics (ECE 1640H) University of Toronto April 28,1998.

[64] C. M. Caves, "Quantum limits on noise in linear amplifiers", Phy. Rev. D. 26, 1817 (1982).

[65] R. Loudon and T. J. Shepherd, "Properties of the optical quantum amplifier", Optica Acta, 31, 1243 (1984).

[66] A. Cavaciuti, B. Sordo, "Noise measurements in EDFAs", Conference on Optcial Fiber Communications, OFC'94 Technical Digest, paper WM9, 163 (1994).

[67] Francesco Prudenzano, Luciano Mescia, Antonella D'Orazio, Marco De Sario, Vincenzo Petruzzelli, Alessandro Chiasera, and Maurizio Ferrari, "Optimization and Characterization of Rare-Earth-Doped Photonic-Crystal-Fiber Amplifier Using Genetic Algorithm," J. Lightwave Technol. 25, 2135-2142 (2007).

[68] Roger W. Pryor, 'Multiphysics Modeling Using COMSOL: A First Principles Approach,' (Jones & Bartlett Publishers, 8 déc. 2009 - 852 pages).

[69] R. Paschotta, article on 'effective cross sections' in the Encyclopedia of Laser Physics and Technology, 1. edition October 2008, Wiley-VCH, ISBN 978-3-527-40828-3.

[70] A. Bjarlev, 'Optical Fiber Amplifiers: Design and System Application' Norwood, MA, USA: Artech House, 1993.

[71] M. J. F. Digonnet, E. Murphy-Chutorian and D. G. Falquier, "Fundamental limitations of the Mc Cumber relation applied to Er-doped silica and other amorphous-host lasers," in IEEE Journal of Quantum Electronics, vol. 38, no. 12, pp. 1629-1637, Dec 2002.

[72] Autar Kaw, 'Newton-Raphson Method of Solving a Nonlinear Equation' University of South Florida Holistic Numerical Methods Institute.

[73] Solution of non-linear equations By Gilberto E. Urroz, September 2004.

[74] William H. Press, ‘NUMERICAL RECIPES: The Art of Scientific Computing, Third Edition’, ISBN-13 978-0-511-33555-6.

[75] Gear, C.W. 1971, Numerical Initial Value Problems in Ordinary Differential Equations (Englewood Cliffs, NJ: Prentice-Hall), Chapter 9.

[76] Shampine, L.F., and Gordon, M.K. 1975, Computer Solution of Ordinary Differential Equations. The Initial Value Problem. (San Francisco: W.H Freeman).

[77] William H. Press, ‘numerical recipes in fortran 77: the art of scientific computing’ ISBN 0-521-43064-X.

[78] Fornarelli, Girolamo,’ Swarm Intelligence for Electric and Electronic Engineering’, (IGI Global, 31 déc. 2012 - 368 pages)

[79] N. Jin and Y. Rahmat-Samii, "Advances in Particle Swarm Optimization for Antenna Designs: Real-Number, Binary, Single-Objective and Multiobjective Implementations," in IEEE Transactions on Antennas and Propagation, vol. 55, no. 3, pp. 556-567, March 2007.

[80] Aboul Ella Hassanien, Eid Emary,’ Swarm Intelligence: Principles, Advances, and Applications’, CRC Press, 5 avr. 2016 - 210 pages.

[81] Kennedy, J.; Eberhart, R., "Particle swarm optimization," in Neural Networks, 1995. Proceedings, IEEE International Conference on, vol.4, no., pp.1942-1948 vol.4, Nov/Dec 1995.

[82] A. Mahanfar, S. Bila, M. Aubourg and S. Verdeyme, "Design Considerations for the Implanted Antennas," 2007 IEEE/MTT-S International Microwave Symposium, Honolulu, HI, 2007, pp. 1353-1356.

[83] N. Iwasaki, K. Yasuda, and G. Ueno, , Dynamic parameter tuning of particle swarm optimization. IEEJ Trans Elec Electron Eng, 1, 353–363, 2006.

[84] J. F. Schutte, A. Groenwold, ‘A Study of Global Optimization Using Particle Swarms’, Journal of Global Optimization, Volume 31, Issue 1, pp 93–108, 2005.

[85] T. Huang and A. S. Mohan, "A hybrid boundary condition for robust particle swarm optimization," in IEEE Antennas and Wireless Propagation Letters, vol. 4, no. , pp. 112-117, 2005.

[86] Y. del Valle, G. K. Venayagamoorthy, S. Mohagheghi, J. C. Hernandez and R. G. Harley, "Particle Swarm Optimization: Basic Concepts, Variants and Applications in Power Systems," in IEEE Transactions on Evolutionary Computation, vol. 12, no. 2, pp. 171-195, April 2008.

[87] N. Jin and Y. Rahmat-Samii, "Advances in Particle Swarm Optimization for Antenna Designs: Real-Number, Binary, Single-Objective and Multiobjective Implementations," in IEEE Transactions on Antennas and Propagation, vol. 55, no. 3, pp. 556-567, March 2007.

[88] Y. Shi and R. Eberhart, "A modified particle swarm optimizer," Evolutionary Computation Proceedings, 1998. IEEE World Congress on Computational Intelligence. The 1998 IEEE International Conference on, Anchorage, AK, 1998, pp. 69-73.

[89] F. Van den Bergh, A.P. Engelbrecht, A study of particle swarm optimization particle trajectories, Information Sciences, Volume 176, Issue 8, 22 April 2006, Pages 937-971

[90] A. Ratnaweera, S. K. Halgamuge and H. C. Watson, "Self-organizing hierarchical particle swarm optimizer with time-varying acceleration coefficients," in IEEE Transactions on Evolutionary Computation, vol. 8, no. 3, pp. 240-255, June 2004.

[91] M. Clerc and J. Kennedy, "The particle swarm - explosion, stability, and convergence in a multidimensional complex space," in IEEE Transactions on Evolutionary Computation, vol. 6, no. 1, pp. 58-73, Feb 2002.

[92] iXBlue photonics https://www.ixblue.com/

[93] K. V. Zotov et al., "Radiation-resistant erbium-doped fiber for spacecraft applications," 2007 9th European Conference on Radiation and Its Effects on Components and Systems, Deauville, 2007, pp. 1-4.

[94] S. Girard, C. Marcandella, G. Origlio, Y. Ouerdane, A. Boukenter, J.-P. Meunier, Radiation-induced defects in fluorine-doped silica-based optical fibers: Influence of a pre-loading with H2, Journal of Non-Crystalline Solids, Volume 355, Issues 18–21, 1 July 2009, Pages 1089-1091.

[95] J. E. Shelby, “Molecular diffusion and solubility of hydrogen isotopes in vitreous silica,” Journal of Applied Physics 48, 3387 (1977).

[96] B. Malo, J. Albert, K.O. Hill, F. Bilodeau and D.C. Johnson, “Effective index drift from molecular hydrogen diffusion in hydrogen-loaded optical fibres and its effect on Bragg grating fabrication”, Electronics Letters ,Volume 30, Issue 5, 3 March 1994, p. 442 – 444.

[97] H. Kuswanto, ‘Formation et transformation des défauts ponctuels dans les fibres optiques germanosilicates : influence du traitement thermique et de l'insolation UV’ PhD theses, http://www.theses.fr/2001STET4010.

[98] S. Girard, A. Laurent , E. Pinsard, T. Robin, B. Cadier, M. Boutillier, C. Marcandella, A. Boukenter, Y. Ouerdane, Free-Space Laser Communication and Atmospheric Propagation XXVI, doi:10.1117/12.2039847.

[99] Lemaire PJ; Reliability of optical fibers exposed to hydrogen: prediction of long-term loss increases. Opt. Eng. 0001;30(6):780-789.

[100] Leproux Philippe, Valérie Doya, Roy Philippe, Pagnoux Dominique, Mortessagne Fabrice, Legrand Olivier, Experimental study of pump power absorption along rare-earth-doped double clad optical fibres, Optics Communications, Volume 218, Issues 4–6, 1 April 2003, Pages 249-254.

[101] J. R. Schwank et al., "Optimum laboratory radiation source for hardness assurance testing," in IEEE Transactions on Nuclear Science, vol. 48, no. 6, pp. 2152-2157, Dec 2001.

[102] P. Paillet et al., "Comparison of charge yield in MOS devices for different radiation sources," in IEEE Transactions on Nuclear Science, vol. 49, no. 6, pp. 2656-2661, Dec 2002.

[103] S. Girard et al., "Proton- and Gamma-Induced Effects on Erbium-Doped Optical Fibers," in IEEE Transactions on Nuclear Science, vol. 54, no. 6, pp. 2426-2434, Dec. 2007.

[104] S. Girard et al., "Radiation Effects on Silica-Based Optical Fibers: Recent Advances and Future Challenges," in IEEE Transactions on Nuclear Science, vol. 60, no. 3, pp. 2015-2036, June 2013.

[105] G. De Angelis, M.S. Clowdsley, J.E. Nealy, R.K. Tripathi, J.W. Wilson, "Radiation analysis for manned missions to the Jupiter system," Adv. Space Res. 34(6), 1395-1403 (2004).

[106] S. Girard et al., "Design of Radiation-Hardened Rare-Earth Doped Amplifiers Through a Coupled Experiment/Simulation Approach," in Journal of Lightwave Technology, vol. 31, no. 8, pp. 1247-1254, April15, 2013.

[107] H. Henschel and O. Kohn, "Regeneration of irradiated optical fibres by photobleaching?," in IEEE Transactions on Nuclear Science, vol. 47, no. 3, pp. 699-704, Jun 2000.

[108] Michael Gaft, Renata Reisfeld, Gerard Panczer, 'Modern Luminescence Spectroscopy of Minerals and Materials', Springer, 29 nov. 2015, p 14,15.

[109] Marilena Vivona, 'Radiation hardening of rare-earth doped fiber amplifiers', PhD thesis, Université Jean Monnet, France.

[110] Blandine Tortech, "Effets des radiations sur des fibres optiques dopees Erbium : influence de la composition," https://tel.archives-ouvertes.fr/tel-00366057/document.

[111] S. Girard ; A. Laurent ; E. Pinsard ; T. Robin ; B. Cadier ; M. Boutillier ; C. Marcandella ; A. Boukenter ; Y.Ouerdane; Radiation-hardened Erbium-doped optical fibers and amplifiers for future high-dose space missions . Proc. SPIE 8971, Free-Space Laser Communication and Atmospheric Propagation XXVI, 89710E (March 6, 2014);

[112] M. Achtenhagen, R. J. Beeson, F. Pan, B. Nyman and A. Hardy, "Gain and noise in ytterbium-sensitized erbium-doped fiber amplifiers: measurements and simulations," in J. Lightw. Technol, vol. 19, no. 10, pp. 1521-1526, Oct 2001.

[113] Y. Hu, S. Jiang, G. Sorbello, T. Luo, Y. Ding, B. C. Hwang, J. H. Kim, H. J. Seo, and N. Peyghambarian, "Numerical analyses of the population dynamics and determination of the upconversion coefficients in a new high erbium-doped tellurite glass," J. Opt. Soc. Am. B. 18(12), 1928-1934 (2001

[114] O. Henderson-Sapir, J. Munch, and D. J. Ottaway, "Mid-infrared fiber lasers at and beyond 3.5 μm using dual-wavelength pumping," Opt. Lett. 39(3), 493-496 (2014).

[115] H. Henschel, O. Kohn, "Regeneration of irradiated optical fibres by photobleaching," IEEE Trans. Nucl. Sci 47(3), 699–704 (2000).

[116] Ayoub Ladaci, Sylvain Girard, Luciano Mescia, Thierry Robin, Arnaud Laurent, Benoit Cadier, Mathieu Boutillier, Youcef Ouerdane, Aziz Boukenter, 'Optimization of rare-earth-doped amplifiers for space mission through a hardening-by-system strategy,' Proc. SPIE 10096, Free-Space Laser Communication and Atmospheric Propagation XXIX, 100960F (February 24, 2017).

[117] A. Ladaci, S. Girard, L. Mescia, T. Robin, A. Laurent, B. Cadier, M. Boutillier, Y. Ouerdane, and A. Boukenter, Optimized radiation-hardened erbium doped fiber amplifiers for long space missions, J. Appl. Phys. 121 (2017) 163104.

[118] S. Girard, L. Mescia, M. Vivona, A. Laurent, Y. Ouerdane, C. Marcandella, F. Prudenzano, A. Boukenter, T. Robin, P. Paillet, V. Goiffon, M. Gaillardin, B. Cadier, E. Pinsard, M. Cannas, R. Boscaino, "Design of Radiation-Hardened Rare-Earth Doped Amplifiers Through a Coupled Experiment/Simulation Approach," J. Lightwave Technol 31(8), 1247-1254 (2013).

[119] Vera Pukhkaya, Philippe Goldner, Alban Ferrier, and Nadège Ollier, "Impact of rare earth element clusters on the excited state lifetime evolution under irradiation in oxide glasses," Opt. Express 23, 3270-3281 (2015)

[120] Ayoub Ladaci, Sylvain Girard, Luciano Mescia, Thierry Robin, Arnaud Laurent, Benoit Cadier, Mathieu Boutillier, Adriana Morana,Youcef Ouerdane and Aziz Boukenter, 'Cerium co-doping effect on stabilizing the irradiation dose lifetime dependency of Rare earth ions in optical fibers', submitted to journal of Luminescence, 2017.

[121] Yasmine Mebrouk, Franck Mady, Mourad Benabdesselam, Jean-Bernard Duchez, and Wilfried Blanc, "Experimental evidence of Er3+ ion reduction in the radiation-induced degradation of erbium-doped silica fibers," Opt. Lett. 39, 6154-6157 (2014)

[122] Ayoub Ladaci, Sylvain Girard, Luciano Mescia, Thierry Robin, Arnaud Laurent, Benoit Cadier, Mathieu Boutillier, Youcef Ouerdane and Aziz Boukenter 'Parametric Simulation Study of the Influence of Rare-Earth Ions Spectroscopic Parameters on Er-Yb doped Fiber Amplifier Performances', submitted to Journal of light wave technology, 2017.

[123] T. E. Tsai, C. G. Askins, and E. J. Friebele, 'Photoinduced grating and intensity dependence of defect generation in Ge-doped silica optical fiber', Appl. Phys. Lett. 61, 390 (1992).

[124] John A. Weil, 'A review of electron spin spectroscopy and its application to the study of paramagnetic defects in crystalline quartz', J.A. Phys Chem Minerals, Volume 10, Issue 4, pp 149–165. 1984

[125] Nicholas Koumvakalis, Defects in crystalline SiO2:Optical absorption of the aluminum-associated hole center, Journal of Applied Physics 51, 5528 (1980).

[126] C J Walsby, N S Lees, R FC Claridge, J A Weil, The magnetic properties of oxygen-hole aluminum centres in crystalline SiO2. VI: A stable AlO4/Li centre, Canadian Journal of Physics, 2003, 81:583-598.

[127] E.J. Friebele, Radiation protection of fiber optic materials: Effect of cerium doping on the radiation-induced absorption, Appl. Phys. Lett. 27(1975) 210-212.

[128] J. Linnros, N. Lalic, A. Galeckas, and V. Grivickas, Analysis of the stretched exponential photoluminescence decay from nanometer-sized silicon crystals in SiO2, J. Appl. Phys. 86 (1999) 6128.

[129] E. Regnier, I. Flammer, S. Girard, F. Gooijer, F. Achten, G. Kuyt, Low-Dose Radiation-Induced Attenuation at InfraRed Wavelengths for P-Doped, Ge-Doped and Pure Silica-Core Optical Fibres, in Nuclear Science, IEEE Trans. Nucl. Sci , 54 (2007) 1115-1119.

[130] S. Girard, Y. Ouerdane, B. Tortech, C. Marcandella, T. Robin, B. Cadier, J. Baggio, P. Paillet, V. Ferlet-Cavrois, A. Boukenter, J.P. Meunier, J.R. Schwank, M.R. Shaneyfelt, P.E. Dodd, E.W. Blackmore, Radiation Effects on Ytterbium- and Ytterbium/Erbium-Doped Double-Clad Optical Fibers, IEEE Trans. Nucl. Sci. 56 (2009) 3293-3299.

[131] M. Vivona, S. Girard, T. Robin, B. Cadier, L. Vaccaro, M. Cannas, A. Boukenter, Y. Ouerdane, Influence of Ce3+ Codoping on the Photoluminescence Excitation Channels of Phosphosilicate Yb/Er-Doped Glasses, IEEE Photon. Technol. Lett. 24 (2012) 509-511.

[132] S, Agnello, Gamma ray induced processes of point defect conversion in silica, PhD thesis Palermo, December 2000. http://www1.unipa.it/lamp/AgnelloPhDThesis.pdf.

[133] S. Girard, J. Keurinck, Y. Ouerdane, J.P. Meunier, A. Boukenter, J.L. Derep, B. Azais, P. Charre, M. Vie, Pulsed X-ray and γ rays irradiation effects on polarization-maintaining optical fibers, IEEE Trans. Nucl. Sci. 51 (2004) 2740-2746.

[134] D. L. Griscom, E.J. Friebele, K.J. Long, J.W. Fleming, Fundamental defect centers in glass: Electron spin resonance and optical absorption studies of irradiated phosphorus-doped silica glass and optical fibers, J. Appl. Phys. 54 (1983) 3743-3762.

[135] Y.G. Choi K.H. Kim, Comparative study of energy transfers from Er3+ to Ce3+ in tellurite and sulfide glasses under 980 nm excitation, J. Appl. Phys. 88 (2000) 3832.

[136] Chien-Nan Lin, Jiin-Yuh Jang, A two-dimensional fin efficiency analysis of combined heat and mass transfer in elliptic fins, International Journal of Heat and Mass Transfer, Volume 45, Issue 18, August 2002, Pages 3839-3847, ISSN 0017-9310.

[137] S. Girard, "Rapport Préliminaire : Approche Couplée Simulations/Expériences pour la réalisation d'amplificateurs optiques optimisés pour les applications spatiales » CNES n°141110/00, 2015.

[138] S. Girard, "Rapport Final : Approche Couplée Simulations/Expériences pour la réalisation d'amplificateurs optiques optimisés pour les applications spatiales », CNES n°141110/00, 2015.

[139] S. Girard, A. Laurent, E. Pinsard, M. Raine, T. Robin, B. Cadier, D. Di Francesca, P. Paillet, M. Gaillardin, O. Duhamel, C. Marcandella, M. Boutillier, A. Ladaci, A. Boukenter and Y. Ouerdane, "Proton irradiation response of Hole-Assisted Carbon Coated Erbium-Doped Fiber Amplifiers", IEEE Transactions on Nuclear Science, vol.61(6), pp.3309-3314, Dec. 2014.

[140] S. Girard, L. Mescia, M. Vivona, A. Laurent, Y. Ouerdane, C. Marcandella, F. Prudenzano, A. Boukenter, T. Robin, P. Paillet, V. Goiffon, M. Gaillardin, B. Cadier, E. Pinsard, M. Cannas, and R. Boscaino "Design of Radiation-Hardened Rare-Earth Doped Amplifiers Through a Coupled Experiment/Simulation Approach", Journal of Lightwave Technology, vol.31, no.8, pp.1247-1254, 2013.

[141] L. Mescia, S. Girard, P. Bia, T. Robin, A. Laurent, F. Prudenzano, A. Boukenter, Y.Ouerdane, "Optimization of the design of high power Er3+/Yb3+–codoped fiber amplifiers for space missions by means of particle swarm approach", IEEE Journal of Selected Topics in Quantum Electronics, vol.20, n°5, ID# 3100108, 2014.

[142] S. Girard, A. Laurent, E. Pinsard, T. Robin, B. Cadier, M. Boutillier, C. Marcandella, A. Boukenter, and Y. Ouerdane,"Radiation-hard erbium optical fiber and fiber amplifier for both low and high dose space missions", Optics Letters, Vol. 39, Issue 9, pp. 2541-2544, 2014.

[143] Gorachand Ghosh, 'Handbook of Optical Constants of Solids : Handbook of Thermo-Optic Coefficients of Optical Materials with Applications,' Academic Press, 24 juin 1998, 12-250.

[144] D. C. Brown, H. J. Hoffman, Thermal, Stress, and Thermo-Optic Effects in High Average Power Double-Clad Silica fiber Lasers, IEEE journal of quantum electronics, VOL. 37, NO. 2, FEBRUARY 2001, pp. 207-2017

[145] J. F. Nye, Physical Properties of Crystals. Oxford, U.K.: Clarendon, 1993.

[146] D. E. McCumber, 'Einstein relations connecting broadband emission and absorption spectra,' Phys. Rev. 136, A954–A957 (1964).

List of publications

Journal papers

A. Ladaci, S. Girard, L. Mescia, T. Robin, A. Laurent, B. Cadier, M. Boutillier, Y. Ouerdane, and A. Boukenter, Optimized radiation-hardened erbium doped fiber amplifiers for long space missions, J. Appl. Phys. 121 (2017) 163104.

A. Ladaci et al, “X-rays, γ-rays, electrons and protons radiation-induced changes on the lifetimes of Er3+ and Yb3+ ions in silica-based optical fibers”, submitted to J. Lumin. 2017.

S. Girard, A. Laurent, E. Pinsard, M. Raine, T. Robin, B. Cadier, D. Di Francesca, P. Paillet, M. Gaillardin, O. Duhamel, C. Marcandella, M. Boutillier, A. Ladaci, A. Boukenter and Y.Ouerdane, "Proton Irradiation Response of Hole-Assisted Carbon Coated Erbium-Doped Fiber Amplifiers," in IEEE Trans. Nucl. Sci., **61** (6), 3309-3314, 2014.

S. Girard, D. Di Francesca, A. Boukenter, T. Robin, E. Marin, A. Ladaci, I. Reghioua, A. Morana, S. Rizzolo, C. Cangialosi, I. Planes, J.Y. Michalon, C. Marcandella, P. Paillet, M. Gaillardin, M. Raine, N. Richard, B. Cadier and Y. Ouerdane., "On-site Regeneration Technique for Hole-Assisted Optical Fibers Used In Nuclear Facilities," in IEEE Trans. Nucl. Sci., **62** (6), 2941-2947, 2015.

D. Di Francesca, S. Girard, I. Planes, A. Cebollada, G. Li Vecchi, A. Alessi, I. Reghioua, C. Cangialosi, A. Ladaci, S. Rizzolo, V. Lecoeuche, A. Boukenter, A. Champavere and Y. Ouerdane, "Radiation Hardened Architecture of a Single-Ended Raman-Based Distributed Temperature Sensor," in IEEE Trans. Nucl. Sci., **64** (1), 54-60, 2017.

Conference papers

A. Ladaci et al," Optimization of rare-earth-doped amplifiers for space mission through a hardening-by-system strategy". Proc. SPIE 10096, Free-Space Laser Communication and Atmospheric Propagation XXIX, 100960F (February 24, 2017).

S. Girard, Y. Ouerdane, E. Pinsard, , A. Laurent, A. Ladaci , T. Robin, B Cadier, L Mescia and A. Boukenter "Radiation hardening of optical fibers and fiber sensors for space applications: recent advances". In International Conference on Space Optics (Vol. 7, p. 10).

List of conferences

National conferences

A. Ladaci, S. Girard, A. Boukenter, T. Robin, B. Cadier, Y. Ouerdane, L.Mescia, "Fibres optiques dopées aux terres rares et amplificateurs optiques pour applications spatiales" FMR 2014 (fiber optic in harsh environments) Lille, France. Oral presentation

A. Ladaci, S. Girard, A. Boukenter, T. Robin, B. Cadier, Y. Ouerdane, L.Mescia : 'Fibres optiques dopées aux terres rares et amplificateurs optiques pour applications spatiales' . JNOG (National days of guided optics) 2015, Rennes. Poster contribution.

A. Ladaci, S. Girard, L. Mescia, E. Pinsard, T. Robin, B. Cadier, A. Laurent, M. Boutillier,Y. Ouerdane and A. Boukenter," Approche couplée Simulation/Expérience pour l'optimisation des amplificateurs à fibre dopée Erbium', FMR 2016 (fiber optic in harsh environments) Paris, France. Oral presentation

International conferences

A. Ladaci, S. Girard, L. Mescia, E. Pinsard, T. Robin, B. Cadier, A. Laurent, M. Boutillier,Y. D. Di Francesca, Ouerdane and A. Boukenter, "Optimization of Erbium Doped Fiber Amplifiers for space missions using a coupled experience/simulation approach to mitigate radiation effects", ISROS 2016 Conference (Warszawa, Poland). Oral presentation

A. Ladaci, S. Girard, L. Mescia, E. Pinsard, T. Robin, B. Cadier, A. Laurent, M. Boutillier,Y. D. Di Francesca, Ouerdane and A. Boukenter, "Simulation results of fiber-based optical amplifiers: parametric study of the influence of rare-earths spectroscopic parameters", ISROS 2016 Conference (Warszawa, Poland). Poster presentation (**Student Award**)

A. Ladaci, S. Girard, L. Mescia, E. Pinsard, T. Robin, B. Cadier, A. Laurent, M. Boutillier,Y. Ouerdane and A. Boukenter, " Validation of the McCumber theory in a wide temperature range for Er3+emission cross section calculation in optical fibers". SiO2 Conference 2016 Nice, France. Oral presentation

A. Ladaci, S. Girard, L. Mescia, E. Pinsard, T. Robin, B. Cadier, A. Laurent, M. Boutillier,Y. Ouerdane and A. Boukenter," Optimization of rare-earth-doped amplifiers for space mission through a hardening-by-system strategy," SPIE Photonic west 2017 (Free-Space Laser Communication and Atmospheric Propagation) San Francisco USA. Oral presentation